MASTER THESIS

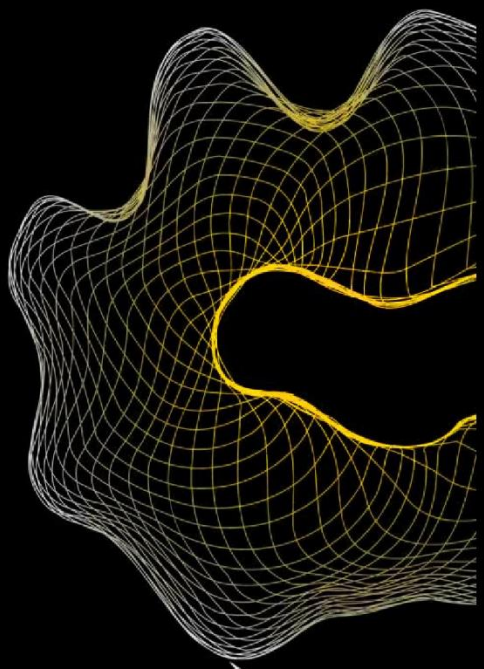

A NOVEL 3D ENGINEERED BREAST CANCER MODEL TO STUDY ULTRASOUND - MEDIATED DRUG PENETRATION INTO THE TUMOR MICROENVIRONMENT.

Alessia Bacci

FACULTY OF SCIENCE AND TECHNOLOGY
DEPARTMENT OF BIOMATERIALS SCIENCE TECHNOLOGY

EXAMINATION COMMITTE

Prof. Dr. Jai Prakash
Prof. Dr. Michel Versluis
Dr. Andries van der Meer
MSc. Marcel A. Heinrich
MSc. Ali Rezae

UNIVERSITY OF TWENTE.

25/08/2021

ACKNOWLEDGEMENTS

After two years in the Targeted Therapeutic group (Biomaterial Science Technology), I would like to express my sincere gratitude to Prof. Jai Prakash for supporting and making possible every learning and professional goal that I set for myself. Thanks for all the scientific knowledge and for the precious opportunities, truly.

I am immensely grateful to Marcel Heinrich, for his patience, for his important supervising, guidance, and passion in imparting his broad knowledge. Thank you for having shaped and improved my scientific approach, I am proud of this, and it is something that I will always bring with me.

The very first prize for the most stood patience, however, goes to Ali Razaei, crucial for the success of this project. Thanks for cheering me up even in the darkest moments of the project. Thanks for all the efforts, we did it!

Thanks to Michel Versluis and Guillaume Lajoinie for having made possible this multidisciplinary and broad collaboration. My fascination for the topic arose two years ago, I never imagined that, as of today, I would have been able to do my master thesis on this. Thanks for your essential availabilities and guidance.

A special thank you goes to Kunal Pednekar, and not only for the thousands of coffees. Albeit the fresh and frenzied start in your career, you were able to be there for everyone. Your generosity always preceded you and I am very thankful.

Thanks to Mark, Hetty, Lydia, and Karin for being there, willing to help, in every circumstance.

Thanks to my De Heurne family & friends. Thanks for having constantly been part of this, for having been my second family, always. I miss you all already. Thanks to Marta, Irene, Marina, and Ornela for these years full of food and wine, for the shared anxieties, the belly laughs, and the love. Thanks to my family, a milestone in all my choice, for all the sacrifices done to satisfy and support my curiosities and wishes. Finally, I would like to thank Marco who, in all these years, has always shown his tireless and fundamental support without ever making me feel alone, wherever I was.

TABLE OF CONTENTS

List of abbreviations

ABSTRACT

The intratumoral delivery of anticancer drugs is subjected to many transport steps from the blood vasculature to the tumor interstitial space across biological barriers that can undergo significant structural changes upon the establishment of tumorigenic events. Breast cancer, as one of the most desmoplastic solid tumors, owns a fibrotic impenetrable stroma due to the aberrant deposition of extracellular matrix (ECM) proteins upon remodelling. Along with the endothelial barrier, the dense stroma hampers the diffusion of therapeutic molecules into the tumor niche, implying a suboptimal exposure to the anticancer drug that, in turn, leads to treatment failure. For this reason, intense research is focused on maximizing the ratio of dose/exposure at the expense of undesired side effects through the modulation of the tumor microenvironment (TME) components. In particular, the use of microbubbles-combined ultrasound (MBs-US) has received great interest in the therapeutic field due to its ability to locally generate temporary formation of openings in the endothelium due to volumetric oscillations of MBs upon US exposure, namely MBs-mediated sonoporation. Understanding how tissue barriers work and which cellular crosstalks are affected by MBs-US is essential for the optimization of acoustical parameters towards an effective translation to the clinic. Due to the multifaceted nature of the subject, the lack of specific preclinical models, and the need for appropriate optical equipment, however, it is challenging to unravel and observe the underlying mechanisms involved in MBs-US drug delivery. Latest advances in biomaterials and microfluidics have allowed the implementation of relevant physiological microsystems in which tissues- and organ-level functions are recapitulated, and pathological conditions can be induced. In this research, a clinically relevant 3D in vitro breast cancer triculture microtissue (BCM) was developed for investigations on the role of biological barriers on differently sized molecules transport. Furthermore, the model owns appropriate optical and acoustical features for being an investigation platform of MBs-US-mediated enhanced molecules diffusion. In particular, the physicochemical properties and architecture of the hydrogel-based scaffold of the BCM were defined through dynamic mechanical analysis, acoustical characterizations, and immunohistochemical staining. Gene and protein expression via qPCR and immunohistochemical staining were evaluated to assess the biological significance of the BCM, while the clinical relevance was verified through comparison with transcriptomic data of breast cancer patients. The BMC model was assembled and then used to show the effect of both endothelium and stromal barriers on molecules' diffusion within the tissue showing the diffusion limitations according to molecule size and type of barrier. Lastly, the model was employed to observe the dynamic of cavitating MBs within the endothelialized channel and their beneficial effects on enhanced molecules' transepithelial transport upon US exposure.

Altogether the developed BCM model for MBs-US studies provides a solid investigation platform that, compared to the state of the art, owns higher biological complexity and organ-specific architecture through the recapitulation of tissue diffusion barriers. Therefore, the BCM model provides more accurate insights into the biophysical effects of MBs-US on the surrounding tissues with enabling a predictive estimation of cellular damage and optimization of acoustical parameters for enhanced drug delivery.

1. INTRODUCTION

The development of effective, controllable, and targeted, anticancer drug delivery approaches is addressed to maximize the therapeutic power by ensuring optimal drug concentrations at the tumorigenic site and reducing unnecessary cytotoxic off-target exposure. in this view, cancer nanomedicine has yielded important combinatorial treatment options by exploiting drug carriers able to interact in a relatively selective fashion with specific components of the TME either via passive or active targeting. Yet, the targeted biological complexity and (inter- and intra- tumoral) heterogeneities of in vivo situations have been shown to negatively impact the efficiency of such therapeutic strategies inasmuch they introduce elements of uncontrollable variability in drug response patterns hardly reproducible in preclinical models. Therefore, it is well consolidated that one of the hardest challenges in drug discovery is how translatable preclinical data are from in vitro studies to in vivo situations. Alternatively, this issue can be reformulated in how predictable are the pre-clinical in vitro drug screening platforms are and how accurate they can be in mimicking in vivo tissue responses to treatment?

Great efforts should be made to be able to recapitulate and priorly investigate *in vitro*, even only to a minimum extent, the *in vivo* scenarios behind the therapeutic failure.

Of these, biological barriers are one of the main obstacles involved in the compromised effectiveness of therapeutic regimens given their selective size-based permeability to foreign and potentially harmful compounds. The endothelium, for example, represents the biological barrier par excellence since it regulates the exchange of molecules between tissues and the bloodstream. In situations of severe solid carcinomas such as breast and pancreas, however, the endothelial barriers result in compromised by the surrounding tumorigenic tissue which exerts significant compression due to solid stress and high interstitial fluid pressure (IFP) which, eventually, lead to the blood vessel collapse. The fibrotic desmoplastic reaction triggered in these types of dense cancers induces, in fact, the formation of an impenetrable stromal barrier upon augmented deposition of ECM proteins and uncontrolled proliferative cells activity. Depending on what needs to be assessed with preclinical drug screening platforms, the integration of such physical impediment yielded by biological barriers is often neglected. Recent advances in oncology, however, have led to the development of enhanced local drug delivery technologies which attempt to overcome such biological barriers. These are mostly based on physical approaches in which external stimuli are applied to generate or modulate biological responses aimed at facilitating the chemotherapeutic penetration into biological tissues. In this perspective, the application of focused ultrasound (US) fields mediated by gas-filled microbubbles (MBs) has shown great potential in enhanced permeability and tumoral penetration of anticancer agents by means of cavitation phenomena. Even in this case, however, discrepancies and limitations of the preclinical set-ups hinder the optimal translation into the clinic. Notably, relatively to this multidisciplinary case, the development of appropriate in vitro platforms aimed at unravelling the underlying biomechanical mechanisms underlying the MBs-mediated US-based drug delivery and at the optimization of the therapeutic parameters, needs to face a broader spectrum of challenges in line with the biological, acoustical, and optical requirements. Ideally, the in vitro model should integrate biological relevancy and possibly complexity, as well as respect optical and acoustical suitability. To the best of our knowledge, current in vitro models for MBs-mediated US applications failed to integrate all these aspects while prioritizing either one aspect (acoustical) rather than the other (biological) and vice versa.

In this research project, the implementation of a three dimensional (3D) in vitro model was addressed at the recapitulation of a relatively dense breast cancer-like microtissue through which both, the effect of biological barriers on molecules diffusion, and the beneficial effects of MBs-mediated US on biological barriers, can

be observed and measured. The accomplishment of research goals implied a multidisciplinary approach along with all the phases of the project, from the establishment of an acoustically and optically clear cell-culture biomaterial to its characterization and, simultaneously, from the design of a model adequate for different set-ups to its optimization, versatility, ease of analysis and reproducibility. Therefore, a tri-culture-based breast cancer microtissue (BCM) characterized by clinical and architectural relevance has been implemented through which molecules transport is investigated in the presence of biological barriers, namely endothelium and stroma, and in the conditions of MBs-mediated US (MBs-US) treatment.

2. BREAST CANCER

Breast cancer (BC) has been recently declared as the most diagnosed cancer by the International Agency for Research on Cancer (IARC) with 2.3 million new cases and 685.000 related deaths in 2020 for a total of 7.8 million cases worldwide in the last 5 years. Due to its elevated morbidity and mortality, it is considered a major public health concern and, future projections estimate that 1 in 12 women will develop breast cancer in their lifetime in the incoming years [1]. Advances in diagnostic techniques, such as mammography, magnetic resonance imaging (MRI), and ultrasound imaging (sonography), have allowed the timing identification of the tumor and thus the prompt intervention with efficacious anticancer treatments which led to a 5-year survival rate of 90% of cases and reduced the mortality rate by 40% (according to the socio-economic status of the country) [2 3]. There are cases, however, in which the tumor mass becomes visible in later stages, when the tumor is already in the metastatic phase, as current BC screening technologies cannot discern it on time yielding, at first, false-negative results. This is the case with denser BC. Among the risk factors associated with BC development and mortality, in fact, the major is the mammographic density (MD), defined as the proportion between the low-density adipose tissue and high-density fibroglandular stromal tissue, followed by a longer-established western lifestyle and age [4 5].
Among all solid tumors, breast cancer owns the broader inter- and intra-tumoral heterogeneity as it encompasses a wide spectrum of histological, molecular, and genetic aberrations in mammary epithelial cells which are reflected in the multitude of pathologic conditions discerned in breast cancer subtypes (Fig.1) [6]. Certainly, each BC subtype shows different sensitivity and resistance to the available current treatments which, with the singular clinical history of the patient, defines the therapeutic regimens that should be adopted to avoid therapeutic failure and maximize prognosis outcomes.
Current treatments in BC care are surgery, radiotherapy, chemotherapy, hormone therapy, and targeted therapy according to the single clinical scenario and cancer stage. In advanced or invasive cancer stages, surgical approaches, such as partial or complete mastectomy and sentinel node biopsy are employed. Significant achievements in BC treatments have been reached with radiation therapy that, at different stages of the disease, even when metastatic, can prevent mastectomy, possibly reducing the risk of mortality. Radiation therapy uses localized high-energy X-rays to effectively kill cancers cells and shrink the tumor without affecting normal tissues. For its versatile action, radiation therapy is usually employed following surgical dissection to reduce the risk of cancer recurrence. Biological approaches, on the other side, can be employed as neoadjuvant (pre-surgery) or as adjuvant (post-surgery) treatments according to the single breast cancer types. About 84% of BC is a luminal-like subtype, characterized by the expression of PR or ER, and likely response to 5-10 years endocrine (hormonal) therapies, such as aromatase or tamoxifen inhibitors. The amount of HER2 protein made by the cancer cells is also determinant for treatment choice as HER2+ breast cancers are more aggressive in growth and spreading. In particular, HER2+ breast

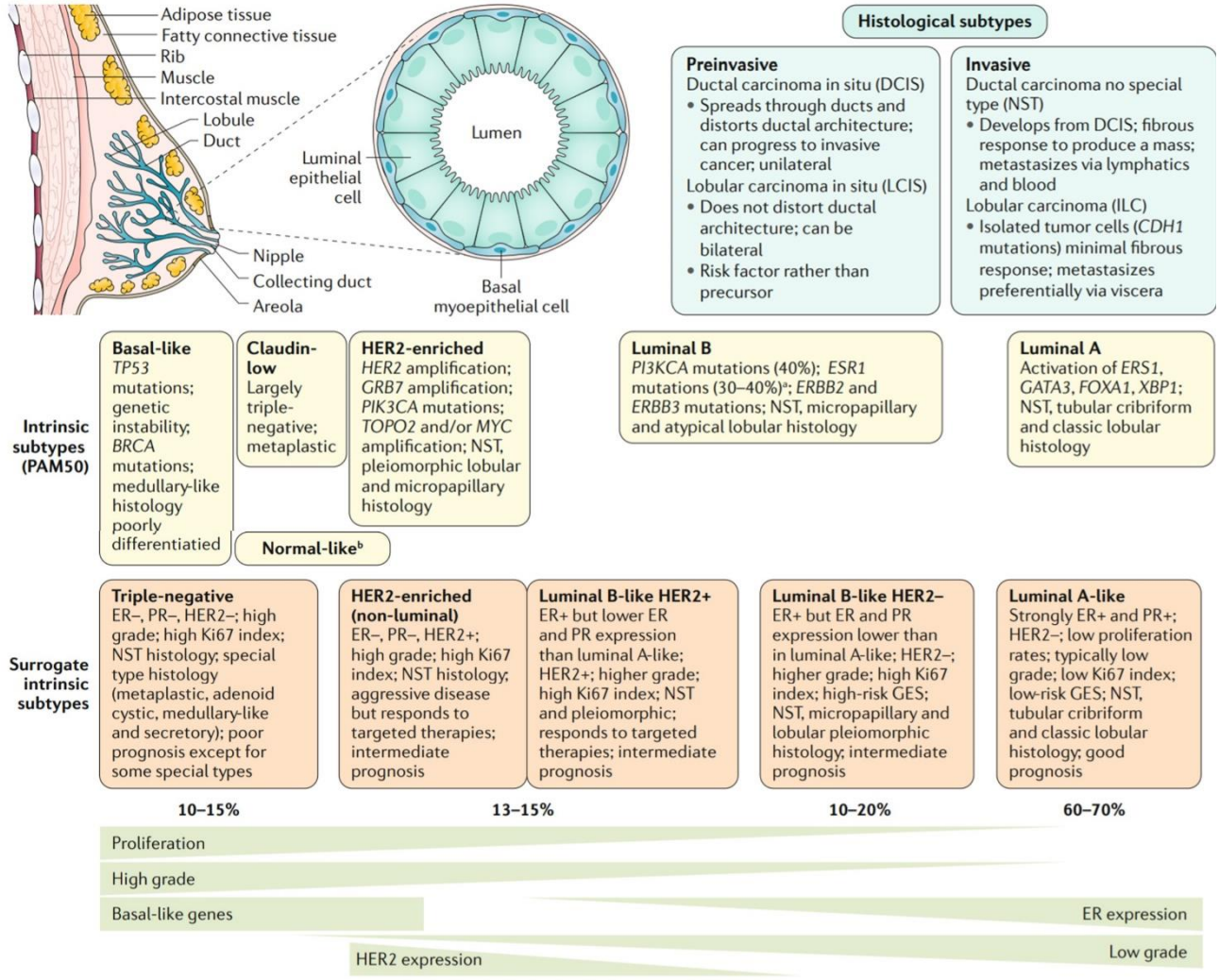

FIG. 1 BREAST CANCER (BC) SUBTYPES WHICH GENERATE IN THE TERMINAL DUCT LOBULAR UNITS. Classification based on molecular and histological characterization which own different degree of aggressivity and have different therapeutic implications. Pictures adapted from Harbeck et al. [5].

cancers show overexpression of ERBB2 oncogene and are amenable to be treated with antibodies-mediated targeted therapy, as in the case of trastuzumab or pertuzumab, or small molecules inhibitors in combination with hormonal therapy and chemotherapy [7]. Besides ErbB family members, the most common breast cancer-specific molecules employed in targeted therapy include vascular endothelial growth factor (VEGF) family members, components of Ras/MAPK pathway, apoptosis and cell cycle regulators (BAX, BCL-2, p53 and element of PI3K/Akt/mTOR pathway), and DNA repair pathway components such as BRCA1. On the other hand, basal-like tumors lack hormone receptors or HER2 and are mostly classified as triple-negative breast cancers (TNBC) for which no molecular-based targeted therapy has been developed yet [8]. In this case, the medical approach is mostly based on chemotherapeutic agents although it showed efficacy only in20% of cases. Nevertheless, despite breast cancer is considered immunologically "cold", preclinical and clinical evidence are showing improved outcomes for patients treated with combinatorial regimens of chemotherapy and immunomodulators. Of the latter, immune checkpoint inhibitors, and in particular those targeting the PD-1/PD-L1 pathways (atezolizumab and pembrolizumab), have been approved by the Food and Drug Administration (FDA) and recognized for the treatment of metastatic TNBC [9]. Tumor-associated antigen vaccines, aimed at triggering the cytotoxic immune against cancer cells have

shown promise in clinical trials, but they are still awaiting FDA approval as breast cancer seems to be particularly refractory from such strategies [10].

Although therapeutic advances in traditional BC treatments improved the therapeutic outcomes in a subset of patients, current approaches are still characterized by limited curative power and significant drawbacks such as high invasiveness, undesired off-target effects, severe systemic toxicity, de novo or acquired multidrug resistance (MDR), and chemo-refractory metastasis. This means that, despite an initial positive treatment outcome, the therapeutic resistance manifests and the tumor can progress again. Therapeutic failure is a multifaceted and complex event, still poorly understood mostly because, as mentioned above, breast carcinomas are singular entities that display different features not only among patients with the same tumor (intertumoral heterogeneity) but even within the same primary tumor, inasmuch can be discerned tumor cell subpopulations characterized by specific phenotypic profiles. Although signs of progress in the stratification of treatments among BC patients, inter- and intra-tumoral heterogeneities, whether spatial or temporal, remain a hallmark obstacle that uniquely affects diagnosis, therapeutic sensitiveness, and patterns of failure by enhancing the range of possible cellular response[11]. Peculiar of BC, regardless of its subtypes is, however, the presence of an impenetrable ECM which hinders the penetration of anticancer drugs leading to the therapeutic failure due to suboptimal exposure.

2.1 BREAST TUMOR MICROENVIRONMENT

2.1.1 CANCER-ASSOCIATED FIBROBLASTS

It is nowadays well established that the TME is fully involved in cancer survival and progression. All the non-cancerous components of the tumor stroma assume a protumorigenic or immunosuppressive role becoming concomitant players in cancer establishment and metastasis. Among the cellular non-malignant factors of the tumorigenic breast stroma, the major contribution is given by cancer-associated fibroblasts (CAFs) which constitute up to 80% of all the activated fibroblasts [12]. In their quiescent state, resident fibroblasts work as sentinels of tissue integrity and are characterized by low proliferative capacity and metabolic activity. However, upon tissue damage, they get activated by various pro-inflammatory factors such as tumor growth factor (TGF)-β and differentiate into myofibroblasts to restore homeostasis [13]. In physiological conditions of tissue regeneration and wound healing, the metabolic and proliferative activity of myofibroblasts is drastically tuned and enhanced, following by the establishment of an inflammatory response mediated by crosstalks with immune cells and in the deposition and remodelling of interstitial matrix proteins. However, when the inflammatory response is prolonged can lead to dysregulations in inflammatory signaling such as a sustained production of cytokines and chemokines, such as tumor growth factor (TGF)-β, VEGF, and C-X-C motif chemokine ligand 12 (CXCL12) but also of connective tissue components, generating a fibrotic and scarring tissue, typical of pathological conditions such as fibrosis and cancer [14]. It is, however, still unclear the origin of such recruited and converted stromal cells but research claims that, besides resident fibroblasts, also bone-marrow-derived mesenchymal stem cells, adipocytes, and endothelial cells can be involved [15]. Although widely investigated, CAFs are still hardly defined either because of their heterogeneity or because of poor understanding of surface-markers specificity. The composition and function of CAFs are in fact dictated by the expression of specific surface biomarkers sets which evolve on tumor progression making their classification into tumor-promoting or tumor-suppressor CAFs even more challenging[15]. *De novo*

expression of α-smooth muscle actin (α-SMA) and fibroblast activation protein (FAP) is the most consolidated hallmark of CAFs that distinguish them from normal fibroblasts. To date, microarray analysis allowed the identification of protumoral CAFs markers of breast cancer that have a prognostic significance such as vimentin, platelet-derived growth factor receptor (PDGFR)—α/-β, podoplanin, cluster of differentiation 90 (CD90), tenascin C, fibroblast specific protein (FSP)-1 [16,17]. Although none of these markers uniquely define CAFs as they do not exclude mesenchymal cell lines, the plethora of ongoing analysis at the single-cell level will certainly draw a more complex picture of CAF functional heterogeneity [13,18]. In general, however, the aberrant proliferation of CAFs is associated with poor prognosis in breast cancer as nowadays it is well consolidated their pivotal contribute in tumor progression, metabolisms, invasion, and metastasis, through their secretome able to modulate and interact with the TME aspects, such as ECM, angiogenesis, immunosuppression, and drug resistance development [19].

2.1.2 HOMEOSTATIC ECM REMODELLING OF THE MAMMARY GLAND

The mammary gland is a compartmentalized structure, mainly composed of three types of tissues, the glandular epithelium, the fibrous stroma, and the fat tissue. The adult female breast contains 15-20 lobes in the glandular epithelium which throughout the milk ducts give rise to several small lobules (acini). The milk ducts are surrounded by epithelial (luminal) and myoepithelial (basal) cells, tightly attached to each other through adhesion molecules such as cadherins and integrins forming tubular structures. These, in turn, are in contact with a dense and continuous layer of ECM mostly made of collagen IV and laminin called basement membrane (BM) which separates the epithelium from the surrounding breast tissues and, most important, ensures polarization of epithelial cells and maintenance of tissue homeostasis [20]. The surrounding component of the ductal structures consists of adipose tissue, stromal tissue, and interstitial matrix, the porous form of the ECM. The latter made predominantly of collagen, and to a minor extent of hyaluronic acid, laminin, fibronectin, and proteoglycans, not only provides support to cellular growth but also to cell adhesion, migration, differentiation. This sectorial architecture of the mammary gland defined by the ECM in both its forms, the basement membrane and interstitial matrix, is a crucial component for the maintenance of the tensional homeostasis which, through the establishment of biochemical and biomechanical signals mainly mediated by focal adhesions, ensures the physiological functioning of the mammary gland [21]. Deregulations in ECM such as focal degradation of the basement membrane, indeed, lead to the cellular detachment from both the epithelium and other cells, thus initiating massive hyperplasia, a precursor of ductal carcinoma in situ (DCIS) which, in the worst case, results in invasive ductal adenocarcinoma (IDC) where epithelial cells spread out across the BM into the surrounding environment or toward distant site via lymphatic vessels [22]. Along the lifetime of a woman, however, the mammary gland composition is subjected to significant fatty and, most of all, fibroglandular tissue remodelling events according to different reproductive stages to respond to homeostatic needs. This consistent remodelling involves over 700 ECM proteins in terms of amount, structure, and disposition, making the breast parenchyma a constantly variable environment characterized by different densities and stiffness [23]. Certainly, this process deeply guides the establishment of biochemical and biomechanical interactions that are created between cells and their surrounding dynamic matrix, determining their fate. In particular, what majorly mutates is the MD. Over time, this ratio has been recognized as one of the major independent risk factors for the development of breast cancer as the relative abundance of stromal and epithelial cells compared to the adipose cells generates high breast density (>75%), increases the risk of breast cancer development by 4–6 fold, and hampers tumor detection by hiding the mass [24].

2.1.3 MALIGNANT ECM REMODELLING OF THE MAMMARY GLAND

In an attempt to determine which, among all the breast gland tissues, is responsible for the increased level of MD, it has been observed that the major contribution is given by the anomalous deposition, cross-linking, and alignment of interstitial matrix proteins within the TME following the activation of stromal cells by tumor-derived factors consistently with the broad body of research claiming the intrinsic involvement of stromal changes in epithelial tumorigenic events [25,21,26]. Among all the ECM proteins, the upregulated secretion and rearrangement of fibrillar collagen is the greatest factor in ECM homeostasis alterations and ECM remodelling in primary tumors [27]. While in healthy soft tissues collagen fibers appear to be curly and parallel to the epithelium, in the proximity of breast cancer tissue they undergo post-translational modifications inasmuch they become aligned and arrange perpendicularly promoting the creation of a protumorigenic environment. Moreover, ECM-modifying enzymes such as lysyl oxidases (LOXs) and prolyl-4-hydroxylases expressed by both tumor cells and CAFs, further promote the alignment and crosslinking of collagen fibers generating a significant increase in stiffness around the tumor [28]. Besides collagens, other ECM proteins in breast cancer stroma such as small molecular mass hyaluronic acid (HA), fibronectin, tenascin C, proteoglycans such as decorin and versican, and laminins, are subjected to alterations of post-transcriptional modifications which generate a protumorigenic environment facilitating tumor cell motility and invasiveness [29]. The intense ECM remodelling is a hallmark of the genesis of dense solid tumors such as breast, pancreas, and prostate and, most important, results in a fibrotic phenotype characterized by increased stiffness and recognized as desmoplastic, strongly associated with poor prognosis and metastasis (Fig.2)[28]. Such desmoplastic ECM remodelling events lead to an overall stiffening of the breast tissue ranging from 0.15 - 0.2 kPa up to 1 - 4 kPa in physiological and pathological conditions respectively, and thus to higher deposition of fibroglandular tissue, high MD and tumor palpability [30,31]. At the macromolecular level, dynamic plasticity and stiffening of the TME lead to integrins-mediated mechanotransduction crosstalk between cancer cells and stromal components. This, in turn, gives rise to a cascade of events aimed at shaping a protumorigenic environment through both the cellular differentiation towards an immunosuppressive phenotype and the oversecretion of soluble factors such as protumorigenic chemokines, cytokines, and cellular stress metabolites, leading to the exclusion of anticancer immune cells and to the recruitment of immune-regulatory cells which promote an anti-immunogenic milieu [32].

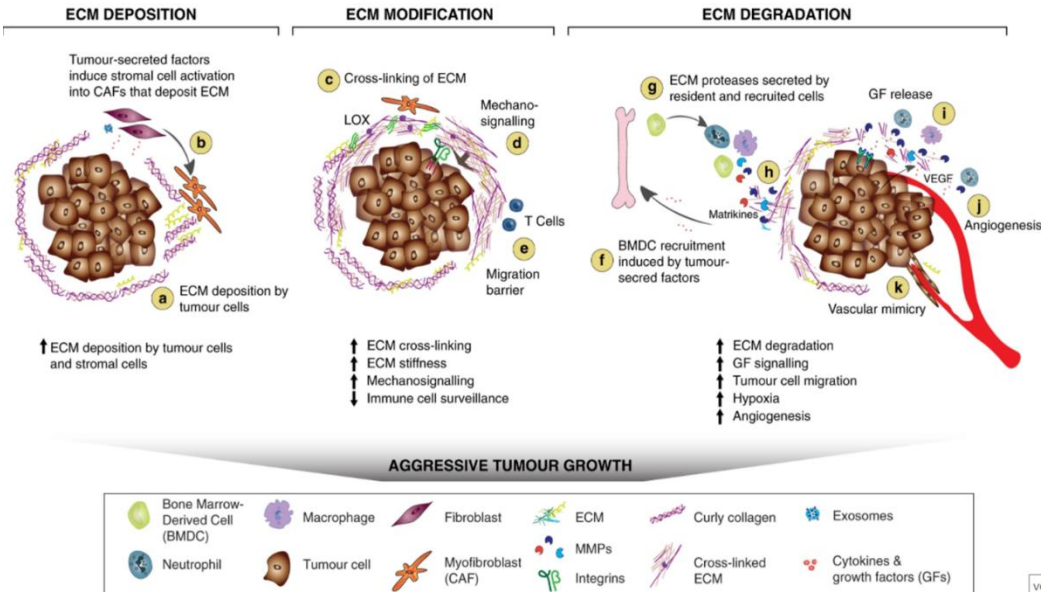

FIG. 2 MECHANISMS OF ECM REMODELLING IN BREAST CANCER PRIMARY TUMOR. Crosstalk interactions between stromal and cancer cells shape a stiff environment which promotes the invasiveness and metastasis of breast cancer. Figure adapted from Winkler et a. [28]

2.1.4 TUMOR VASCULAR NETWORK REMODELLING

While in physiologic conditions the levels of matrix metalloproteinases (MMPs) and their inhibitors, as well as of other enzymes such as LOXs or tissue transglutaminase 2 (TG2), ensure a cyclic homeostatic renewal of ECM proteins by degrading the old ones and allows the synthesis of new ones, in tumor this balance is skewed [33]. The products of the intense cleavage and proteolytic degradation of ECM via MMPs family lead to both the degradation of the BM and the release by neutrophils of growth factors and bioactive matrix proteins, namely matrikines, that induce angiogenic sprouting upon the sense of VEGF concentration gradient, leading to microvascular angiogenesis and enhanced cancer invasiveness [28].
Angiogenesis is defined as the generation of new blood vessels from pre-existing vascular beds and it is induced by cancer cells to sustain the increased metabolic activity and the high demand for nutrients and oxygen [34]. Basically, the formation of new vessels occurs upon imbalances in proangiogenic regulators since angiostatic signals are overwhelmed by the abundant presence of angiogenic factors such as VEGF-A, PDGF-C, interleukin (IL)-8, and basic fibroblasts growth factor (bFGF) secreted by both cancer and stromal cells. The result is the generation of an abnormal, tortuous, thin-walled, irregularly branched, circumferentially enlarged, and leaky capillary-like network characterized by enhanced permeability (with gaps <2 μm in diameter) as tumor-associated endothelial cells proliferate quickly but form weaker tight junctions compared to normal vasculature [35 36]. Even tumor lymphatic vessels are leaky and discontinuous and lack proper fluid drainage and removal of waste products leading to interstitial retention and an overall increase of the IFP. Together, the hyperpermeability of blood vessels and the poor lymphatic drainage give rise to the enhanced permeability and retention effect (EPR), typical of solid tumors and widely investigated as it potentially makes the tumor niche more permissive to drug molecules' entrance. As a consequence, the high IFP, in combination with the solid stress due to unconstrained tumor growth and abnormal ECM deposition, compress the vascular structures which, are already compromised by the lack of hierarchical vascular structure which confers the vascular tone, eventually collapse. Certainly, the occlusion of blood vessels, as well as their tortuosity, has consequences in terms of flow resistance and inadequate afflux of nutrients, therapeutics, and fluctuations in oxygen levels (hypoxia) and acidosis which strongly contribute to MDR and radiotherapy failure [37 38]. Among all, the expression of hypoxia-inducible factor (HIF)-1α is increased upon hypoxic conditions and further supports the transcription of the proangiogenic factors leading to the upregulation of proteins that support the growth and proliferation of hypoxic malignant cells.

2.2 IMPLICATIONS IN BREAST CANCER TREATMENTS

The aberrant structural alterations and stromal content intensification of the breast cancer micro milieu have irreversible implications on the surrounding tissues and strongly contribute to shaping tumorigenic scenarios [39]. Of these, there is the instauration of hypoxic and metabolic alterations towards acidic conditions due to increased IFP and solid stress, that trigger antiapoptotic and drug resistance mechanisms [40,41]. Alternatively, a dense and impenetrable tumor supporting environment is characterized by the formation of a fibrotic stroma which not only constricts blood vessels limiting the supply of nutrients and therapeutics but also constitutes a physical barrier for intratumoral drug molecules transport and penetration [42 43]. In any case, the therapeutic regimes, which ideally should reach the entirety of malignant cells to be efficacious avoiding suboptimal exposure and thus increase the risk of drug resistance, are strongly hindered. Consequently, partial and suboptimal drug exposure can make cancer cells gradually resistant to the therapeutic agent thus contributing to acquired drug resistance and leading to a reverse in their effectiveness.

2.2.1 TRANSPORT BARRIER IN CANCER

Once systemically administered, chemotherapeutic is transported in the blood stream via convection as it is carried by the moving fluid. For a given dose, all parts and organs of the circulatory systems are detrimentally exposed to the drug as solutes are rapidly mixed in the blood flow. Before reaching the tumor cells, however, its concentrations are significantly reduced as they need to overcome several biological and physical barriers. Their effective reaching to solid tumors is in fact conditioned by structural pathophysiological features of the TME such as microvessels integrity and intratumoral flow distribution, on extravascular components such as interstitial and extracellular space, and tumoral and normal cellular components.

2.2.1.1 ABERRANT TUMOR MICROVASCULAR NETWORK

By getting close to the tumor site, the supply of nutrients and therapeutics is particularly modest within the TME as flow does not respect the normal hemodynamic laws due to both structural abnormalities, in which the proportionality of blood vessels diameter and flow velocity is skewed, and to environmental adverse hypoxic and acidic conditions, which instead accentuate viscous flow resistance. Tissue oxygenation is a crucial factor for the therapeutic outcomes as scarce oxygen levels has been positively associated with weaken radio- and chemotherapeutic treatment. Thus, the maximum oxygen diffusion distance of 100 μm from blood vessels becomes a limiting factor as tumor tissue areas out of this range turn out to be hypoxic and thus harder to eradicate. Furthermore, intratumoral blood flow is subjected to fluctuations over periods of ca. 15 minutes generating intermittent hypoxia, further inducing angiogenic events. In general, low microvascular density, tortuosity, and blood vessels compression by the high IFP and solid stress of the surrounding matrix compromise the physiological supply of nutrients, oxygen, and therapeutics with dangerous implications.

2.2.1.2 ENDOTHELIAL WALLS

Another physical barrier at the vascular level is given by the endothelial layer which, as described above, results advantageously in being leaky in tumor tissues due to weaker adherent junctions between endothelial cells which allow the passage of hydrophilic solutes with relatively large size and of nanoparticles (NPs). Nevertheless, the entity of porous endothelium and the relative vascular permeability differ upon the content of collagen of the vessel wall so at inter- and intratumorally levels making the passive drug delivery unreliable and heterogeneous. Across the microvessel walls, drug transport occurs by filtration and this, in turn, depends on the hydraulic conductivity which describes the ease and velocity with which blood can flow into the blood tumor vasculature. More precisely, hydraulic conductivity is defined as the ratio of the fluid flow average across blood vessel wall per unit area divided by driving filtration pressure and it is correlated whether to the intrinsic permeability of the tissue and to the density and viscosity of the blood flow. In this sense, hydraulic conductivity determines the fluid filtration rate through the vessel walls into the interstitial space and it is considered significantly higher in tumor vessels than in normal capillaries.

2.2.1.3 EXTRACELLULAR MATRIX

Once overcome the vascular endothelial barrier and entered the interstitial space, the transport of a solute into the tissue can occur through either convection and/or molecular diffusion according to the presence of a moving fluid or of a concentration gradient respectively. Because of its direct proportionality with a

concentration gradient, diffusion is more effective on shorter distances while convection rate relies on the distance over which the convective fluid flows. The relative contributions of these two transport mechanisms within the tissue, however, vary depending on solute diffusivity and on the interstitial fluid velocity but situations in which both simultaneously occur are also common. In case of solid tumor tissues, in which the interstitial volume is limited due to intense cell proliferative activity and large ECM molecules deposition and a leading flow is missing because of enhanced retention due to lack of drainage, convection is less important [44]. The presence of structural elements within the extravascular TME constitutes physical barriers that limit drug diffusion and hamper their penetration towards cancer cells. Of these, the aberrant ECM of solid tumors constitutes an element of a steric hindrance for molecules and NPs diffusion as their transport depends on the fraction of accessible space reduced by stromal components [45]. The ECM of solid desmoplastic tumors such as breast and pancreatic carcinomas is very dense, impenetrable, protect tumor cell clusters, and takes up space generating longer diffusion distances between the vessel and the tumor cells. Further reduction of free drug is given by the limited supply of blood flow as reported above but also by the binding of drugs to ECM components
In general, the penetration distance within the tissue relies on the strength of the transport mechanisms and the kinetics uptake by cellular components. This is the case of low-relative-molecular-mass (low-Mr) doxorubicin which, although its high diffusivity, has a very limited tissue penetration as it can be rapidly uptaken by normal and tumor cells in the proximity of microvessels. The penetration distance of a solute into the tumor tissue is measured as the rate of diffusive spread over time, relies on the residence time of the drug in the plasma, and is often heterogeneous due to differences in the distances among areas in the tissue and the nearest blood vessels. In general, the diffusion time through a maximum typical diffusion distance from blood vessels of around 100 μm ranges from a few seconds for small solutes to tens of minutes for larger molecules [46].

2.3 CANCER NANOMEDICINE TO ENHANCE THERAPEUTIC POWER OF CURRENT TREATMENTS

In the last three decades, nanomedicine has gained considerable attention in cancer treatment thanks to the possibility to be targeted to specific TME components either reprogramming or normalizing them, thus overcoming the above-mentioned therapeutic limitations and barriers and, most importantly, maximizing the anticancer effect of conventional chemotherapies. Engineered nanocarriers, namely nanoparticles (NPs), such as liposomes and polymeric micelles can be functionalized for controlled, targeted, and enhanced drug delivery to the tumor site [47]. Since their establishment, in fact, nanocarriers have been developed as modulators of chemotherapeutics' biodistribution via whether passive targeting, through the exploitation of EPR effect, or active targeting, through the tuning of their physicochemical properties. Since the clinical approval of PEGylated liposomal doxorubicin (Doxil) in 1995, however, few other breast cancer nanodrugs, among which albumin-bound paclitaxel (Abraxane), have been integrated into clinical standards with beneficial survival outcomes [48]. Notwithstanding the promising results of preclinical studies, cancer nanomedicine showed a moderate success rate in the clinic where, besides some exceptions, no concrete clinical benefit was observed in chemotherapeutic anticancer efficacy except for reduced toxicity. The causes behind the striking discrepancies between the broad spectrum of designed nanosystems and the clinical translation in which just a small percentage of them are approved, are multiple and have different character [49]. From the practical point of view, pharmacological challenges encompass stable biodistribution profile, acceptable side-toxicity, drug release mechanisms, and biodegradation but also production-related challenges such as upscaling, reproducibility, and cost of manufacturing [50].

From the practical point of view, pharmacological challenges encompass stable biodistribution profile, acceptable side-toxicity, controlled drug release mechanisms, and biodegradation but also production-

related challenges such as upscaling, reproducibility, and cost of manufacturing. From the biological point of view, there has been a growing awareness of the poor understanding of both intra- and inter- tumoral heterogeneity revealed by massive sequencing analysis and of the unreliability of the EPR effect as a drug delivery route. The intertumoral heterogeneity introduces, to a great extent, an additional obstacle toward the successful clinical translation of cancer nanomedicine as selecting the right therapeutic combinatorial regimen that specifically fits the patient populations is very challenging [50]. Second of all, nanosystems are still not enough to penetrate tumor biological barriers. De facto, current trends in pharmacological oncology are to investigate combinatorial regimens in which nanocarriers are used to facilitate the intratumoral entrance of the chemotherapeutic component, overcoming the clinical unsuitability of cancer nanomedicine.

2.3.1 SYSTEMIC STRATEGIES TO ENHANCE DRUG DELIVERY

Intratumoral penetration and diffusion of NPs strongly rely on their physical and chemical properties such as size, shape, surface charge, and coating, and lipid solubility. However, tissue penetration-promoting characterization goes to detriment of the targeting power. Although still too complex to be clinically effective and practical, several approaches are currently under investigation in order to find the optimal combination between enhanced NPs penetration and delivery specificity. Among these, size switchable NPs responding to internal stimuli of the TME, such as pH decrease or high expression of MMPs, are still subjected to heterogeneities among tumors and patients [51]. On the other hand, the coating of NPs with ligands that facilitate the intratumoral entering such as lactoferrin and tumor-targeting RGD peptides family objectively showed enhanced penetration and accumulation of NPs within the tumor niche. Alternatively, consistent efforts have been done to develop pharmacological methods aimed at remodeling the physical barrier constituted by TME components for the enhanced penetration of chemotherapy or immunotherapy within the tumor niche. In this view, particular attention has been dedicated to ECM's protein degradation and to tumor cells' apoptosis to reduce intratumoral density but also to blood vessel normalization by means of inhibitors of proangiogenic signaling [52]. Losartan, most of all, has shown its clinical efficacy not only as an antihypertensive agent but also as an antifibrotic agent as it significantly decreased the amount of collagen I, one of the principal components of the stromal barrier [53]. Concerns related to the use of TME manipulating approaches, however, are related to increased risk of metastasis in case of the degraded matrix but also to the undesired activation of parallel protumorigenic pathways given an increased realization of the complexity and the multitude of dynamic interactions between cancer cells and TME [54].

2.3.2 LOCAL PHYSICAL MODULATION OF THE TME

Besides systemic combinatorial therapeutic regimens, cancer nanomedicine penetration can be enhanced by means of locally confined treatment strategies, mostly based on external physical stimuli, which are more suitable for the standardization of controlled treatments regardless of the tumor pathophysiological features.

RADIATION THERAPY: Of these, radiation therapy can enhance drug penetration by damaging the tumor endothelial barrier through beams of intense energy (X-rays). Importantly, radiotherapy combined with nanomedicine has shown to have a mutually beneficial outcome as it enhanced NPs intratumoral infiltration and accumulation and these, in turn, empowered the effect of radiochemotherapy itself [50]. Despite its local application at the tumor site, radiotherapy in combination with nanomedicine has shown a surprising abscopal effect inasmuch tumor antigens released upon radiation exposure were captured by means of nanocarriers and used by antigen-presenting cells to trigger an anticancer immunological response to distant sites [55 56].

HYPERTHERMIA: Since 2013, hyperthermia has been included in the clinical practice for patients affected by recurrent breast cancer for the enhancement of chemotherapy, radiotherapy, and immunotherapy as reported by studies [57] [58]. Hyperthermia induces an increased temperature ranging from 42°C to 45°C to irreversibly damage cancerous tissues while it maintains intact surrounding healthy tissues. The rationale behind the use of hyperthermia together with chemotherapy and/or radiotherapy lies in heat-induced increased blood flow and chemotherapy delivery, as well as inhibition of hypoxia and angiogenesis, and DNA repair [59] [60]. Recently, MR-imageable thermosensitive liposome has been combined with focused ultrasound to trigger the temperature-dependent release of doxorubicin has undergone several clinical trials for the treatment of TNBC [61]. The combination of hyperthermia and ultrasound resulted in be advantageous even for what concerns enhanced drug penetration within the dense tumor niche [62] [63].

PHOTODYNAMIC THERAPY: Another local approach is given by photodynamic therapy and in particular by photochemical tissue penetration (PTP), which allows to temporally and spatially control the drug release and minimize unnecessary systemic cytotoxic exposure. This light-based cytotoxic therapy can be combined with immunoconjugates or nanoconstructs to achieve a localized effect and exploits a photosensitizer molecule which activates upon light exposure producing reactive molecular species or free radical to induce a reaction in the surrounding environment [64]. In the context of augmented drug intratumoral penetration, the generation of singlet oxygen upon photosensitizer excitation damages the epithelial layer and decrease tissue densities allowing enhanced drug concentration within the tumor niche [65].

ULTRASOUND: Alternatively, ultrasonic energy, already employed as a diagnostic imaging technique, has been broadly investigated in the last two decades for its application in therapeutic regimens and it showed to be efficacious in many malignancy conditions such as brain, prostate, breast, and most abdominal organs. The application of ultrasound (US) can whether induce thermal effects such as mild hyperthermia or have non-thermal effects, meaning mechanical or chemical effects on tissues, ensuring anticancer non-invasive drug accumulation within the tissue (Fig. 3) [66]. More recently, gas-filled microbubbles (MBs) have been employed as imaging contrast agents and yielded promising results in theranostics applications. In particular, their use resulted in to be particularly beneficial in what is defined as "sonotherapy", namely MBs-mediated sonoporation, often in combination with nanotherapeutics, such as liposomes, or chemotherapy but also genes [67]. Basically, MBs-mediated US allows spatially confined drug delivery through the generation of transient openings in both the endothelial barrier of tumor blood vessels and of the cellular membrane upon compression and expansion of MBs enhancing endocytosis and vascular perfusion even in highly stromal cancers. A broad body of investigation is reporting that ultrasound energy can be combined with other anticancer therapeutic regimens such as chemotherapy and hyperthermia, to enhance the therapeutic efficacy of these latter ones [68] [69]. Later studies conducted in phase 1 human clinical trial showed concrete benefit in survival rate in a patient affected by inoperable pancreatic ductal adenocarcinoma following MBs-mediated sonoporation in combination with gemcitabine [70]. Additional advantages of this US-based technology have been achieved through the synergistic combination with NPs as it allows controlled and precise drug delivery, but also to overcome limitations usually faced by nanocarriers alone such as limited uptake and accumulation of drugs and antibodies [71]. However, US-mediated drug delivery is an emerging strategy, and more research is needed to unravel the interactions that are established between cells and MBs upon US exposure.

2.3.3 MICROBUBBLE-MEDIATED SONOPORATION

In the last decades, the use of the US for medical applications has been significantly extended to the therapeutic fields through the exploitation of gas filled MBs which, already broadly used in imaging techniques as US contrast agents, nowadays are employed as theranostics tools. Once intravenously administered, MBs (ca. 1-10 μm), indeed, respond to US field through volumetric oscillations that, according to acoustic parameters, not only create harmonic echoes stronger than those of tissues enhancing the imaging contrast but also generate a cascade of mechanical effects of different extent on the surrounding tissues that can be exploited for enhancing anticancer drugs and genes delivery across biological barriers. MBs' shells can be functionalized for prolonged circulation times, targeted therapy, or even loaded with the therapeutic agents, allowing higher localized concentrations and reduced toxic exposure of off-targets tissues. As mentioned above, the most established ultrasound therapeutic mechanism is based on MBs-mediated sonoporation which relies on the generations of fluid streamings upon MBs oscillations and these, in turn, generate mechanical stresses on the nearby tissues allowing transient openings not only in the plasma membrane but also in the endothelial barrier between tight junctions, through which drugs can pass. Lately, the biomechanical effects of MBs on tissues have been furtherly investigated thanks to the implementation of several in vitro models that allowed the observation of heterogeneous cellular responses upon sonoporation such as transients of calcium ions, depolarization of plasma membrane potential, temporary rearrangement of actin, and tubulin cytoskeleton, cell shrinkage and nucleus contraction. The behavior of MBs, and thus their effects on tissues and therapeutic potential, however, strongly depend on MBs physical properties such as size, resonance frequency, and shell shedding but also on acoustical and environmental factors that cannot always be recapitulated in vitro. Among the acoustical parameters, acoustic pressure is what determines MBs oscillations intensity in stable and inertial cavitation. While the stable cavitation occurs at lower acoustic pressures and makes MBs behave linearly, with expansion phases equal to the compression ones, in the inertial cavitation oscillation amplitude increase to the point that the pressure exerted by the streamings overcomes that of MBs leading, eventually, to their collapse [72]. Sonoporation, however, can occur whether in the stable and in the inertial regimens due to microstreamings and microjets respectively. In both cases, cells are subjected to shear stresses that temporarily or permanently disrupt the biological membranes. Other acoustical parameters that affect drug uptake mechanisms are pulse duration, pulse repetition frequency, and sonication time. Tuning such parameters can favor endocytosis-, sonoporation-, or sonoprinting-based drug delivery mechanisms. In addition to these, also the properties of the surrounding environment should be considered to predict MBs behavior such as the presence of nearby rigid (in vitro) or viscoelastic (in vivo) boundaries, the vessel size, and thus the distance between cells and MBs, and the viscosity of the fluid.

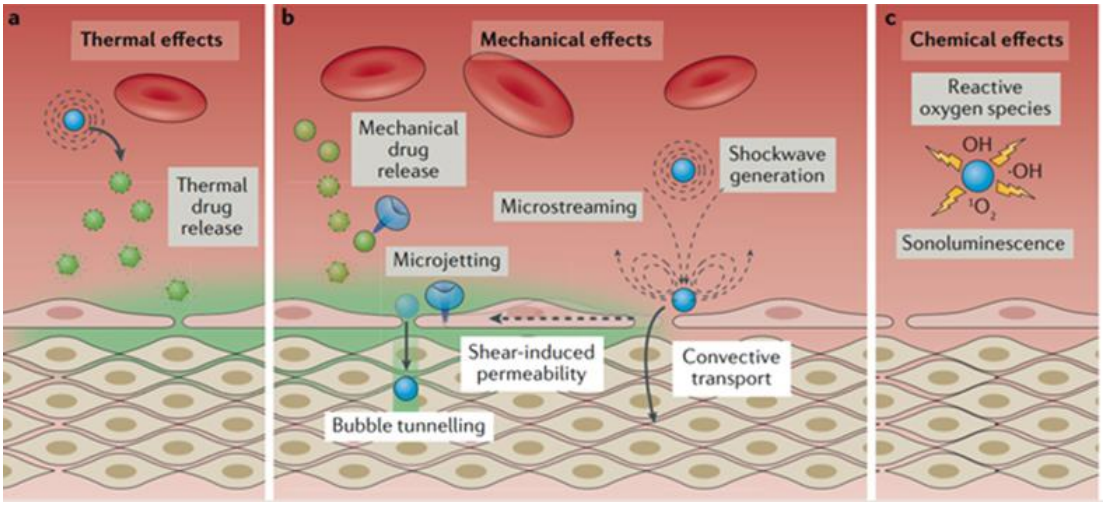

FIG. 3 MICROBUBBLES-MEDIATED THERAPEUTIC EFFECTS UPON ULTRASOUND EXPOSURE; BESIDES MECHANICAL EFFECTS, THE THERAPEUTIC EMPLOYMENT OF MBs-US CAN BE BASED ON OTHER MECHANISMS SUCH AS THE TRIGGERING OF CHEMICAL EFFECTS OR VIA HYPERTHERMIA. Figure adapted from Stride and Coussios [72]

2.4 THE IMPROTANCE OF PRECLINICAL INVESTIGATION MODELS

Considerable efforts are still made to unravel the complex and broad network of interactions between cancer cells and the TME in order to identify vulnerabilities and pivotal crosstalks that promote tumor progression. Likewise significant are the attempts to make the physical barrier more accessible to anticancer drugs and thus to develop approaches for the enhancement of drug intratumoral penetration. Their assessment and efficacy, however, requires accurate preclinical models that can allow the observation and comprehension of biological interactions and reactions and, eventually, the identification of limitations and strengths of each therapeutical strategy. Furthermore, given the broadness of cancer implications in terms of resistance and migration, and thus the need to adopt a multivalent approach in cancer treatment, the importance of having reliable and predictive preclinical models could lead to the optimization of synergistic, effective, and possibly personalized combinatory therapeutic regimens. Even the diagnostic field can take advantage of these technologies since they can be used to detect biomarkers that describe tumor progression [73]. All these aspects are of great interest to drug developers and to the pharmaceutical industry since once that cancer targets have been identified, they can use in vitro models as relatively fast high-throughput drug screening platforms. In this way, molecularly targeted therapies can be validated and optimized with a significant reduction in costs and time compared to in vivo models [74]. As matter of facts, an average time of 7.3 years (range, 5.8-15.2 years) and an amount that ranges from $320.0 million to $2.7 billion have been estimated for the development of a single new anticancer drug [75]. The mechanism of action, the pharmacokinetics, the anticancer activity, and the safety of the testing drug are preliminarily assessed in preclinical trials that cover an extensive part in the process of drug development. From preclinical trials to phase III there is an increasing trend in time and resources, eventuating in significant costs once clinical trials are reached [76]. Despite a great deal of effort in producing preclinical in vitro models that best recapitulate human biology and pathophysiology, there are still remarkable limitations that imply a poor translation from preclinical to clinical trials [77]. As a matter of fact, compared to all therapeutic areas, oncology presents considerably higher drug attrition rates [78]. Although the recapitulation *in vitro* of organ-like microarchitectures has enabled invaluable findings in oncological fields so far, many key hallmarks involved in complex tumor mechanisms, such as drug resistance, still need to be elucidated. Both pharmaceutical and academic laboratories are highly committed on the improvement of three-dimensional (3D) *in vitro* cell cultures by integrating physiologically relevant elements in order to be able to perform

realistic pharmacodynamic studies [79]. Finally, it is estimated that the market of 3D cell cultures for cancer research will reach $1.4 billion by 2022 [80], suggesting that high hopes are placed into future cancer 3D *in vitro* models.

2.4.1 PRECLINICAL MODELS TO STUDY DRUG PENETRATION IN BREAST CANCER

As reported above, a broad spectrum of tumor-related factors contributes to breast cancer therapeutic failure in terms of both drug resistance and disease relapse. Besides the mechanisms of intrinsic or acquired multidrug resistance common in most epithelial-like cancers, breast cancer is intrinsically characterized by biochemical and physical properties which add complexity to the prediction and successes of therapeutic treatments. Breast cancer cannot be univocally defined as it encompasses a broad range of pathological conditions with as many drug sensitivities and therapeutic outcomes according to the presence or less of hormone receptors. Besides the compromised and abnormal tumor-related vasculature which does not allow the proper transport of drugs into the tumor site, breast desmoplastic stroma constitutes a real physical barrier as it strongly hampers the adequate exposure of cancer cells to the macromolecular drug candidates and NPs, limiting their diffusion and penetration and thus contributing to increased acquired drug resistance. All these physical attributes of the breast TME should be considered and deeply investigated to understand to which extent they hinder therapeutic effectiveness and to develop targeted therapies.

2.4.1.1 IN VIVO

In vivo models can allow the evaluation of drug pharmacokinetics and pharmacodynamics but still are not reliable models because of species-to species variability, meaning that they do not reflect human metabolic rate, tumor-suppressor pathways, immunogenicity, and cytogenic profile. De facto, it is also difficult the identification and the control of specific pathways and mechanisms involved in the tumor response upon therapeutic regimes. Moreover, animal models are time and costs consuming and currently, with the ambition to decrease the amount of animal experimentations, there are significant ethical issues related to the use of animal models for drug screening. More recently banks of explant have allowed the availability of ex vivo cultures made of animal- or human-derived tumor slices, sometimes integrated into gels, which have been used to study cancer biology and drug sensitivities. Such models can be a valuable tool for the development of personalized medicine as they present the original phenotype and heterogeneity but are less applicable to unravel basic drug resistance mechanisms as patient-dependent variance among tissue samples makes it difficult to standardize and compare experimental readouts.

2.4.1.2 IN VITRO

2D Although their broad employment as the drug's in vitro cytotoxicity tools, the conventional in vitro two-dimensional (2D) tissue cultures are nowadays broadly recognized to be unsuitable for anticancer drug investigations since, apart from allowing ease of use and of manipulation of cell-culture substrates in a non-physiological setting, they fail to recapitulate the complex biological environment. They are, indeed, time and costs effective platforms that allow the observation of specific singular pathways but the lack of a three-dimensional (3D) network induces an unreliable cellular behavior and a distorted gene expression compared to the in vivo situations thus failing to mimic the original phenotype. Most important, 2D cell culture monolayers cannot recapitulate the spatial, temporal, biological complexity of the TME barriers and thus the actual diffusion and penetration of larger drug molecules and the response of tumor cells.

2.4.1.2.1 3D MODELS

To address these challenging three-dimensional (3D) *in vitro* models have been created to mimic and recapitulate one or more pathophysiological aspects in controllable settings. Advances in biomaterials and biofabrication allowed the developments of complex models that mimic organ-like architecture and encompasses patho-physiologically relevant elements, such as gradients, dense stroma, interstitial flow, and patient-derived cells. Besides being versatile tools for disease modelling, these advanced in vitro platforms are a very promising aids in the identification auxiliary of therapeutic targets for the enhanced antitumoral drug delivery. In the context of drug resistance mechanisms in breast cancer, the most consolidated in vitro platforms are given by multicellular spheroids, biomaterials-based models such as scaffolds or hydrogel, and microfluidic chip-based models. These design possibilities range from the simplest case of spheroids which are scalable, inexpensive, high-throughput drug screening tools those allow the understanding of basic disease mechanisms to more complex and harder to control platforms like microfluidic chips. Certainly, the complexity of the model can be increased in order to achieve more physiologically relevant constructs, for example through the incorporation of a relatively complex vascular network or immune cells) but this goes in detriment of even lesser controllable variables and more accurate and in-depth characterization. Given the broad complexity of in vivo breast cancer architecture and biology, preclinical 3D in vitro models should be thus implemented according to the specific research question keeping the level of complexity at the minimum to ensure their predictive power, robustness, and reproducibility.

2.4.1.2.2 MULTCELLULAR SPHEROIDS

Multicellular spheroids are relatively inexpensive, easy, and high-throughput cancer models in which homotypic or heterotypic cells are densely clustered together to form 100-600 μm aggregates thus showing a 3D cellular organization and favouring cell-cell interactions. Their tunable size allows the observation of different events. Smaller spheroids, 100-200 μm, for example, are used for investigating cellular and materials interactions but also to test the cytotoxicity of anti-cancer drugs.
On the other side, larger aggregates ca. 200-600 μm, have been created for the reproduction of more aggressive phenotypes and are usually characterized by the presence of transport gradients and proliferation rim inasmuch they present a necrotic and hypoxic core, in which cancer cells are in a quiescent state, and a proliferating outer shell. The presence of a hypoxic core and thus the expression of HIF-1α further increased the resistance to doxorubicin and 5-fluorouracil. Spheroids are invaluable tools for investigating the effects of intercellular interactions in tumor progression but also the uptake and penetration of NPs and therapeutics, and the sensitivity of monoculture and co-culture spheroids [81]. Multicellular spheroid models, however, fail to recapitulate all feature of solid tumors characterized by a high desmoplastic reaction since they do not incorporate the extracellular milieu and cells-matrix interactions thus do not incorporate resistance provided by physical barriers involved in drug resistance such as the vascular barrier and ECM.
Such limitations associated to spheroids have been recently highlighted by Brancato et al. in a study in which the efficacy and uptake of doxorubicin (DOX) has been compared in two breast cancer models, one based on mono- or co-cultures spheroids, and another based made of 3D gelatin scaffold-based microtissue (3D-μTP). In both models, they integrated breast cancer cells (MCF-7) and CAFs able to produce endogenous ECM. In this way they could observe differences in cytotoxicity effect, diffusional transport properties and protumorigenic protein expression. Interestingly, they found different tumor-associated biomarkers expressions, higher diffusion coefficient of DOX and lower cell viability in the 3D-μTP compared to the spheroid model [82].

2.4.1.2.3 BIOENGINEERED 3D MODELS

A more engineering-based approach to recapitulate and manipulate cell/ECM-based aspects in physiologically relevant settings is driven by biomaterials-based models, classified in scaffold-based, hydrogel-based, and biofabrication-based strategies (Fig. 4) [83].

Advances in biomaterials allowed the employment of polymer scaffolds and hydrogels, whether natural and synthetic, in which cells or multicellular spheroids can be seeded on or embedded in, respectively. Solid scaffolds are generally employed for migration and metastasis studies of invasive breast cancer cell lines. Hydrogels, instead, are an alternative type of scaffolds that can be distinguished due to their higher water content and swelling behaviour due to their hydrophilic properties. Thanks to their porous crosslinked structures, they promote nutrient and oxygen diffusion as well as drug delivery and are suitable for investigating heterogeneity and tumor complexity thanks to their versatile production methods and components, and ability to incorporate multiple cell types. Ideally, both these engineered 3D models should provide mechanical, biochemical, and physical cues appropriate for cell adhesion, proliferation and differentiation, but also migration. Usually, in the case of breast cancer models, tumor-stroma interactions are intrinsically recapitulated in naturally derived polymers such as silk, collagen, gelatin, agarose, hyaluronic acid, alginate, and chitosan. These polymers, however, are characterized by low mechanical properties and batch-to-batch variations which affect their reproducibility. Alternatively, by means of BM extracts and decellularized ECM (dECM) it is possible to reproduce the natural ECM maintaining the protein content, the biochemistry, and in the second case the structure. Matrigel is broadly employed product extracted from murine Engelbreth-Holm-Swarm (EHS) tumor cell cultures, and contains to a greater extent laminin, followed by collagen IV, enactin, and growth factors. The amount of such protein content, however, can vary from one batch to the other affecting experimental readouts and the reproducibility of the model. Synthetic polymers, on the other side, can be easily reproduced with tunable mechanical, degradation, and structural properties while they must be functionalized in order to present bioactive groups observed in natural tumor ECM, such as RGD (Arg-Gly-Asp) peptides, that facilitate protein adsorption and cell adhesion. For mimicking breast cancer tissues, the most employed synthetic polymers are given by polyethylene glycol (PEG), polycaprolactone (PCL), polyurethane (PU), and polylactic acid (PLA). Eventually, TME mimicking scaffold- or hydrogel-based models can be produced via the employment of biofabrications techniques such as 3D bioprinting and stereolithography, or through the development of microfluidic devices. The application of biofabrication techniques for 3D cell cultures enable well-defined cell patterning in terms of composition and architecture, high reproducibility, and the realization of relatively thick and complex constructs thanks to computer-aided 3D geometries. The possibility to integrate multiple

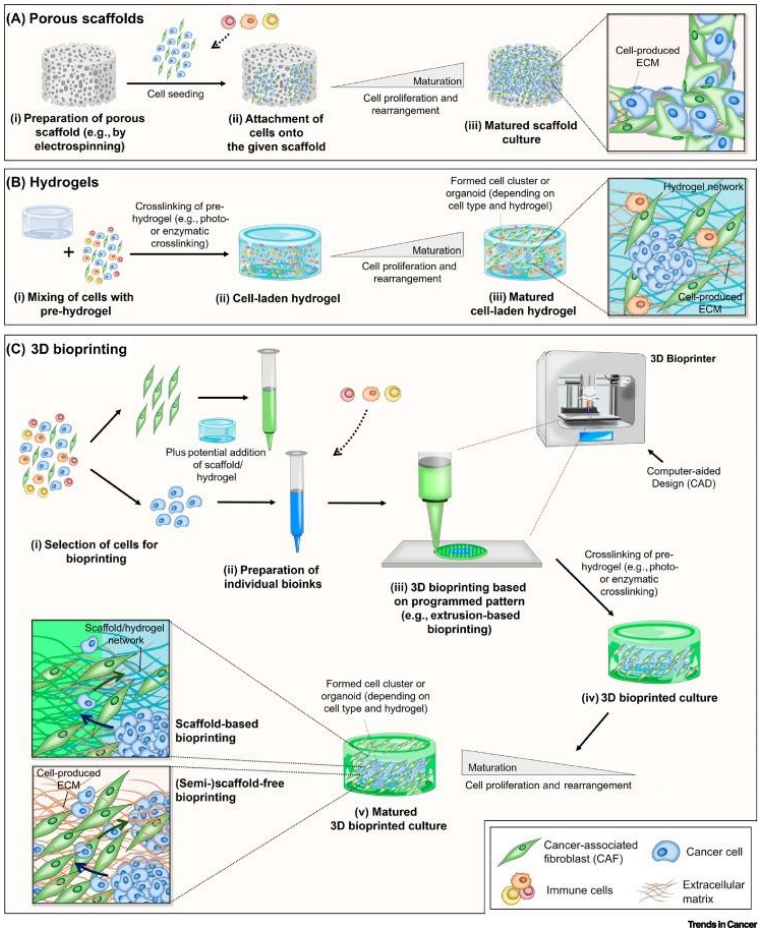

FIG. 4 SCHEMATIC REPRESENTATIONS OF DIFFERENT CELL/ECM-BASED MODELS. Figure adapted by Rodrigues et al. [83]

bioink cartridges allows to combine multiple biomaterials within the same scaffold and, most of all, to introduce additional biological complexity as control over spatial and temporal deposition of cells, either in the forms of organoids or spheroids, proteins, growth factors, and other biologically active molecules. Bioprinting techniques thus enable the creation of larger tumor tissues and eventually, their interations with other surrounding tissues. For this reason, they have been widely employed to study many aspects of breast cancer such as drug resistance, the effect of stiffness on drug response, and metastatic breast cancer to the bone. Microfluidic-based chips represent the most complex of engineered TME breast and as they include many aspects such as three-dimensional organization, intercellular and cell-stroma interactions, the presence of diffusion, oxygen and nutrients gradients, vasculature, and thus flow rates. These microfluidic systems can recapitulate both static and dynamic regimens enabling the observation of biochemical, mechanical, and hydrodynamic cues such as shear stresses, mechanical strains, interstitial fluid flows, hydrostatic pressures as found in vivo. More interestingly, they are suitable for multiplexing with other parallel microfluidic systems allowing high throughputs.

2.4.2 MODELS FOR SONOPORATION

The use of animal models for the study of MBs-mediated sonoporation aimed at controlled drug delivery has, to a great extent, yielded important insights, such as MBs-US parameters optimization in terms of maximization of the therapeutic efficacy and estimation of undesired side effects. Nevertheless, *in vivo* models do not allow the observation of specific mechanisms underlying cell-MB interactions or their effect on tissue at the macromolecular levels either because of the complexity of the organisms in their entirety but also because current microscopy-based techniques cannot obviate the lack of transparency of in vivo settings, making real-time measurements very challenging whilst they could unravel crucial questions. It is, in fact, still unclear which are the mechanical stresses and the biophysical effects induced by the action of MBs at both the MB-cell and intracellular levels. Also, the lack of standardized investigation platform and protocols and thus of therapeutic acoustical parameters generates discrepancies among experimental results Even in *in vitro* models, however, the issues related to length- and time-scales over which these events occur still remain. The dynamics of MBs and their mechanical effects on cells are, indeed, phenomena observable at the micrometer (or even less) length scale, and ranges from nanoseconds to microseconds. The biological effects of MB such as drug diffusion and uptake can, on the other hand, be a matter of seconds to minutes and can be appreciated in the nanometers (across the cellular membranes) to micrometers (within the tissues) range [84].
Several experimental design and set-up can be employed as tools of investigation, from single cells and 2D monolayers to 3D cell cultures and microfluidic chips. As in the case of breast cancer *in vitro* models, and mostly in the case of multidisciplinary subjects like sonoporation-based drug delivery, the implementation of the *in vitro* cellular model and the level of its complexity strongly must rely on the research question since still, it is not possible to integrate all the biological nor physical aspects found in the *in vivo* environments.

2.4.2.1 SINGLE CELLS AND 2D CELL POPULATIONS FOR MBs-US STUDIES

Advances in biotechnologies allowed the development of tools able to isolate and trap single cells that can be used as 2D in vitro models for investigating the impact of a single MB on a single cell over time and space and, thus, to focus on membrane poration, cytoplasm leakage, and cell lysis upon cavitation. This closer look yields interesting insights related to cell fate, to the mechanics and rheology of cellular

membranes but offer, perhaps, more relevant understanding about the acoustics and physics of cavitation itself.
For the same purposes of unravelling MBs-cellular interactions, 2D cell culture monolayers on commercially available platforms such as the OpticCell chamber can also be employed. The most employed monolayer systems consist, indeed, in seeding cells on microchannels exposed to flow to simulate shear stresses and hemodynamic drug delivery. Besides considerations about the effect of the distance between MBs and the cellular substrate, these models have been used to investigate the delivery effectiveness of molecules and, in particular, the gene transfection potential of plasmid coated MBs.
Although these approaches can offer invaluable insights for what concerns the definition of cytocompatible acoustical parameters and the optimization of cell-MBs interactions by, for example, the functionalization of MBs surface, they have consistent limitations. As mentioned above, the fact that these models do not recapitulate a 3D environment has significant consequences in terms of cellular phenotype and thus treatment response. Furthermore, the amount of cellular detachment and other considerations about cellular membrane reactions are also questionable due to the substrate physical properties on which cells are seeded which induce fictitious mechanotransduction affecting, even in this case, the therapeutic response. The presence of a substrate also disturbs the acoustical signal and the MBs behaviour and dynamics, compromising whether the resonance frequency and the amplitude of oscillation of MBs.

2.4.2.2 3D IN VITRO MODELS FOR MBs-US STUDIES

The importance of integrating elements of complexity and biological relevance in 3D in vitro models for therapeutic sonoporation studies is nowadays widely recognized, needed, and pursued. An important aspect that should be considered in drug delivery studies is the presence of tumor and stromal cells, as well as a relatively dense fibrotic ECM. As reported above, multicellular hetero- and homo-spheroids are invaluable tools that can yield important information about drugs penetration and are, more often, embedded into hydrogels-based scaffolds to mimic the ECM environment surrounding tumors in terms of proteins, biological cues, and mechanics. Even in this field, advances in microfluidics contributed significantly to the in vitro recapitulation of biological barriers encountered by therapeutics, MBs, and nanocarriers in vivo. As a matter of fact, organ-on-chip models used in MBs-mediated sonoporation studies successfully recapitulated blood vessels, tumors, and the blood-brain barrier. In particular, the integration of endothelialized channels within ECM-like hydrogels would permit the observation of MBs behavior and sonoporations under flow conditions but also the formation of a tight-junctions opening in the vascular barrier, and the potential extravasation and diffusion within the surrounding environment upon inertial cavitation. Furthermore, it would allow the characterization of MBs hydrodynamic in viscoelastic medium and deformable boundaries, and the definition of parameters for which US-induced cellular damages are not reversible due to violent shock waves and jetting. These in-depth observations could be exploited to optimize the MBs surface, composition, and concentrations but also US exposure to enhance drug delivery powers while minimizing adverse side effects. As far as we know, so far, the 3D in vitro models develop for MBs-US investigation are summed up below [Tab.1][Fig.5].

	DESIGN	AIM	BIOLOGICAL COMPLEXITY	REF
A	384-WELLS ORGANO-PLATE MICROFLUIDIC VESSEL-ON A CHIP IN SERIES	ACOUSTIC CHARACTERIZATION FOR US-MEDIATED DRUG DELIVERY	- ENDOTHELIALIZED CHANNEL - ECM-LIKE GEL - PERFUSABLE	[85]
B	MICROFLUIDIC VESSEL ON A CHIP	VISUALIZATION OF MICROBUBBLE/ULTRASOUND DEPENDENT DRUG DELIVERY TO MICROVASCULATURE	- (HUMAN) ENDOTHELIALIZED CHANNEL - HUMAN FIBROBLASTS - FIBRIN MATRIX - PERFUSABLE	[86]
C	3D MICROVASCULAR NETWORK WITH CHANNELS IN PARALLEL	MBs-VASCULAR ENDOTHELIUM INTERACTIONS FOR US-MEDIATED DRUG DELIVERY	- (HUMAN) ENDOTHELIALIZED CHANNELS - COLLAGEN GEL - IN PARALLEL VASCULAR NETWORK	[87]
D	CELLULOSE FIBERS COATED WITH CHITOSAN AND GELATIN BASED-SCAFFOLD	MB-MEDIATED INTRACELLULAR NPs DELIVERY	- MOUSE FIBROBLASTS - HYDROGEL-BASED SCAFFOLD	[88]
E	CLINICELL	OPENING OF ENDOTHELIAL CELL–CELL CONTACTS DUE TO SONOPORATION	- 2D MONOLAYER - HUMAN ENDOTHELIAL CELLS	[89]
F	LAYERED ACOUSTOFLUIDIC RESONATORS	MBs DYNAMICS, MICROSTREAMING VELOCITY FIELD, ACOUSTIC EMISSION, CELL-MBs INTERACTIONS	- HUMAN BASAL EPITHELIAL CELLS - PERFUSABLE - 2D MONOLAYER	[90]
G	PDMS MICROFLUIDIC TRAP ARRAY	INVESTIGATE MBUS-MEDIATED ENHANCED DOX DELIVERY TO CANCER SPHEROIDS	- HUMAN TUMOR SPHEROIDS - PERFUSABLE	[91]
H	OPTICELL CONTAINING ACOUSTICALLY RESPONSIVE HYDROGEL-BASED SCAFFOLD	PROPERTIES OF THE ACOUSITCALLY RESPONSIVE SCAFFOLD	- FIBRIN SCAFFOLD - MOUSE MESENCHYMAL STEM CELLS	[92]
I	PDMS MICROFLUIDIC SYSTEM	CHARACTERIZATION OF THE ENHANCED ENDOTHELIAL PERMEABILITY MB-ENHANCED US-INDUCED CAVITATION	- HUMAN ENDOTHELIALIZED CHANNEL - PERFUSABLE	[93]

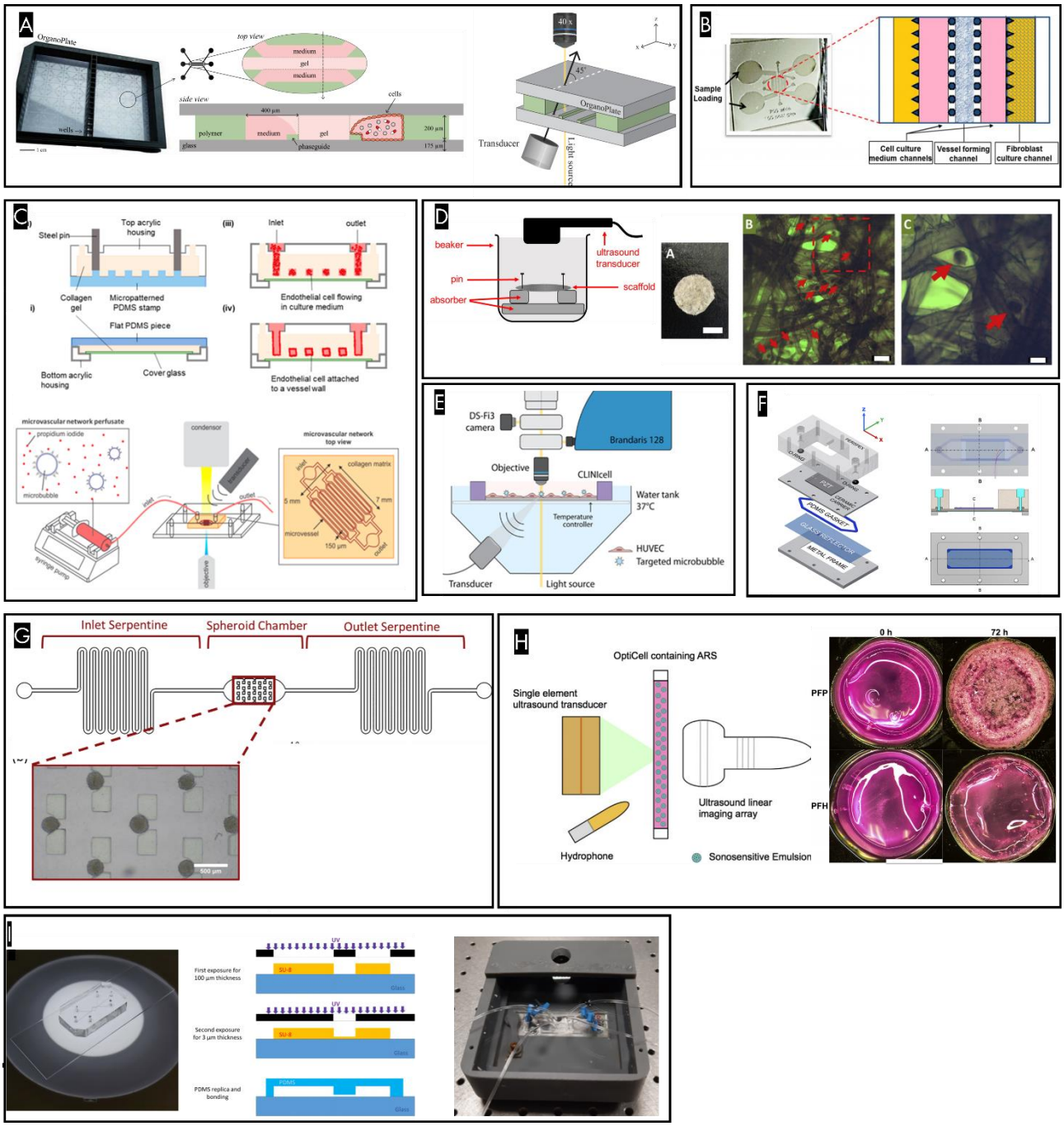

FIG. 5 CURRENT IN VITRO 3D MODEL FOR INVESTIGATING ACOUSTIC PARAMETERS OR DRUG DELIVER MECHANISMS OF MBS-US. Although some of these models is based on hyrogel-based scaffold for endothelial cells, they lack biological complexity in terms of organ-like architecture and thus biological barriers, and offer a too semplicistic, although highly reproducbiibl in vitro platforms.

3.1 SIGNIFICANCE OF THE STUDY AND RESEARCH QUESTION

Nowadays, a broad body of research is engaged in the development of new biomaterials for in vitro tissue simulation or in the advancement of biofabrication techniques aimed at the realization of organ-like architecture constructs. The recapitulation in vitro of relatively complex and functionalized microtissues allows the focused observation of biological processes and interactions which are hardly discernible in vivo models due to the involvement of a multitude of cellular pathways, to the lack of specificity, and to imaging issues. Moreover, the implementation of faithful tissue-like models allows the screening and the evaluation of penetration and transport of therapeutic combinatorial regimens for cancer treatments and thus a more accurate translation of their potential into the clinic. In the acoustic field, such investigation platforms together with advanced imaging tools, like ultra-high-speed camera and high-speed fluorescence imaging, allow the direct observation of physical phenomena, the comprehension of MBs-cells interactions, and the mechanisms at the basic of sonoporation-mediated drug delivery. Notwithstanding, the realization of in vitro models suitable for both biological and acoustical applications come with challenges inasmuch a broader spectrum of requirements needs to be considered and respected in order to develop investigation platforms adequate for biological, optical, and acoustical set-ups. To the best of our knowledge, as of now, the developed in vitro models for MBs-mediated sonoporation studies are reduced to the integration of 2D cell monolayers or, the more complex, integrate endothelialized 3D channels in microfluidic devices surrounded by a cell-free ECM-like matrix.
As reported above, the level of complexity of in vitro models, for biological and acoustical investigations is dictated by the research question requirements. Since these models have focused on the study of MBs-single cells or MBs-endothelial layer interactions, most of them present a moderate biological relevance as they include, most of the time, just an endothelialized microvascular network, sometimes incorporated into a cell-free ECM-like matrix.

The goal of this project is thus to implement a 3D *in vitro* breast cancer microtissue suitable for both biological and acoustical applications. In particular, the model should allow the evaluation of hindering effects given by physical barriers associated with the desmoplastic breast carcinoma on the intratumoral transport of different molecules. The model should be also adequate for the observation of acoustical phenomena such as MBs cavitation and for the assessment of the enhanced extravasation and diffusion of molecules within the tissue by means of MBs-US.
Compared to the state-of-the-art, this model presents a higher level of biological complexity as it allows the integration of multiple cancerous and non-cancerous cellular components, high stromal density, perfusable endothelialized channels with different patterns, a stable and versatile structure with significant thickness, and importantly, clinical relevance, without neglecting optical and acoustical transparency in a very specific range of timescales and length scales.

3.2 GENERAL AIM AND SPECIFIC OBJECTIVES

This project, aimed at the implementation of a 3D in vitro breast cancer microtissue (BCM) suitable for the study of molecules transport with or without the MBs-mediated US, was conducted following a multidisciplinary approach.

We hypothesize that the diffusion distance of different molecules within the tumor microtissue is hampered by the presence of a continuous endothelial barrier and even more limited in the presence of a dense stromal barrier with high cellular density.
Based on this, we hypothesize that the application of MBs-mediated US can enhance the extravasation through the endothelial barrier and the diffusion distance of molecules within the tissue.

The process phases and the relative research questions are summarized below:

I. MODEL DESIGN, IMPLEMENTATION & OPTIMIZATION

a. Can the 3D hydrogel-based scaffold recapitulate the densely packed breast tumor?
b. Does the 3D hydrogel-based scaffold include the optical and acoustical requirements for being employed in the study of cavitation effects and sonoporation?

i) Hydrogel composition study:

Stability: mechanical stability, stable crosslink, channel integrity
Biocompatibility: cell viability
Transparency: optical clarity

ii) Mould design

iii) Cell seeding and channel endothelialization

iv) Hydrogel characterization: scanning electron microscopy (SEM) and dynamic mechanical analysis (DMA)

II. MODEL CHARACTERIZATION

a. Is the model suitable for 3D cell culture and acoustical set-up?
b. Does the model present tumorigenic trends?
c. Is the model clinically relevant?
d. Can the model recapitulate desmoplastic trends?

i) Acoustical and optical characterization

ii) Biological characterization:
Gene expression
Tumorigenicity and clinical relevance
Organ-like architecture

iii) Mechanical characterization

III. THE EFFECT OF PHYSICAL BARRIERS ON MOLECULES TRANSPORT

a. Does the model recapitulate the effect of physical barriers on molecules diffusion within the TME?
b. Does the model mimic the different impediments of tissue barriers on molecules of different sizes?

i) Effect of different physical barriers on molecules with different sizes [Tab. 2, left]:

IV. MBs-MEDIATED US

a. Does the model allow for the observation of MBs cavitation phenomenon inside the channel?
b. Does MB-mediated sonoporation enhance the extravasation and diffusion endothelial barrier?

Effect of MBs-US on molecules diffusion through the endothelial barrier [Tab. 3, right]:

EFFECT OF PHYSICAL BARRIER AND MOLECULES SIZE ON MOLECULES TRANSPORT			
	Cell-free	Endothelial (3T3-)	Stroma (3T3+)
RhodB	◆	◆	◆
FITC10kDa	◆	◆	◆
FITC70kDa	◇	◇	◆
Silica NPs	◇	◇	◆

EFFECT OF MBs-US ON TISSUE TRANSPORT BARRIERS			
	Cell-free	Endothelial (3T3-)	Stroma (3T3+)
NO MBUS	◆	◆	
WITH MBUS	◆	◆	

TAB. 3 APPLICATIONS SET-UP SCHEME; Left table: study of transport of molecules according to their size and of the biological diffusion barrier involved, cell-free hydrogel, endothelium, and stroma respectively. Empty marks indicate that the perfusion was conducted even in those conditions, but a complete dataset of triplicate is missing; Right table: FITC Dextran 10 kDa was tested for the MBs-US application in which its transport through both, cell-hydrogel and the endothelial barrier, was evaluated with or without treatment of MBs-US.

3.3 RESEARCH APPROACH

3.3.1 TRI-CULTURE SYSTEM

In order to establish a biologically relevant 3D *in vitro* breast cancer model, a murine cancer cell line (4T1) was cultured in spheroid models. In a mouse model, 4T1 cells are used as a syngeneic model for preclinical TNBC studies. TNBC is a highly aggressive and invasive subtype, diagnosed in more than 17% of breast cancer cases.
The high cellular density of murine fibroblasts (NIH-3T3) was used because of their excellent properties, such as high expansion capacity, easy handling, and good availability to mimic a stroma-dense TME. In this multicellular platform, 3T3 fibroblasts and 4T1 cancer spheroids (on day 3) of cell culture were embedded in ECM-like hydrogel solution (GelMA/Matrigel) in the pathophysiological-like ratio (5:1) [81]. Immortalized mouse heart endothelial cells (H5V) were used to endothelialized the channel. The resulting triculture-based microtissue was grown for 10 days, monitored, and characterized in terms of growth, viability, and cell distribution, throughout the entire period of culture in order to identify the best culture time point for diffusion assessments.

3.3.2 HYDROGEL CHOICE AND CHARACTERIZATION

The choice of gelatin methacryloyl (GelMA) has been dictated by its excellent suitability to reproduce a 3D ECM-like environment in terms of both inherent biological signals of gelatin and tunable biomechanical properties but also because of its optical transparency. GelMA is obtained by modifying gelatin, a hydrolyzed form of collagen, through the replacement of many amine-containing groups on side chains by methacrylate groups. However, most amino acid motifs, such as arginine-glycine-aspartic acid (RGD) sequences and matrix metalloproteinases (MMPs) digestion sites, are not affected by this modification. This ensures cell adhesive properties of GelMA hydrogels and their enzymatic cleavage by type I and II collagenases. The presence of methacryloyl groups makes GelMA a photopolymerizable biomaterial, which means that, once that a photoinitiator (PI) is added, it covalently crosslinks when exposed to UV light. This rapid polymerization takes place at mild conditions (natural pH, room temperature, etc) and provides adjustable mechanical features. GelMA owns great mechanical tunability over physiological-like ranges of stiffness, pore size, and density, providing an excellent microenvironment for cells mimicking the native ECM. GelMA concentration, the degree of functionalization, UV intensity and exposure are tunable parameters that determine the final biological and mechanical features [94].

As BC microenvironments are usually well-recapitulated with collagen-based models, several attempts to generate a GelMA and collagen hydrogel were done [95] [46] [Supplementary material, Fig.1S]. Nevertheless, GelMA and collagen crosslink at opposite temperatures yielding hydrogel stability and reproducibility issues. Thus, to increase the cell viability and biological relevance, Matrigel was added to the GelMA hydrogel solution. Matrigel is broadly employed for the in vitro mimicking of the complex ECM of BC and consists of a soluble and sterile extract of basement membrane proteins secreted by Engelbreth-Holm-Swarm (EHS) mouse sarcoma cells. It contains undefined and highly variable ECM factors that certainly affect the reproducibility of experimental readouts and the reproducibility of model [96]. On the other side, Matrigel contains critical growth factors and cytokines for cell growth-enhancing cellular events, allowing cells to express malignant features [97] [98] [99].

3.3.3 EXPERIMENTAL EMPLOYMENT OF 3D *IN VITRO* HYDROGEL-BASED BCM$^{(+)/(-)}$

Parallel to the characterization of the cell-free hydrogel made of GelMA and Matrigel, in which pore size distribution, dynamic mechanical analysis, and stability were assessed, also hydrogel biocompatibility was assessed by means of characterization at the microscopic level in terms of cell growth, viability, and morphology. In the latter case, 3D monocultures of NIH/3T3 fibroblasts and 4T1 cancer cells were separately seeded in the hydrogel-based scaffolds and evaluated. Once assessed the biological and mechanical validity of the cell laden GelMA/Matrigel hydrogels, further characterization at the molecular level was conducted in terms of both, relative desmoplastic reaction and of relative pro-tumorigenic features. In this case, 3D hydrogels made of 3T3 and 4T1 cancer spheroids (collected on day 3) in ratio 5:1 were submitted to dynamic mechanical analysis (DMA), on days 0,5, and 10, and gene expression by quantitative polymerase chain reaction (qPCR) on day 4 respectively. The whole triculture system was assembled for further characterizations and applications. In particular, subsequent to BC spheroid seeding (till day 3), these were integrated into the 3D hydrogel solution with or without 3T3 fibroblasts cell line. In both cases, the channel was endothelialized with an endothelial H5V cell line. Besides the cell-free hydrogel model, BCM without 3T3 (BCM $^{(-)}$) and with 3T3 (BCM $^{(+)}$) were employed according to the applications.

Microtissue morphology and relative pro-tumorigenic features were furtherly assessed via protein expression by immunohistochemical (IHC) staining. The resulting 3D in vitro model was kept in static culture for about 10 days in order to be ready for both, transport and MBs-US applications.

Three configurations of the model were used in this phase of applications to study molecules transport, namely cell-free model, BCM$^{(-)}$ composed of endothelial H5v cells and 4T1 breast cancer spheroids for evaluation on the endothelial barrier, and BCM$^{(+)}$ which differed from the previous one upon addition of 3T3 to confer to the model a dense stroma. After recapitulating a microenvironment that owns both endothelial and stromal barriers, we wanted to assess the effective functionalization of the BCM models and their suitability as a tool for molecules transport studies. In order to do so, the diffusion profiles of Rhodamine B (ca.1 nm) and FITC Dextran 10 kDa (ca. 4-5 nm) within the three tissue conditions were estimated. As diffusion rate, we considered the diffusion distance of the tracers from the channel wall over time (10 min). FITC Dextran 70 kDa (ca. 10 nm) and silica NPs (100 nm) with a net lower diffusion rate were characterized just in the case BCM $^{(+)}$ for a more complete data set in the case of stroma samples. In acoustical setups, cell-free hydrogel and BCM$^{(-)}$ were employed to investigate the enhanced transport through the walls of both, cell-free hydrogel and endothelialized channels.

3.4 BCM MODEL DESIGN

During the design and optimization phases, we addressed challenges relative to the composition of a biocompatible, stable, relevantly sized, and perfusable hydrogel matrix. These requirements had to match with the development of an optically and acoustically clear chamber which allowed both the photocrosslinking of the thick GelMA/Matrigel hydrogel and avoided the US beam distortion and interference while ensuring ease for perfusion set-up. Furthermore, the general requirements followed to develop the model were the high reproducibility, the control over cultivation conditions, the incorporation of multiple cell lines, and the eligibility to be used in dynamic conditions (perfusion) in two different microscopic set-ups (acoustical and biological).

In detail, the BCM model was based on a GelMA/Matrigel perfusable triculture scaffold into a containing mould customized with inlet and outlet needles. The whole model thus was designed to host and perfuse the in vivo-like environment with a significant cellular density and appropriate volume.
Practical challenges were mostly related to channel integrity (structural stability), to the success of endothelization, to the firm installation of perfusion needles within the cured hydrogel, and to the design of acrylic holder able to allow hydrogel photocrosslinking and thus its stability.

a. Choice of hydrogel:

The guidelines followed in the hydrogel composition study were mostly based on the requirements of cell viability, transparency, and structural stability as reported in the previous section .

b. Choice of mould:

When a US wave propagates through mediums with a different impediment a loss of the transmitted signal and echo generation due to partial reflection might occur. Notably, albeit the broad employment of polydimethylsiloxane (PDMS) as an acoustical chamber of microfluidic devices used for US applications, it does not yield the optimal US transmission as it does not properly match the impediment between the water and the viscoelastic hydrogel matrix and, in fact, it is characterized by high α (usually >2 dB/cm) [90 93 100].

For the same unmatched impediments reason, for the final configuration of the BCM model also sharp needles and glass slides were avoided. Therefore, the final BCM model a transparent square-shaped plastic mould (15x15x5mm) was used as main microtissue holder. The mould was customized with blunt inlet and outlet needles and, eventually in case of sonoporation, punched to avoid interferences of the plastic mould bottom with the US beam. Due to the significant size of the samples (10x10x5 mm), the hydrogel was compartmentalized in two or three adjacent parts according to the final application and microscope setting. The several model design which presented limitations are reported in Supplementary material, Fig.5S.

c. BCM MODEL ASSEMBLY

According to the different microscopy configurations of the biological and acoustical experimental set-ups, the BCM hydrogel was assembled to have the channel sharper as possible. Thus, in case of molecules transport (observed with inverted microscope) the channel was close to the bottom of the microtissue, while in the MBs-US set-up the channel was located as close to the top as possible (observed with an upright microscope). The layering-based assembly of the BCM used in applications is shown below (Fig.7):

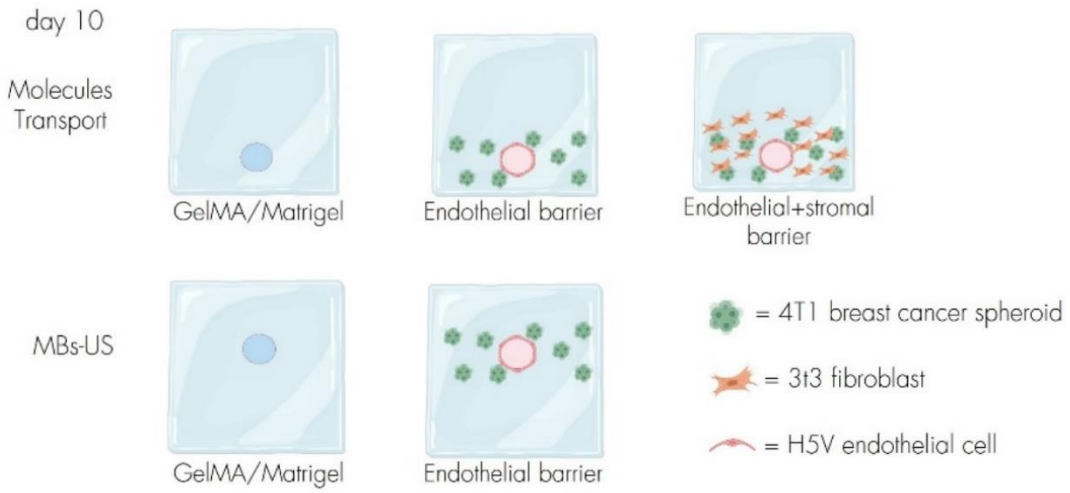

FIG. 7 SCHEME BCM EMPLOYMENT IN THE APPLICATIONS On day 10, cell-laden hydrogel, with or without 3T3 BCMs were used for studying the transport of molecules with different size, while in MBs-US applications only cell-free hydrogel and endothelialized hydrogel (without 3T3) were used

d. Choice of perfusion fluid:

The dynamic of MBs, and in particular the pressure threshold for inertial cavitation regime, is also affected by the viscosity of the medium in which they flow, for this reason, in this model setup, MBs and fluorescent dyes were administered in a BMF solution to better mimic the blood viscosity. Medium viscosity and flow velocity, in turn, vary with the channel size (200 μm) [101]. Perfusion was possible by means of tubes connected to a syringe pump in infusion mode following withdrawal on the outlet side with a syringe to facilitate to further address the flow within the channel.

4. MATERIALS AND METHODS

Chemicals and Materials

NIH/3T3 fibroblast and Mouse 4T1 breast cancer cells were obtained from American Type Culture Collection (ATCC, Rockville, MD). 100 nm plain Silica NPs were obtained from Sicastar-redF. Antibodies used were obtained from companies as listed in Table 2 (Appendix). Secondary and tertiary antibodies were obtained from Dako Denmark (Agilent Technologies, Santa Clara, CA, USA). Fluorescent secondary antibodies were obtained from Thermofisher Scientific (Waltham, MA, USA) or Invitrogen (Carlsbad, CA, USA). RPMI-1640 without glutamine and Dulbecco's Modified Eagle Medium (DMEM) 4.5 g/l with L-glutamine was purchased from PAA/GE healthcare (Eindhoven, The Netherlands). Haematoxylin, Penicillin/Streptomycin (Pen/Strep), and β-mercaptoethanol were purchased from Sigma Aldrich (Zwijndrecht, The Netherlands). Dulbecco's Phosphate-Buffered Saline (DPBS) was purchased from Lonza Benelux BV (Breda, The Netherlands). Fetal bovine serum (FBS) and Trypsin-EDTA 0.5% were purchased from Life Technologies (Blieswijk, The Netherlands).

4.1 HYDROGEL PREPARATION AND CHARACTERIZATION

4.1.1 GelMA synthesis

Gelatin methacryloyl (GelMA) was synthesized according to previously published protocols at a high degree of methacryloyl substitution (~75%) [102]. In brief, 10% w/v gelatin was dissolved Dulbecco's phosphate buffered saline
(DPBS, Lonza) at 50 °C until a homogenous solution was obtained. Then 8% v/v of methacrylic anhydride were added to the solution drop-wisely. The solution was allowed to react for 2 h under constant stirring before the reaction was stopped by adding MilliQ water. Then the GelMA solution was dialyzed against MilliQ water with a 12-14 kDa dialysis tubing at 40°C for 1 week to remove salts and methacrylic acid. The GelMA solution was then lyophilized and stored at -20°C until further use.

4.1.2. GelMA and Matrigel Hydrogel Preparation

Photoinitiator (PI) 2-Hydroxy-4′-(2-hydroxyethoxy)-2-methylpropiophenone namely Irgacure 2959 (Sigma Aldrich) was dissolved at a concentration of 0.3% w/v in DPBS at 80°C for 10 min. Lyophilized GelMA pre-polymer was fully dissolved at working concentration 4% w/v in PI solution, mixed on vortex, and warmed at 37°C for complete dissolution wrapped in aluminium foil. The 4% GelMA 0.3% PI warm solution was sterilized through 0.2 µm syringe membrane filters (Corning® syringe filters) and 1 % v/v Penicillin/Streptomycin (Pen/Strep, Lonza) was added to minimize the risk of contamination. To incite biological signaling 5% v/v Matrigel was stored in ice till use was added to the GelMA solution, gently

mixed to avoid bubbles, and protected from visible light. The final hydrogel solution made of 4% w/v GelMA (0.3% w/v PI) and 5% v/v Matrigel was stored at 4°C under dark conditions until experiments. The hydrogel was then poured in disposable base plastic moulds 15x15x5mm (Polysciences, Inc., Warrington, PA) personalized with aligned inlet and outlet blunt needles 27 G through which 200 µm nylon fishing line (DLT Predator, Nylon Vislijn, 0.20mm, 500m, The Netherlands) was inserted to form the negative of the channel. Once that the GelMA/Matrigel solution was poured, the hydrogel was left 10 min at 4°C for a first thermal crosslink. The mold with gelatinous hydrogel was then photopolymerized by exposure to UV light (λ 365nm, NailStar NS-01, NailStar Professional, London, UK) at 12 mW/cm^{-2} and 5 cm distance for either 2 min. Once that the hydrogel was cured, the fishing line was removed, and the channel was formed.

4.1.3 Hydrogel Characterization

Crosslinking stability

GelMA Matrigel hydrogels were prepared and placed at 37°C. To measure the loss in volume due to water release at 37°C and thus the hydrogel crosslink stability, pictures of the hydrogel were taken at 0, 15, 30,45, 60,120,180, 300 minutes. Pictures were then analysed in ImageJ and the size and thickness measured. All the data measurements were then standardized min 0.

Scanning Electron Microscopy (SEM)

GelMA/Matrigel hydrogels were prepared as written above. The hydrogels were washed twice with DPBS and fixated with 4% formaldehyde solution for 40 minutes and washed twice again with DPBS. After fixation, samples were stored at 4°C in DPBS. The samples were then placed in a falcon tube with enough DPBS to cover them and they were frozen into the liquid nitrogen and lyophilized for 2 days. Samples were broken apart with tweezers and placed on SEM stubs. They were coated with a conductive coating by gold sputtering (Sputter Coater 108 Auto, Cressington Scientific Instruments, Watford, UK) and imaged with the Scanning Electron Microscopy (JSM-IT100, JEOL, Tokyo, Japan). Pore size was analysed with ImageJ.

Mechanical properties

GelMA/Matrigel hydrogels were prepared as above mentioned. For assessing the mechanical properties, samples were submitted to Dynamic Mechanical Analyzer (DMA 850, TA, New Castle, DE). All the measurements were in compression mode and performed at 20 °C, with an initial/preload force of $9.80655x10^{-5}$ N. Stress-strain curves were visualized on TRIOS software (v5.3, https://www.tainstruments.com/trios-software/).

4.1.4 Cell culture

Mouse 4T1 breast cancer cells were cultured in Roswell Park Memorial Institute (RPMI) 1640 medium (PAA/GE Healthcare, Eindhoven, The Netherlands) supplemented with 2 mM L-glutamine,10% fetal bovine serum (FBS) and antibiotics (50 U/ml Penicillin and 50 ng/ml streptomycin. Mouse NIH/3T3 fibroblasts and mouse H5V endothelial cells were cultured in Dulbecco's modified Eagle's medium (DMEM) (PAA/GE

Healthcare, Eindhoven, The Netherlands) supplemented with 2 mM L-glutamine, 10% FBS and antibiotics (50 U/ml Penicillin and 50 µg/ml streptomycin). All cells were grown in cell culture treated 75 cm^2 flasks in a humidified incubator at 37 °C with 5% CO_2. Cells were passaged every 3 days and 0.05% trypsin-EDTA in PBS was used for cell detachment.

Cell Viability

To determine the viability of cells after seeding and thus the biocompatibility of the fabrication process, green fluorescent Calcein-AM/red fluorescent ethidium homodimer-1(EthD-1) staining on hydrogels. In brief, hydrogels containing monocultures of both NIH/3T3 fibroblasts and 4T1 cancer cells were prepared and immediately, after cell seeding within the hydrogels, each sample was cut in four parts and measured on days 1,4,7,10.
Each sample was washed twice with DBPS before incubated with 1 µl/mL Calcein-AM to stain alive cells and 2 µl/mL EthD-1 to stain dead cells for 20 min at 37°C and immediately imaged with fluorescence microscopy (EVOS Cell Imaging System, Thermofisher Scientific). Quantification was performed by counting alive and dead cells using ImageJ (Wayne Rasband, NIH, MD).

Cell Metabolic Activity

Similar to cell viability, the metabolic activity of cells was measured 1, 4, 7 and 10 days after cell seeding. To monitor the activity, 15 µL of Alamar Blue dye (Sigma-Aldrich) in 150 µL of culture medium was added per well. After 4h, the fluorescent signal was measured using a VIKTOR™ plate reader (Perkin Elmer, Waltham, Massachusetts).

Spheroid formation

Wells of a non-adherent, round-bottom 96-well plate were treated with 100 µl of a protein repellent coating consisting of 1% (w/v) Pluronic®F-127 (BASF, USA) prior to experiments to prevent cell attachment during spheroid culture. Pluronic solution was added to each well, incubated overnight at 37°C, and washed out twice with sterile MilliQ water before cell seeding. Mouse 4T1 breast cancer cells were seeded with a cellular density of 6000 cells/well and cultured undisturbed for 3 days at 37 °C with 5% CO_2 to form homospheroids.

4.2 BCM Assembly and Characterization

Preparation for studying physical barriers effect on molecules transport

GelMA/Matrigel solution was prepared as described above while the BC microtissue assembly is schematized below.
The effect of physical barriers as endothelium and stroma was evaluated by assembling three different types of models:

i) cell-free model;

ii) ii) stroma-free microtissue model [H5V+, 4T1+, 3T3-] to investigate the effect of endothelial layer;

iii) iii) BC microtissue model [H5V+, 4T1+, NIH/3T3+] in which, besides the endothelial layer, also the effect of stromal components such as high cellular density fibroblasts was evaluated.

For cell-free hydrogel the preparation procedure is the same described above (Supplementary Materials, Fig.6S). For the cellular models, a first layer of hydrogel solution with or without $4x10^6$ cells/ml NIH/3T3 was deposited in the plastic mould and cooled down for a first thermal crosslink at 4°C for 10 min. Approximately n=40 4T1 spheroids per sample were harvested on day3, collected in falcon tube, centrifuged, and mixed with the solution of hydrogel with or without ($4x10^6$ cells/ml) NIH/3T3. This second layer of hydrogel containing 4T1 spheroids and NIH/3T3± was poured on top of the first solidified hydrogel layer and again placed at 4°C for 10 min. The thermal crosslink at 4°C has a double function as it ensures the deposition of cancer spheroids roughly at the same level of the channel avoiding their precipitation on the mould bottom due to gravity and increases the photocrosslinking stability of the whole assembled hydrogel. Upon solidification, the cellularized hydrogels were photopolymerized by exposure to UV light (λ 365nm, NailStar NS-01, NailStar Professional, London, UK) at 12 mW/cm^{-2} and 5 cm distance for 2 min (Fig.).

Channel endothelialization: Following the photocrosslinking of the microtissue, the channel was coated with a solution of 100 µl of Matrigel in 1 mL of cold DPBS and left at room temperature for 1 h prior to endothelialization to improve cellular adhesion. The microfluidic device was endothelialized by injecting in the inlet and outlet needles 25 µl of 10 x 10^6 cells/ml H5V suspension in DMEM medium. Both inlet and outlet needles were closed with sealed 30 G needles to facilitate the entrance of cells into the channel. The microtissues were then incubated for 30 minutes at 37°C. Right after, the same injection process was repeated, and the needles were closed again and incubated overnight immersed in cell culture medium made of DMEM/RPMI-1640 at 50:50 ratio. After 24 h the 30 G needles were removed allowing the external medium to passively flow into the channel. The formation of a confluent monolayer took ca. 3 days (Fig.8).

BCM were cultivated in petri dishes immersed in DMEM/RPMI-1640 at 50:50 ratio for 7 days at 37 °C with 5% CO_2. Cell culture medium was changed and refreshed once per day for 7 days. BCM were monitored with bright field microscopy (EVOS Cell Imaging System, Thermofisher Scientific).

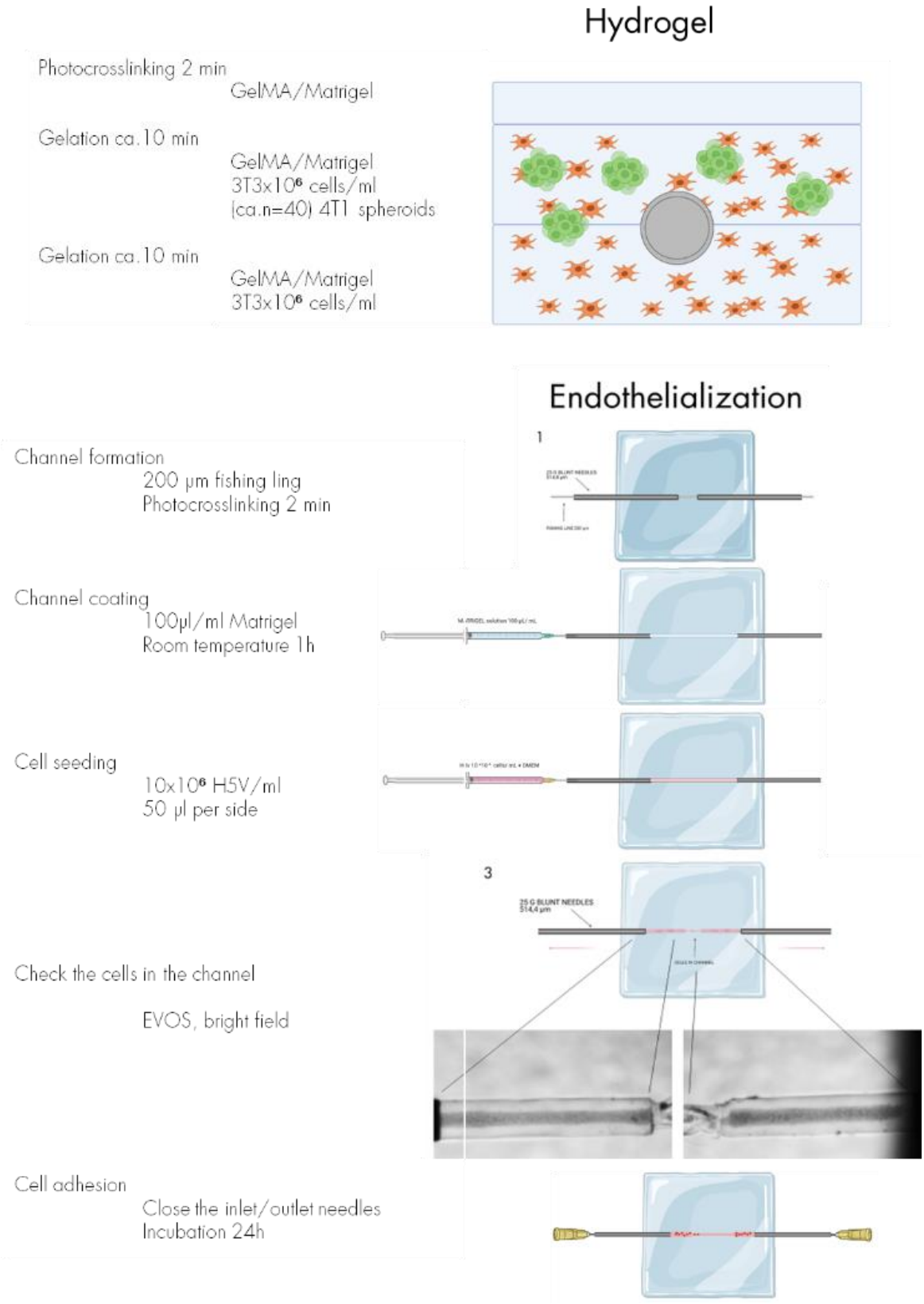

FIG. 8 SCHEMATIC REPRESENTATION OF BCM LAYERING-BASED PREPARATION AND ENDOTHELIALIZATION PROTOCOLS

CellTracker™ Labelling

Previously cultivated cells were labelled with CellTracker™ (Green CMFDA Dye, Red CMTPX Dye; Molecular Probes) according to manufacturer's protocol. Briefly, 4T1 spheroids and H5V cells were harvested, centrifuged, and resuspended in a solution of 1 µL of CellTracker™ dye in 1mL of fresh medium every million cells and incubated for 40 min at 37°C. In NIH/3T3 – hydrogels, 4T1 spheroids were stained in red and H5V endothelial cells in green [Fig.] In NIH/3T3 + hydrogels, 4T1 spheroids were stained in red and H5V endothelial cells in green while fibroblasts were not stained. Next, the CellTracker™ working solution was removed upon centrifugation and cells resuspended in fresh medium and further cultured. Picture were taken on day 1 of culture with fluorescence microscopy via 4x 10 x objective (EVOS Cell Imaging System, Thermofisher Scientific).

4.3 MODEL CHARACTERIZATION

i) Acoustical characterization: cell-free and cell-laden NIH/3T3^{+} (4*10^{6} cells/ml) GelMA/Matrigel hydrogels (15x15x5mm) were used to assess the acoustical clarity of the model;
Optical characterization: cell-free and BCM $^{(-)/(+)}$ were used to assess the optical clarity of the model under acoustical set-up;

ii) Biological characterization: NIH/3T3 and 4T1 monocultures were separately seeded to compare the differences in gene expression of the two cell lines in 2D monolayers and 3D hydrogel environments (Supplemtary Materials, Fig.);

iii) Biological characterization: BCM $^{(+)}$ (H5V $^{(-)}$) models in which just 3T3 and 4T1 cells were seeded in 7x7x5 mm hydrogels as 3D monocultures and then as 3D co-culture were used to assess the tumorigenicity of the model in the 3D environment with pathophysiological ratio 5:1, NIH/3T3:4T1;

iv) Mechanical characterization: Co-culture 3D samples (NIH/3T3^{+}; 4T1^{+}; H5V $^{-}$) were used to assess the mechanical properties of the cell-laden hydrogel and a potential increase in model stiffness over a 10-days period;

v) Biological characterization: BCM$^{(+)}$ were sectioned and stained via immunohistochemical staining to observe morphology and protein expression over time (on day 7 and day 14).

4.3.1 Optical and acoustical characterization

Samples for optical and acoustical characterization in the US set-up were realized as described above, with and without (4x10^{6} cells/ml) NIH/3T3 fibroblasts. In order to assess the hydrogel acoustical transparency, acoustical characterization has been performed (the set-ups are shown in Fig.9). The measurement was performed using two focused single-element transducers, mounted in a water bath, see the below figure. The transmit transducer (V304 SU, Olympus) had a center frequency of 2.25 MHz and a focal distance of 4.77 cm. The receive transducer (V307-SU, Olympus) had a center frequency of 5 MHz and a focal distance of 4.90 cm. Pulses were produced with a programmable waveform generator

(8026, Tabor Electronics Ltd., Tel Hanan, Israel). The amplitude was adjusted and amplified by a power amplifier (VBA 100-200, Vectawave). Received signals were recorded on a digital oscilloscope.

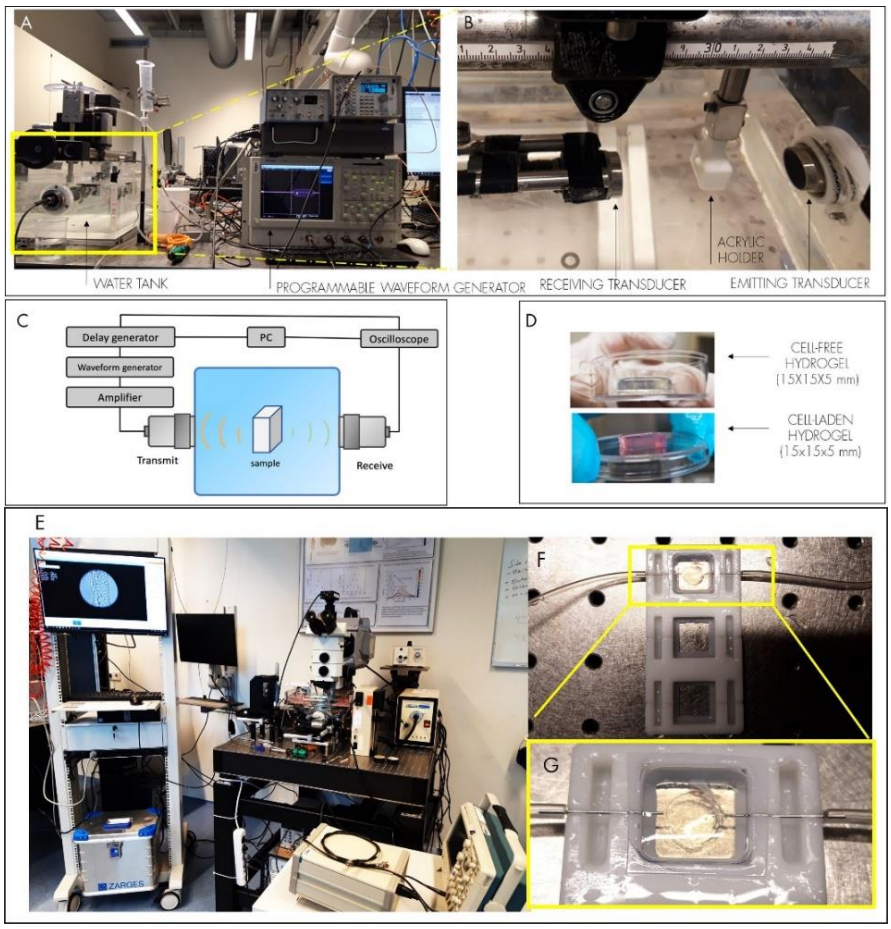

FIG. 9 EXPERIMENTAL SETUPS OF ACOUSTICAL AND OPTICAL CHARACTERIZATIONS. A) Overview of the acoustical characterization experimental setup; B) Water tank containing emitting and receiving transducers and the acrylic holder for the samples with and without cells (shown in D); C) Schematic representation of the acoustical setup; E) Optical and MBs-US setup with ultra-high-speed-camera; F) G) Cell-free hydrogel model (complete with disposable mould and needles) inserted in the acrylic holder for keeping the sample in the water tank during experimets.

4.3.2 Biological characterization

4.3.2.1 Tissue morphology

Haematoxylin and eosin (H&E) staining were performed for a histopathological tumor representation of BC microtissues with NIH/3T3, H5V, and 4T1 cancer spheroids at day 7. Before and after tissue fixation with 4% paraformaldehyde BC microtissue were properly rinsed (x 2 times) in 1xPBS. The fixed samples were subject to sucrose treatment which, as a cryoprotectant, disrupts interactions between polar water molecules preventing ice crystal formation in tissues when water freezes and expands. BC microtissues were treated with 5%,10%, 20% sucrose (Sigma Aldrich) in demi water for 1 h each and then 30% sucrose in demi water overnight at 4°C. For sectioning BC microtissues were collected, embedded in Cryomatrix (Thermo Scientific), and frozen at – 80°C. Afterward, BC microtissues were cut into 10 mm thick sections using a Cryotome FSE (Thermo Scientific). The BC microtissue slices were collected on microscope slides and air-dried for 30 minutes. Samples were fixed with 4% formaldehyde for 15 min and washed 3 times x 2 min in aqua dest. BC microtissue slices were then incubated for 15 min in haematoxylin solution and rinsed under tap water for 15

minutes. After washing, slides were incubated for 1.5 min in eosin-solution. Following a series of ethanol-based dehydration steps, respectively (2x) 96% and (2x) 100% ethanol for 1 min each, the sections were sealed with cover slip by adding Depex mounting medium and left overnight at 4°C.

4.3.2.2 Tumorigenicity

a. Immunohistochemical staining of microtissue

Tumorigenicity trends of the BC microtissues with NIH/3T3, H5V, and 4T1 cancer spheroids were observed with immunohistochemistry (IHC) staining at day 7 and day14. Before and after tissue fixation with 4% paraformaldehyde BC microtissue were properly rinsed (x 2 times) in 1xPBS. The fixed samples were subject to sucrose treatment which, as a cryoprotectant, disrupts interactions between polar water molecules preventing ice crystal formation in tissues when water freezes and expands. BC microtissues were treated with 5%,10%, 20% sucrose (Sigma Aldrich) in demi water for 1 h each and then 30% sucrose in demi water overnight at 4°C. For sectioning BC microtissues were collected, embedded in Cryomatrix (Thermo Scientific) and frozen at – 80°C. Afterwards, BC microtissues were cut into 10 mm thick sections using a Cryotome FSE (Thermo Scientific). The BC microtissue slices were collected on microscope slides and air-dried for 20 minutes. Samples were fixed with aceton (Sigma Aldrich) for 10 min and air dried again. The edges of the slides were marked with a hydrophobic Pap-pen (Life Technologies). BC microtissue were rinsed three times in PBS (5 minutes each) before primary antibody incubation overnight at 4°C.
The next day, the slides were washed 3 times with PBS and in order to avoid nonspecific staining of the tissue and unwanted background staining that falsely indicates the presence of an antigen, slides were treated with endogenous peroxidase blocking via 125 µl of 30% hydrogen peroxidase (H_2O_2) in 50 ml PBS for 30 min. Again, BC microtissue were rinsed three times in PBS (5 minutes each) before secondary antibody (dilution 1:100) incubation for 1 h at room temperature. Samples were rinsed per 3 times (5 min each) in PBS before the tertiary antibody (dilution 1:100) incubation for 2 h at room temperature. Samples were rinsed per 3 times (5 min each). Next, 3-amino-9-ethylcarbazole (AEC) staining kit (Sigma Aldrich) was used to stain section. Sample were rinsed in aqua dest before counterstaining the section with haematoxyline for 1 min. The samples were then left under tap water flow for 5 min and covered with a coverglass using Aquatex.
Sections have been imaged using a Hamamatsu NanoZoomer Digital slide scanner 2.0HT (Hamamatsu Photonics, Bridgewater NJ).

b. Relative gene expression in BC microtissue

Cell-laden hydrogel with NIH/3T3 and 4T1 cancer spheroids 3Dmonocultures and co-cultures (ratio 5:1) were mixed with hydrogel solution and photocrosslinked in plastic molds (7x7x5 mm). After 4 days of culture each hydrogel was degraded with 1.5 mg of collagenase (Sigma-Aldrich). The hydrogels were incubated at 37 °C till the complete hydrogel degradation was reached (approximately 1,5 h). Afterwards, the cell suspension was centrifuged (300 g for 5 min) and the supernatant was removed. The cells were then lysed
using RNA lysis buffer supplemented with mercaptoethanol (10 µl/1 mL lysis buffer). The RNA was isolated using standard protocols provided by the manufacturers (RNA Kit, Sigma-Aldrich). The purity and RNA concentration of the samples were determined using NanoDrop (Nanodrop ND-1000, Wilmington, DE, USA) with a sample size of 2 µl. cDNA was synthesized using standard protocols and products (Bio-Rad Laboratories B.V., Hercules, California, USA). The synthesis was performed using Arktik Cycler (Thermofisher Scientific) with pre-designed protocols, provided by the

manufacturers. The qPCR was performed as follows. The prepared cDNA was diluted using RNAse free water to a final concentration of 5 ng/ mL. For each gene measured, a primer master mix was prepared consisting of respectively 0.08 mL forward primer, 0.08 mL backward primer (both at conc. of 15 mM), 4 mL SYBR Sensimix (Bioline Reagents, London, UK) and 1.84 mL RNAse-free water, adding up to a final volume of 6 mL for each well. Respectively 2 mL cDNA and the primer master mix were added in one well. Afterwards the plate was sealed and centrifuged for 2 min before starting the qPCR conform standard protocols (C1000 thermal cycler Bio-Rad, CFX 384 RT system). The housekeeping gene Glyceraldehyde-3-phosphate (GAPDH) was used for data normalization and for determination of relative gene expression values. The fold induction values were calculated from the Cq values using the $2^{-\Delta\Delta Ct}$ methods.

.

c. Transcriptome expression analysis in the human cohort from the public database

We selected and downloaded human TNBC gene expression datasets from the Expression Omnibus database (GEO). *GSE65194 dataset comprises of 41 TNBC tissues versus 11 normal breast tissues serving as control [103]. We used GEO2R to assess the expression of different mRNA expression in TNBC versus control samples and plotted the normalized gene expression levels

4.3.3 Mechanical characterization

To evaluate the stiffening of BC microtissue over time, H5V - samples were harvested and fixed in 4% Paraformaldehyde at days 0, 5, and 10. In particular, NIH/3T3 cells and 4T1 spheroids (day 3) were seeded into the hydrogel as described above. For assessing the mechanical properties, samples were submitted to Dynamic Mechanical Analyzer (DMA 850, TA, New Castle, DE). All the measurements were in compression mode and performed at 20 °C, with an initial/preload force of 9.80655×10^{-5} N. Stress-strain curves were visualized on TRIOS software (v5.3, https://www.tainstruments.com/trios-software/).

4.4 Effect of physical barriers on molecules transport within the BCM

To investigate the transport of molecules with different molecular weight through the endothelium and into the surrounding extravascular stromal matrix, the three models, respectively cell-free, NIH/3T3 -, and NIH/3T3 +, were connected by means of tubes (Masterflex Transfer Tubing, Tygon® ND-100-80 Microbore, 0.020" ID x 0.060" OD) to the perfusion system. In particular, the inlet needles were connected via tubing to a 1 ml syringe located on the syringe infusion pump (KDS 200 / 200P legacy syringe pump) while the outlets were connected via tubing to a 1 ml syringe hand controlled. Blood mimicking fluid solution (BMF) composed of glycerol (MW 92.094, 99.5%; Thermo Fisher Scientific, Waltham, MA, USA) and PBS (Gibco, Sigma-Aldrich the Netherlands) was filtered with 0.2 µm syringe membrane filter and used as circulating fluid in a ratio of 55:45 wt% to match physical properties of blood [104]. Stock solution of Rhodamine B (Sigma Aldrich) and of fluorescein isothiocyanate-dextran (FITC-dextran) 10kDa and 70 kDa (Invitrogen™) were prepared by dissolving 50mg/ml of dye powders in MilliQ water and later in BMF with final concentrations of 200 µg/ml. While 50 mg/ml of 100 nm plain Silica NPs (Sicastar-redF) were added to BMF at a concentration of 500 µg/ml. The perfusion rate was set at 10 µl/min while the outlet syringe was used to create a sort of suck withdrawal within the channel and address the flow. Bright field images and fluorescence microscopy time lapses (time range = 600 s and interval 10 s) were token with

4x objective (EVOS Cell Imaging System, Thermofisher Scientific). To evaluate the dyes diffusion rate, pictures at t=0,60,300,600 s were overlapped and modified with the bright field picture on Inkscape, while measurements were done with ImageJ. To further confirm the different diffusion rates, signal intensity profile was also analysed via ImajeJ.

4.5 US APPLICATION

4.5.1 BCM Preparation for MBs-US application

The preparation protocol of BCM for acoustical applications is similar to the previous described with a few differences. First, the bottom of the plastic mould 15x15x5 mm was punched with 8 mm disposable biopsy puncher (Acu-Punch, Acuderm Inc, Lauderdale, USA) to avoid the plastic to interfere with the UV beam. To allow the crosslink of the hydrogel within the mould the punched part was then attached to the bottom with transparent tape and completely removed right after the crosslink. Second, the volume of solution is higher as the channel was supposed to be closer to the top surface rather than the bottom surface as in the previous case. The disposable mould was then filled completely with three layers instead of two, of which the last one was cell-free hydrogel layer to ensure a relative transparency of the channel in the presence of NIH/3T3. For US-mediated enhanced molecules diffusion study, cell-free and NIH/3T3- hydrogels were used to investigate the effect of MBUS on the endothelium and, eventually, the enhanced molecules extravasation and diffusion.

4.5.2 High-speed imaging setup

By means of ultra-high-speed camera it was possible to observe mutual interactions which are established among cavitating MBs within the channel as well as the influence of (endothelialized or cell-free) vessel walls in MBs dynamic. In general, the high-speed videos reveal how the cavitating bubbles can increase the permeability of vessel walls yielding insights crucial for a better understanding of underlying sonoporation mechanisms. Depending on different applications the speed of recording may vary. Studying the bubble dynamics is possible at recording speed of at least 2 million frames/second since the microbubbles cavitate at millions of Hertz. Since we were interested in observing the interaction of bubbles with the vessel walls the videos are recorded in hundreds of thousand frames per second (the exact frame rate is mentioned at the caption of each figure).
The setup includes an Olympus-BX2 microscope with a 5x objective (Fig.10). The bubble and vessel wall were recorded using Photron SA-Z high-speed camera. The samples were illuminated with Sumita LS-M352 at the maximum power to support the needed light for the high-speed imaging. The ultrasound waves were produced using Tabor 8026 waveform generator and amplified with amplifier (gain of 51dB). The amplified electronic signal was transformed into pressure waves using a focused ultrasound transducer with the centre frequency of 2.25 MHz (C305, Panametrics, USA). The alignment of optical and acoustical focal points was adjusted using a 200 μm needle hydrophone.

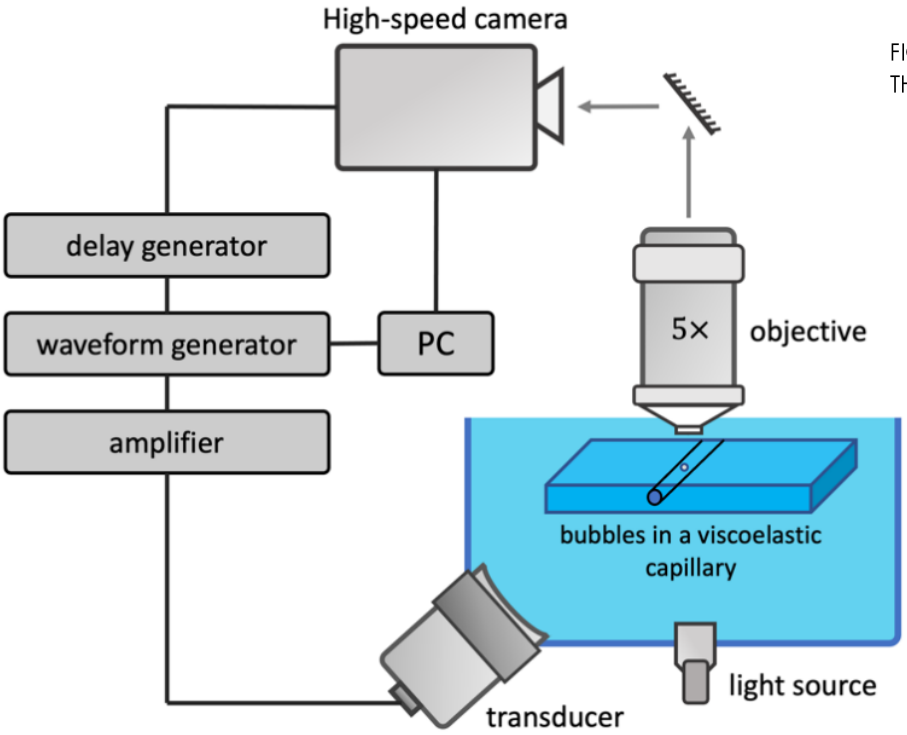

FIG. 10 SCHEMATIC OVERVIEW OF THE HIGH-SPEED-CAMERA SET UP

4.5.3 Fluorescent imaging Setup:

The FITC-Dextran 10 kDa has been used as fluorescent material to observe the diffusion in the surrounding matrix. The illumination of dye was performed using Olympus TH4 Halogen Lamp and a proper filter cube. Since we are interested to observe the propagation of dye in a long time and due to the low intensity of fluorescent dye the videos are recorded with 1.9 frames/s with the exposure time of 260 ms using Lumenera LM165M camera. The perfusion rate was set at 10 µl/min while the outlet syringe was used to create a sort of suck withdrawal within the channel and address the flow.

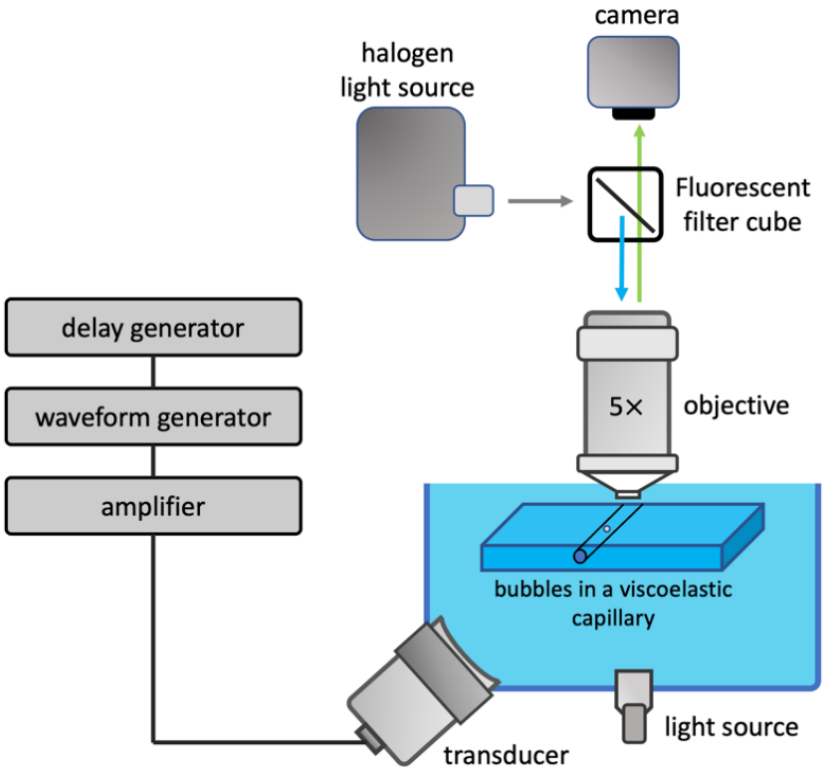

FIG. 11 FLOURECENT SETUP FOR QUANTIFYING THE EFFECT OF CAVITATION ON DRUG DELIVERY

4.5.4 Ultrasound pressure wave parameters:

Pressure:

According to the information in literature the drug delivery is more efficient when the bubbles are cavitating in the inertial cavitation regime [105] [106]. At inertial cavitation MBs oscillate significantly inducing shear stresses on the surrounding medium including the capillary walls. This is the mechanical effect behind the increased permeability and drug delivery mediated by MBs-US. The pressure that we have used in these experiments was 700 kPa, according to therapeutic sonoporation parameters found in literature [90]. By means of ultra-high-speed camera we could observe MBs in an inertial regime of oscillation upon exposure to this pressure.

Frequency:

The frequency at which the bubbles were insonified is based on the resonance frequency of bubbles. The resonance frequency is the frequency at which the bubble has the biggest oscillation. This frequency can be calculated using Meneart relation:

$$f_0 = \frac{1}{2\pi R_0}\sqrt{\frac{3\kappa P_0}{\rho}}$$

In this equation R_0 is the radius of bubble at rest, ρ is the density of liquid, κ is the polytropic exponent of gas inside the bubble and P_0 is the pressure inside the bubble. As it can be seen in Fig. 12 the resonance frequency strongly depends on the radius of bubble. This frequency is calculated based on the size of bubbles each time before performing the experiment. For example, for a case with $R_0 = 3\,\mu m$, $\kappa = 1.07$, $P_0 = 100\,kPa$, $\rho = 1000\ kg/m^3$ the resonance frequency is 1 MHz. Since the bubbles are monodisperse all the bubbles that have been used for each experiment have the same size therefore the same resonance frequency. In this context it is worthwhile mentioning the size distribution of bubbles were investigate with a coulter counter. Results indicate an average diameter of 6 μm for a MBs concentration of 20x10⁶ MBs/ml.

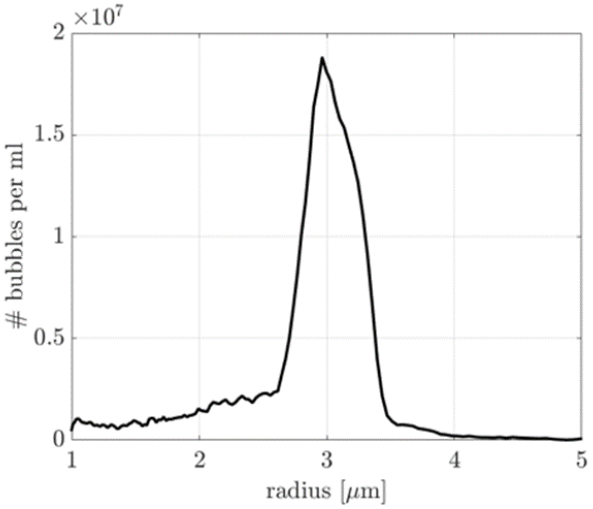

FIG. 12 CHARACTERIZATION OF A POPULATION OF THE EMPLOYED MONODISPERSE MBs (DENSITY 20X10⁶ MBs/ML) SHOW HOMOGENITY IN SIZE OF THE MBs WITH AN AVERAGE RADIUS OF 3 μm

Number of cycles and Pulse repetition rate

It has been shown in the literature that because of primary acoustical radiation force the bubbles can be pushed to the vessel walls. The cavitation in vicinity of bubble walls increase the permeability of vessel walls. The movement of bubbles is possible using long acoustical pulses. We have used 250 cycles for each burst of pressure waves. This applied pressure wave was repeated 4 times per minute.

Graphs & Statistical Analysis

All graphs were made using GraphPad Prism Vol.5 (GraphPad Software Inc., San Diego, CA) based on calculations using Microsoft Excel (Microsoft, Redmond, WA, USA). All values are expressed as mean ± standard error of the mean (SEM). Statistical significance of the results was performed by either two-tailed unpaired student's t-test for comparison between two treatment groups or two-way ANOVA for to compare multiple treatment groups. Statistical
significance between two patient groups in survival analysis was performed by Log-rank (Mantel-Cox) test. Significant difference was determined for a p-value of *p < 0.05, **p < 0.01 and ***p < 0.001, respectively.

5. RESULTS

5.1 GELMA/MATRIGEL HYDROGEL CHARACTERIZATION

5.1.1 GelMA/Matrigel hydrogel versatility and transparency

As shown in Fig. A-B-C, the 4% (w/v) GelMA + 5% (v/v) Matrigel hydrogel is very versatile as it can be employed to generate relatively thick (at least 5 mm) (Fig.13 A,C) or relatively large constructs (25x25x5 mm) (Fig.13 B) in a controllable fashion. In this research, hydrogels of 7x7x5 mm and15x15x5 mm were cured in 120 s via photo-crosslinking. While the small hydrogel size was used for samples aimed at mechanical and biological characterization, the larger size allowed us the model suitability for the different applications and set-ups, but also ease of perfusion and handling. Within the same hydrogel, it was possible to create multiple channels with different sizes, like 50, 100, and 200 μm as shown in Fig. D, as well as different patterns of channels, Fig. E-F. The formation of parallel and crossed channels in 15x15x5 mm hydrogels, as well as in 25x25x5 mm hydrogels, whether on the same plane and on different planes further shows the integrity and inner stability of the hydrogel constructs. However, the realization of thick (ca.5 mm) and large (> 15 mm) constructs resulted in a bit challenging because of insufficient photopolymerization factors. As reported above, in this case, the degree of methylation, GelMA and/or PI concentrations, or UV exposure time can be tuned to obtain more stable constructs at the expense, however, of cell viability. Important for this project is the transparency of the hydrogel which guarantees the optical clarity necessary for the observation of potential biological and acoustical phenomena.

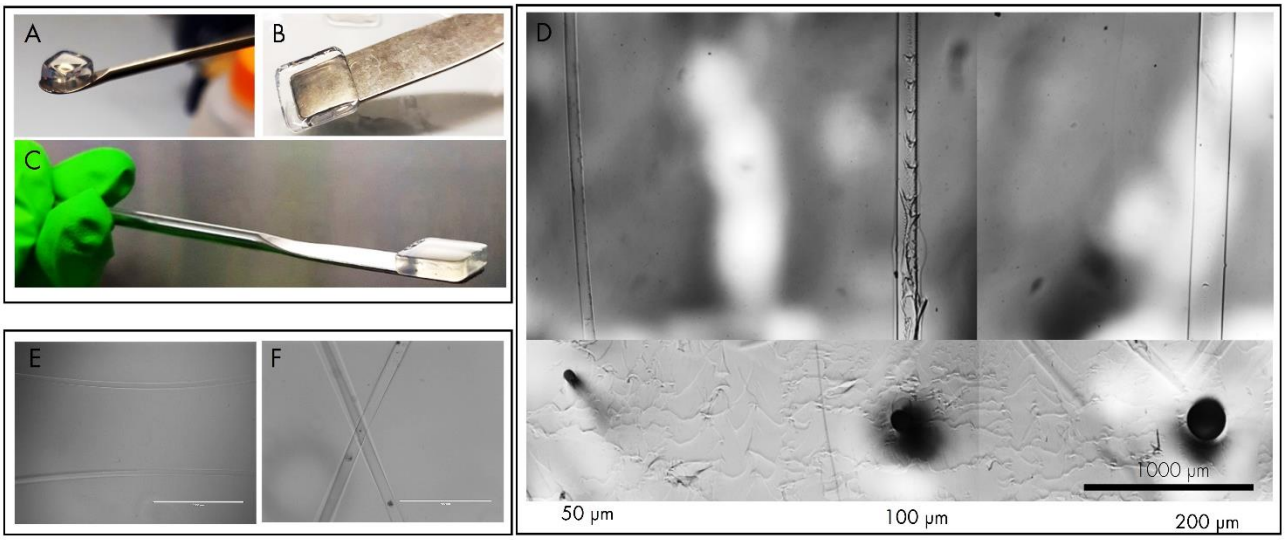

FIG. 13 CELL-FREE HYDROGEL INTEGRITY AND VERSATILITY IN SIZE (A,B,C), CHANNEL SIZE (D) AND CHANNEL PATTERNS (E,F) A) 7x7x5 mm hydrogel B) 25x25x5 mm hydrogel C) 15x15x5 mm hydrogel; D) Three channel sizes in the same hydrogel (15x15x5mm), left channel 50 µm, central channel100 µm, right channel 200 µm; The central channel resulted in slightly damaged by friction upon removal of the fishing line; bright field microscopy (4x) EVOS E) Parallel channels; bright field microscopy (4x) EVOS F) Crossed channels; bright field microscopy (10 x) EVOS

5.1.2 GelMA/Matrigel hydrogel stability and integrity

The stability of the hydrogel at physiological temperature (37°c) was assessed over a time range10 h, as shown in Fig. 14 F. Observation of the hydrogel allowed an approximate estimation of the loss of water of the hydrogel and thus of loss of volume. Upon incubation, the hydrogel size starts to decrease quickly and becomes stabilized after ca.90 mins for a total reduction by ca. 48.8% compared to the initial volume. Interestingly, despite the significant hydrogel dehydration, the channel integrity and stability were not compromised. Besides the storing temperature, as anticipated in the previous section and as shown in fig. A, also the initial size of the hydrogel affects the dehydration extent inasmuch, it affects the photocrosslinking resulting in a less stable in case of the large sample or very stable and thus minor dehydration, in case of the smaller sample, construct.

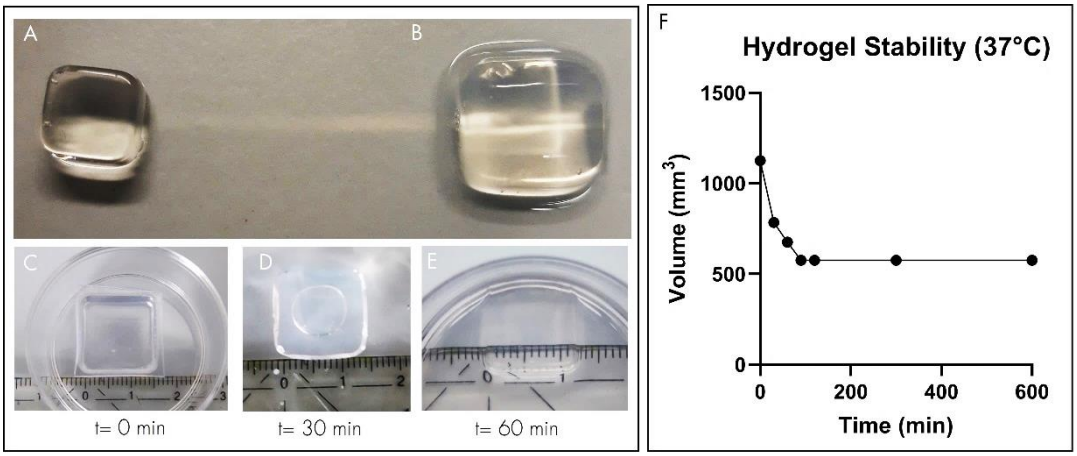

FIG. 14 HYDROGEL STABILITY AT ROOM TEMPERATURE AND AT 37°C A) cell phone picture of 7x7x5 mm hydrogel after 30 min at room temperature; B) cell phone picture of 15x15x5 mm hydrogel after 30 min at room temperature; C)D)E) cell phone pictures of 15x15x5 mm hydrogels after 0, 30, and 60 min at 37°C; E) Stability in terms of loss of water content and thus in terms of volume of a15x15x5 mm hydrogel over time

5.1.3 GelMA/Matrigel hydrogel morphology and pore size

The internal morphology of the 4% GelMA/5% Matrigel hydrogel was observed by Scanning Electron Microscopy (SEM). From the images obtained **(Fig.15),** GelMA/Matrigel hydrogels revealed a similar porous internal structure characterized by an irregular laminar organization. From the images and from the graph reported in **Supplementary material Fig. 3S**, it can be observed that sample n.1 shows a more homogeneous pore size distribution with a mean value of ca. 9,607 μm, while sample n.2 shows higher heterogeneous morphology and pore size distribution but still maintains the average pore size of 9,37. Sample n.3, shown in **Fig.**15 ,on the other hand, shows middle features of the first twos with a relatively homogeneous morphology and two main pore size means, ca. 9,654 μm. In general, we can assume that the GelMA/hydrogel hydrogel shows a relatively homogeneous network with non-interconnected pores which present an average diameter of 9,544 ± 0.0876 μm. It should be considered, however, that cell-free hydrogels were freeze dried prior to SEM measurements. Lyophilization has an impact on the structure of the sample, yielding cell-free hydrogels were lyophilized prior to SEM measurements. Pore size is well known to affect cell viability and affinity as it affects nutrient and oxygen diffusion. However, in case of fibroblasts, it was observed that 5-15 μm is a relatively optimal size which supports they ingrowth and survival [107]. The non-interconnectivity of pores, however, could impact their migration and proper spreading.

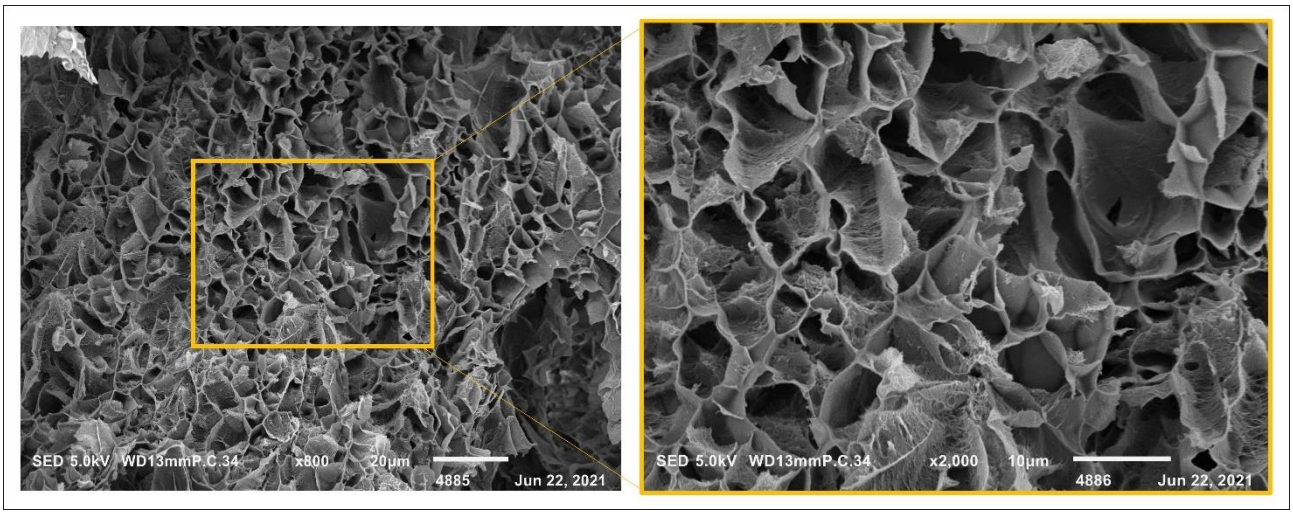

FIG. 15 GELMA/MATRIGEL INTERNAL MORPHOLOGY OBSERVED WITH SCANNING ELECTRON MICROSCOPY (SEM); Pictures show one of the three samples measured. Magnification is 800x for the left picture while the right picture is a detail of the left picture (2000x). The sample showed an average pore size of 9,654± 0.4125 μm.

5.1.4 GelMA/Matrigel hydrogel mechanical properties

The mechanical behaviour shown in Fig. 16 of the GelMA/Matrigel hydrogels was assessed via Dynamic Mechanical Analysis (DMA) by means of transient experiments in which the polymeric specimen is subjected to a gradual load and the deformation response is monitored over time. In the individual graphs of the three specimens in Fig.4, it is possible to observe the similar viscoelastic spectrum of the three 4% (w/v) GelMA/5%(v/v) Matrigel samples upon gradual compression of the three hydrogels. Approximately, deformation values of the GelMA/Matrigel hydrogel reach ca. 60% for compression lower than 200 kPa (Supplementary material Fig.4S).

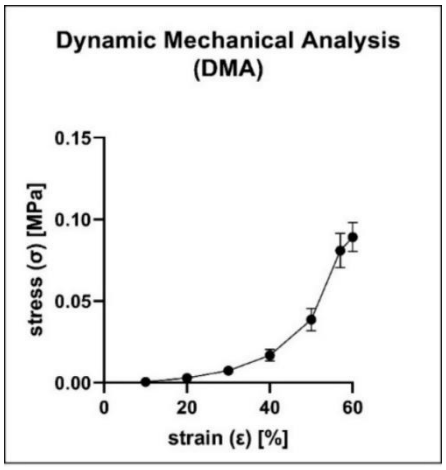

FIG. 16 SVISCOELASTIC BEHAVIOUR OF CELL-FREE GELMA/MATRIGEL HYDROGEL SHOWN AS STRESS STRAIN CURVE IN CIMPRESION MODE

5.2 HYDROGEL-BASED CELL CULTURE

Concurrent with the hydrogel characterization, a physiological-like multicellular breast cancer microtissue was established and characterized by incorporating murine stromal and parenchymal breast cancer cell lines. In particular, spheroids made of 4T1 breast cancer cells were embedded in the GelMA/Matrigel hydrogel containing NIH/3T3 fibroblasts in a pathophysiological-like ratio of 5:1 NIH/ 3T3:4T1. Following, the channel was endothelialized with H5V which are murine heart endothelial immortalized cells. The tri-culture model made of NIH/3T3 fibroblast, 4T1 cancer spheroids, and H5V endothelialized channel constitute the breast cancer microtissue (BCM).

In this part of the project, the cell-laden 4% GelMA /5% Matrigel hydrogel was tested for cell viability assays and protocols for the cell seeding and model assembly process was elaborated and optimized.

5.2.1 Stromal and cancerous cell lines viabilities

In Fig.17 A)-B), the cell viability of the 3T3 and 4T1 cell lines respectively were assessed via LIVE/DEAD while the metabolic activity was assessed with Alamar Blue assays (Fig.17 C). In the case of fibroblasts, cell viabilities of both $2*10^6$ cells/ml and $4*10^6$ cells/ml NIH/3T3 monocultures in GelMA/Matrigel hydrogel were assessed on days 4,7, and 10. Likewise, the relative metabolic activities of both the monocultures over time (day 1,4,7,10) were measured and normalized to day 1. The analysis of the relative metabolic activity yields more quantitative results and, contrarily to what was expected, reveals striking cell growth and proliferation rates at the lower density of $2*10^6$ cells/ml when compared with the higher cellular density ($4*10^6$ cells/ml) maybe because the denser cellular density constrains cells within the hydrogel hampering the proper spreading. In this model, however, we aimed at the generation of a high cellular density model for investigations on a densely packed stromal barrier and opted for $4*10^6$ cells/ml NIH/3T3. Similarly, the cell viability and relative metabolic activity of 4T1 breast cancer cell line within the 4% (w/v) GelMa/5% (v/v) Matrigel is reported below in Fig.17 C. Even in this case, the metabolic activity is subjected to an unexpected drop followed by a significant increase on day10. Overlapped and split GFP and RFP chaannels images of the LIVE (green) /DEAD (red) staining are reported below and, in

any case, show a growing trend in cell spreading and adhesion. While 4T1 breast cancer cells tend to aggregate and grow in a clustered fashion, NIH/3T3 fibroblasts follow an aligned and distributed pattern.

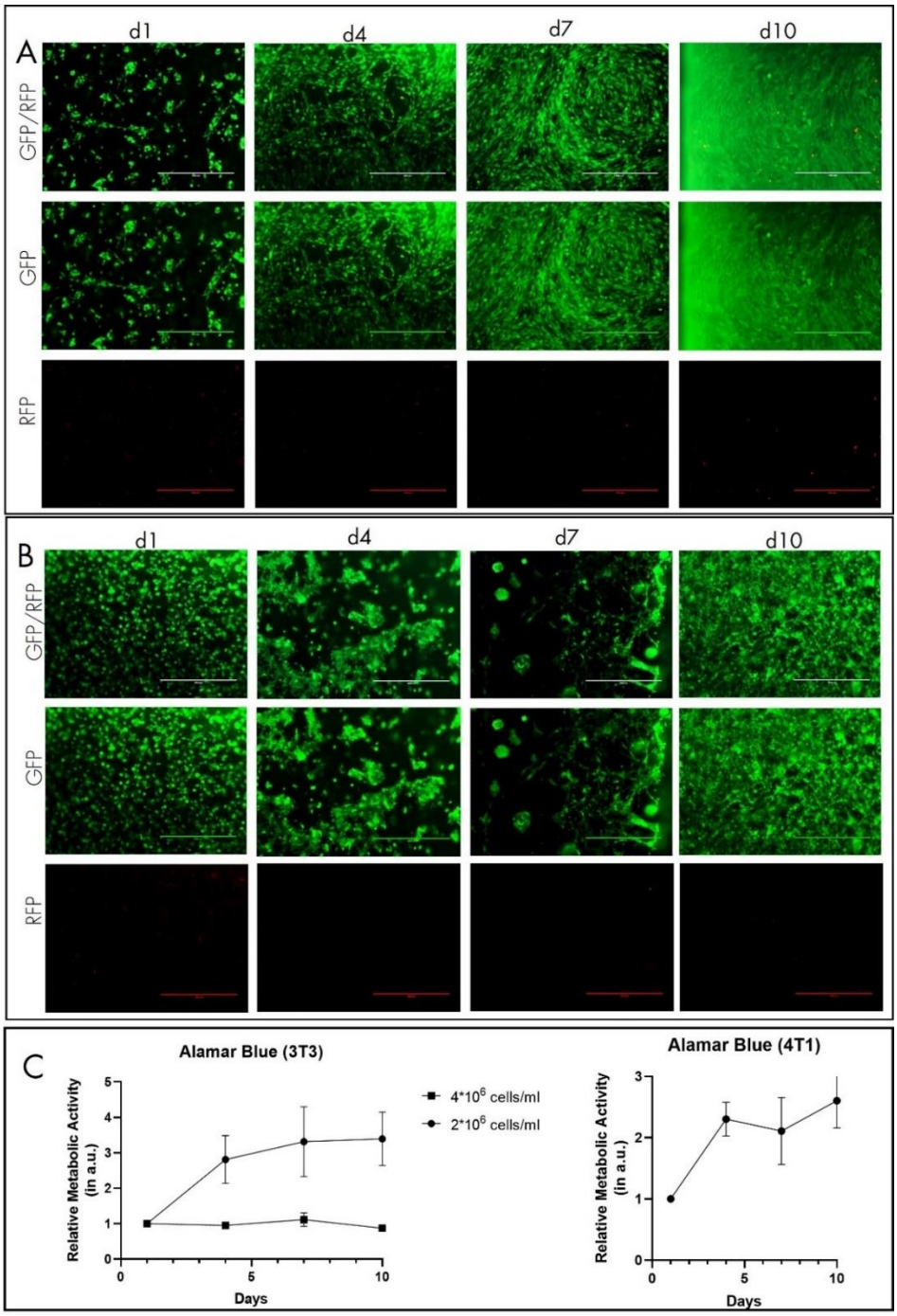

FIG. 17 HYDROGEL BIOCOMPATIBILITY VIA CELL VIABILITY ASSAYS A) LIVE (green)/DEAD (red) assay of NIH/3T3 fibroblasts monocultures in hydrogel with cellular density of $2*10^6$ cells/ml. Measurements were taken at d1, d4, d7, and d10 of culture. Pictures were taken at EVOS with 10x magnification to show cell viability, morphology, and distribution; B) LIVE (green)/DEAD (red) assay of 4T1 breast cancer cells monocultures in hydrogel with cellular density of $2*10^6$ cells/ml. Measurements were taken at d1, d4, d7, and d10 of culture. Pictures were taken at EVOS with 10x, magnification to show cell viability and morphology which, in this case show the formation of cell clustered indicated with white arrows; C) Metabolic activities of NIH/3T3 fibroblasts monocultures in hydrogel with cellular density of $2*10^6$ cells/ml and $4*10^6$ cells/ml and of 4T1 cells ($2*10^6$ cells/ml) were assessed with Alamar Blue assay (left and right respectively). Measurements were taken at d1, d4, d7, and d10 of culture and normalized to d1 in case of $2*10^6$ cells/ml 3T3 and 4T1 and normalized to the negative control of each day for $4*10^6$ cells/ml 3T3 . The graph shows the mean values and SEM of the triplicate for each data set.

5.2.2 Channel endothelialization of BCM

Following the endothelialization protocol, as shown in Fig.18, a confluent H5V coverage of the supernatant channels within five-seven days of dynamic (capillary force) culture was obtained. Cells injected from both, the inlet and outlet, needles readily adhered to the walls of the supernatant channel coated with Matrigel, elongated, and grown toward the middle part of the channel as shown in Fig.18A (day=0 of endothelialization) and in Fig.18B-C (day 5 and day 6 respectively), without evidencing the presence of necrotic areas. Furthermore, as shown in fluorescence microscopy, cells covered the entire circumference of the channels. No further changes in endothelial morphology were observed after four days of cultivation. After five-seven days of culture, a confluent monolayer of H5V was created (Fig.18C). Following the same endothelialization protocol but modifying the disposable plastic mould with two more needles, inlet and outlet, was possible to integrate and endothelialized a second channel in a parallel fashion within the same hydrogel. Moreover, success of the endothelialization protocol, morphology, and distribution of H5V cell line was assessed with Calcein-AM (green) assay on day 4 as reported in Fig.18 G,H.

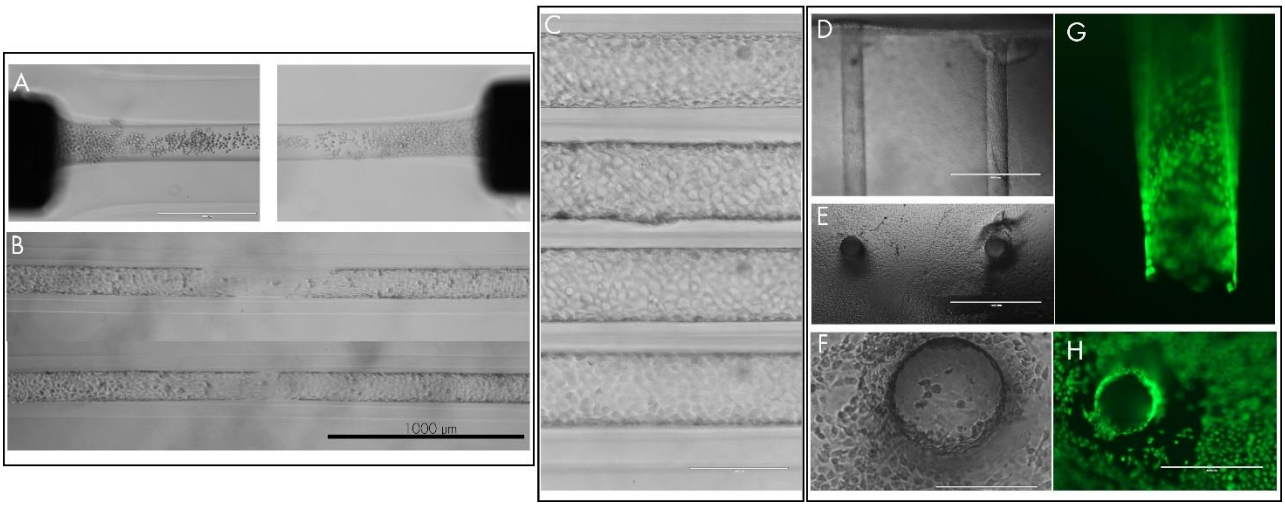

FIG. 18 CHANNEL ENDOTHELIALIZATION A) Channel (200 µm) extremities nearby the inlet and outlet needles (27G) right after H5V injection (day 0), bright field microscopy 4x B) Channel (200 µm) middle part on day 5 (above) and on day 6 (below) show the H5V cell growth and spreading within the channel, bright field microscopy 4x; C) Different plans (from the middle plan to the top plan) of the same channel (200 µm) part, bright field microscopy 10x; D) E) Endothelialization of two channels (200 µm) within the same hydrogel, top and side view respectively, bright field microscopy 4x; F) Side view of one of the two channel, some H5V cells came out of the channel and attached on the external surface, bright field microscopy 10x; G) H) Top and side view respectively of LIVE/DEAD assay on H5V cells within the channel (200 µm), fluorescence microscopy, 10x.

5.3 BREAST CANCER MICROTISSUE (BCM)

Two model were assembled for the final applications of this research project. The difference between the two models is given by the presence or lack of the stromal components, NIH/3T3 fibroblasts in this case. Thus, we have:

i) BCM $^{(-)}$ composed of 4T1 spheroids/sample and a confluent endothelial layer made of H5V (Fig. 19 A-E);

ii) BCM $^{(+)}$ composed of NIH/3T3, 4T1 spheroids/sample (in the ratio 5:1, NIH/3T3:4T1) and a confluent endothelial layer made of H5V (Fig.19 F-L);

While BCM $^{(-)}$ is used for investigating the effect of the endothelial barrier on molecules transport, the complete BCM $^{(+)}$ offers a more complete biological scenario with the inclusion of high cellular density stromal components. The visibility of the channel and spheroids is, with no doubts, clearer in the BCM $^{(-)}$ as shown in the bright field images below. However, although the high cellular density, it is still possible to discern BCM $^{(+)}$ components thanks to the transparency of the hydrogel.

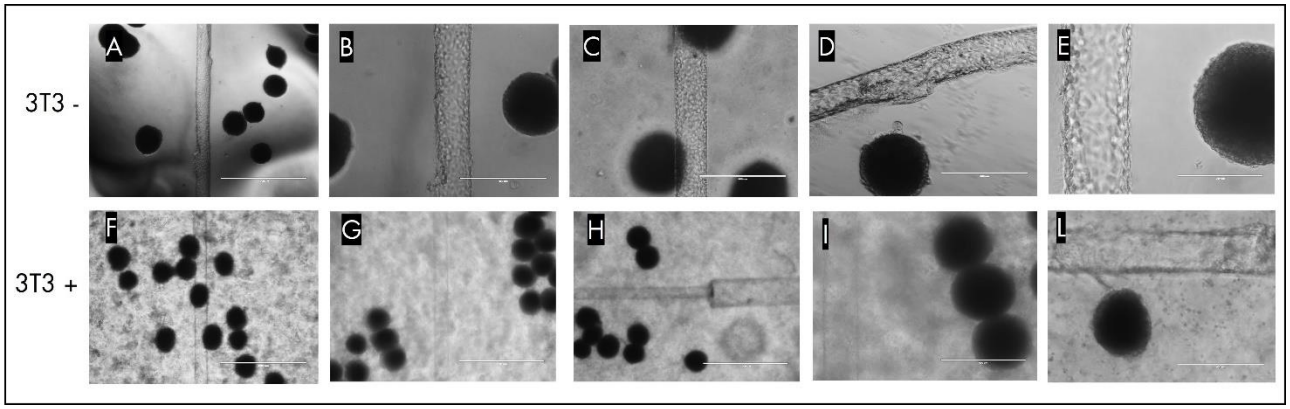

FIG. 19 FUNCTIONALIZED BREAST CANCER MICROTISSUES WITHOUT (A-E) AND WTH (F-L) STROMA (NIH/3T3 FIBROBLASTS).
Pictures were taken with bright field microscopy with the following magnifications: a) f) g) h) 4x; b) c) d) i) l) 10x; e) 20x. While in NIH/3T3 – hydrgoels, 4T1 spheroids and channel are neatly visualized, in NIH/3T3 + channel walls are less visible.

5.3.1 BCM model assembly and static cell-culture

As the final result of the cell seeding and endothelization protocols showed in Fig., the complete BCM $^{(-)/(+)}$ models are assembled as shown in Fig.20. This 3D BCM model owns high degree of reproducibility and tunability of the components' distribution within the hydrogel matrix. Ideally, 4T1 spheroids populations should be placed around and nearby the channel as shown in Fig. 20 A, possibly located on the same plane as shown in Fig. 20 (D,E,L) in which endothelial layer and spheroid's border are sharply observable. It should be avoided, instead, the deposition of spheroid merely above the channels as, due to gravity, they tended to precipitate risking the damage, and eventually the collapse, of the channel [supplementary material, Fig,6S]. The precise deposition of spheroids into the hydrogel around the channel was not always obvious as shown in Fig.20 B (right picture). Interestingly, during cell culture over the 10-days period, differences in hydrogels opacity and yellowing between the two conditions, BCM$^{(-)/(+)}$ were remarkable. After 9 days of culture, it is, indeed, very clear the observation of a different type of matrix, denser, certainly, less transparent, Fig. 20 E-H.

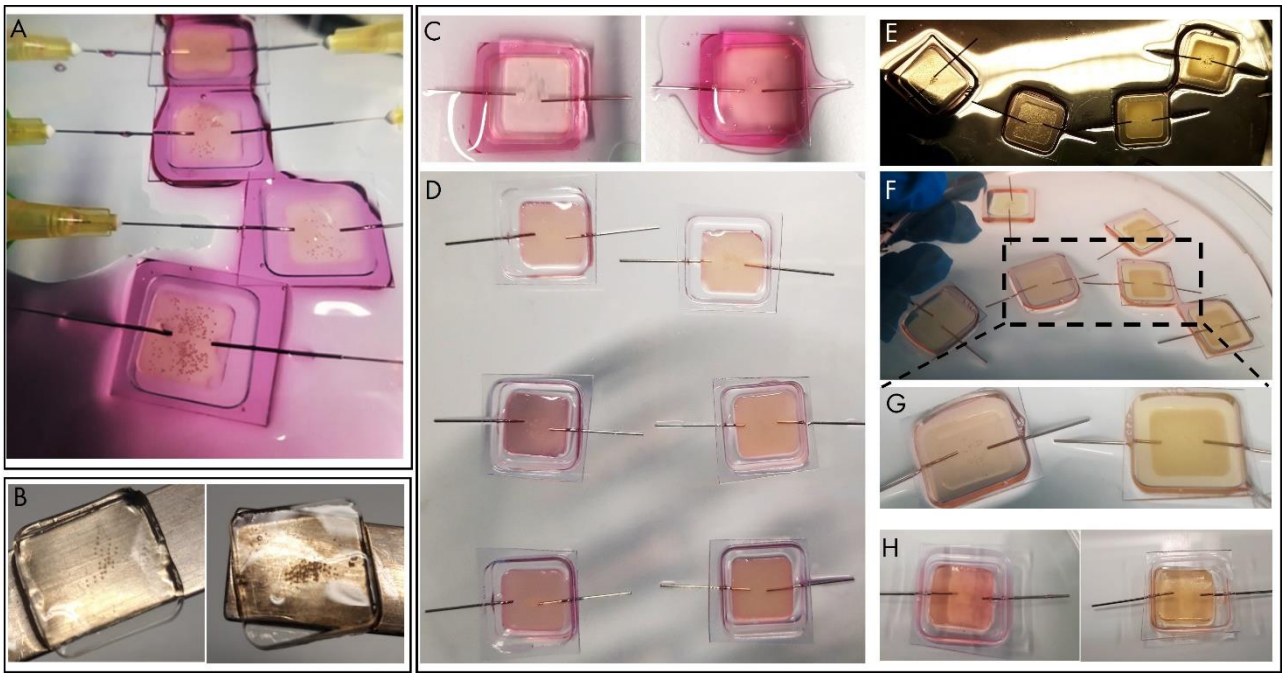

FIG. 20 BREAST CANCER MICROTISSUE ASSEMBLY AND CULTURE **A)** BCM on day 0 right after endothelial cell seeding, the yellow 30 G needles are inserted within the inlet and outlet needles; **B)** Stroma-free (NIH/3T3 -) hydrogels show the random distribution of 4T1 breast cancer spheroids within the hydrogel; **C)** Differences in stroma-free (NIH/3T3 -) (left) and stromal (NIH/3T3+) (right) hydrogels on day 0 of culture; **D)** Differences in stroma-free (NIH/3T3 -) (left side) and stromal (NIH/3T3+) (right side) hydrogels on day 4 of culture; **E)F)G)H)** Differences in stroma-free (NIH/3T3 -) (left) and stromal (NIH/3T3+) (right) hydrogels on day 9 of culture. The samples containing NIH/3T3 undergo a change in transparency and acquired a yellowish colour. All the pictures were taken with cell phone.

5.3.2 Qualitative approach - CellTracker™ staining

Prior to cell seeding, H5V cells and 4T1 spheroids were fluorescently labelled with CellTracker™ probes and their disposition in both, $BCM^{(-)/(+)}$, was assessed on day 1 of culture at EVOS . This qualitative analysis just gives us a hint on the cellular distribution within the microtissue and further emphasizes the less optical clarity due to NIH/3T3 fibroblasts presence. As mentioned above and as reported below in Fig. 21 (second raw) the presence of fibroblasts reduces the signal intensity of spheroids (in green) and of channel (red) compared to the non-stromal microtissue (red spheroids and green channel).

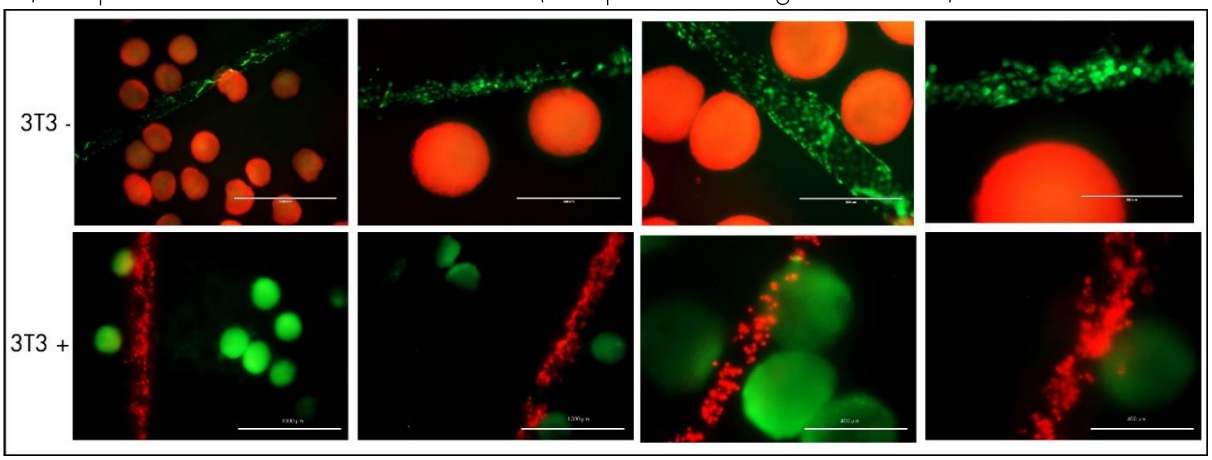

FIG. 21 BCM CELL TRACKER LABELLING H5V ENDOTHELIAL CELLS AND 4T1 BREAST CANCER SPHEROIDS WERE LABELLED BEFORE CELL SEEDING INTO THE HYDROGEL. In NIH/3T3- hydrogels, 4T1 spheroids are labelled in red and H5V cells in green, while in NIH/3T3+ hydrogels, 4T1 spheroids are in green and H5V cells in red

5.4 BCM MODEL CHARACTERIZATION

After the characterization of GelMA/Matrigel hydrogel in terms of biomaterial's stability, versatility, mechanical and optical properties, it followed the characterization of the GelMA/Matrigel hydrogel in terms of cell viability, biocompatibility, and tunability of cellular components within the hydrogel. Simultaneously to this second phase, further characterization was conducted at the level of the whole BCM model in parallel. Given the different natures of characterizations necessary for the description of this model, this phase was conducted all over the project duration. Specifically, each characterization step was carried out upon optimization steps. In other words, when the hydrogel composition was defined after a broad biomaterials study, the acoustical characterization was conducted right away to assess the suitability of the model in the acoustical set-up. Similarly, when the cell viability of the hydrogel was estimated, mechanical and biological characterization of the model was assessed. The progressive characterization of the model did in such a manner as to adopt BCM subtypes ($BCM^{(-)}$ and $BCM^{(+)}$) according to the relevancy of the analysis. Results from different characterizations are reported below.

5.4.1 ACOUSTICAL CHARACTERIZATION

Cell-free hydrogels and $3T3^{+}$-laden hydrogels ($4*10^{6}$ cells/ml) were acoustically characterized. After assessing the optical clarity, in this analysis, we analysized the acoustical clarity of the model and thus its suitability for acoustical applications with a small attenuation or distortion of the US beam. In this analysis, we aimed at measuring the attenuation coefficient **α** which indicates how easily a volume of material can be penetrated by a beam of sound. Large attenuation coefficients imply a quick "attenuation" (weakened) of the beam as it passes through the medium, and a small attenuation coefficient means that the medium is relatively transparent to the beam, so there is no attenuation. Here, attenuation was measured from 30-cycle ultrasound pulses transmitted over a frequency range from 0.7 to 5 MHz at peak negative acoustic pressures ranging from 10 kPa to 100 kPa, by increments of 10 kPa. To measure attenuation, first, a reference signal was recorded, i.e., we have measured the amplitude of a signal that travels through the water to the receive transducer. Then the sample was placed between the transducers at the focal point of transmit transducer and the attenuated signal was measured. The longitudinal attenuation in respect to the water is calculated using the below relation:

$$\alpha = 20 \times \log \frac{I_{hydrogel}}{I_{Reference}} \qquad \text{ATTENUATION COEFFICIENT } \alpha \text{ [dB/cm]}$$

Where

$I_{incident}$ =intensity of the incident (transmitted) wave.

I_{ref}= intensity of reflected wave relative to the

In comparison to water, it was observed a very small attenuation which oscillates around zero for pressure intensities in the range of 10-100 kPa of both cell-free and cell-laden GelMA/Matrigel meaning that hydrogels are acoustically transparent. The observed fluctuations in the attenuation curves originate, in fact, from the reflections and constructive or destructive interference of pressure waves. The peak in attenuation recorded in the range 0.5 -1 MHz of the cell-laden hydrogel (Fig. 22 right) is given by a mistake in data acquisition. The recording length of oscilloscope was not adjusted properly to record the signals at a low frequencies.

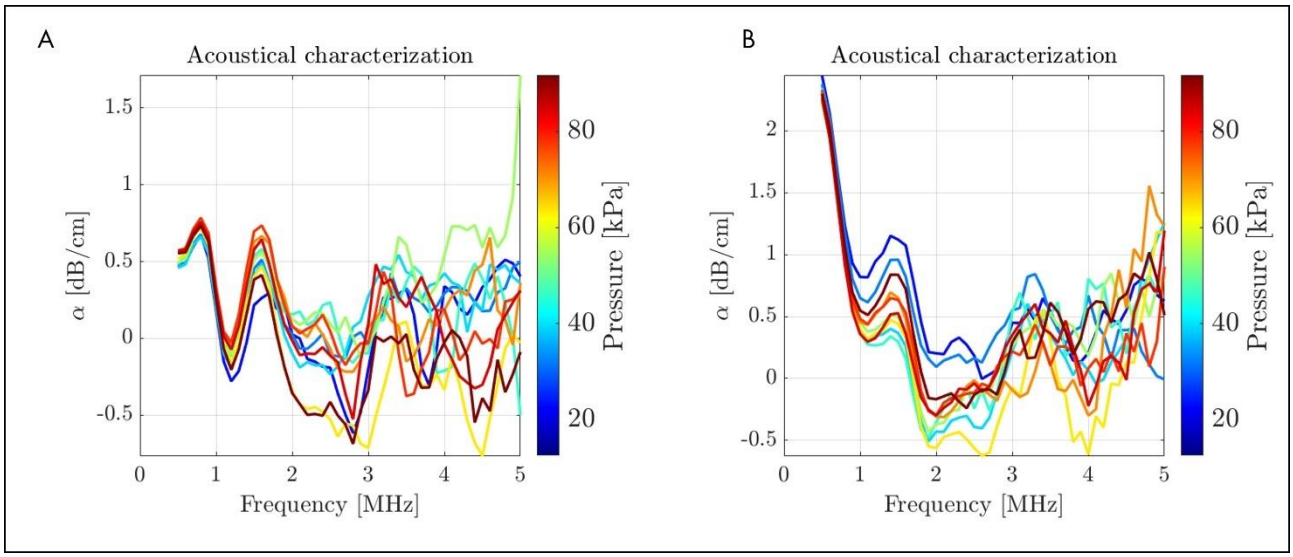

FIG. 22 ACOUSTICAL CHARACTERIZATION OF CELL-FREE (LEFT) AND CELL-LADEN (RIGHT) GELMA/MATRIGEL HYDROGEL

5.4.2 BIOLOGICAL CHARACTERIZATION

5.4.2.1 H&E STAINING: MORPHOLOGY OF THE BCM

H&E staining was performed to observe the morphology of the BCM $^{(+)}$ model and to yield a qualitative analysis relative to both biological and structural relevance. In Fig. 23, side (Fig 23 A-D) and top (Fig. 23 E-F) views of 10 µm thick sections of the BCM $^{(+)}$ are reported. Pictures were taken with 2,5x, 10x, and 1x magnifications and provide a more concrete idea of the model architecture, of the variability of cell distribution within the tissue and around the channel, and eventually, of the tissue size itself. Situations in which tumor spheroids are in the proximity of the channel as shown in Fig.23 C were more common compared to situations as depicted in Fig.23 A in which the tumor spheroid is located very distantly from the channel. It is also interesting to point out the NIH/3T3-given ECM which characterized the BCM $^{(+)}$ stroma surrounding the channel and the tumor spheroids. In Fig. 23 D, the detail of the channel shows the presence of endothelial cells attached around the channel and a more consistent ECM surrounding it. The samples, large ca. 12x12 mm and thick 4-5mm were sectioned on the side (XY) as discussed so far, but also, they were sectioned from the top (XZ) to yield another perspective of the tissue morphology. From top views (Fig.23 E, F), the disposition of tumor spheroids around the channel can be observed. Detail is given in Fig.23 F in which the endothelial wall and the tumor spheroids are indicated by arrows. From the top view of the sectioned tissue, emerged the discontinuity of the endothelial walls and thus that the channel was not completely coplanar (it was not possible to have it all in the same 10 µm tissue slice). For the aim of our project, the non-coplanarity of the channel was not an issue because we were always able to have the vessel walls on focus but if it is particularly accentuated it might yield discrepancies in some measurements.

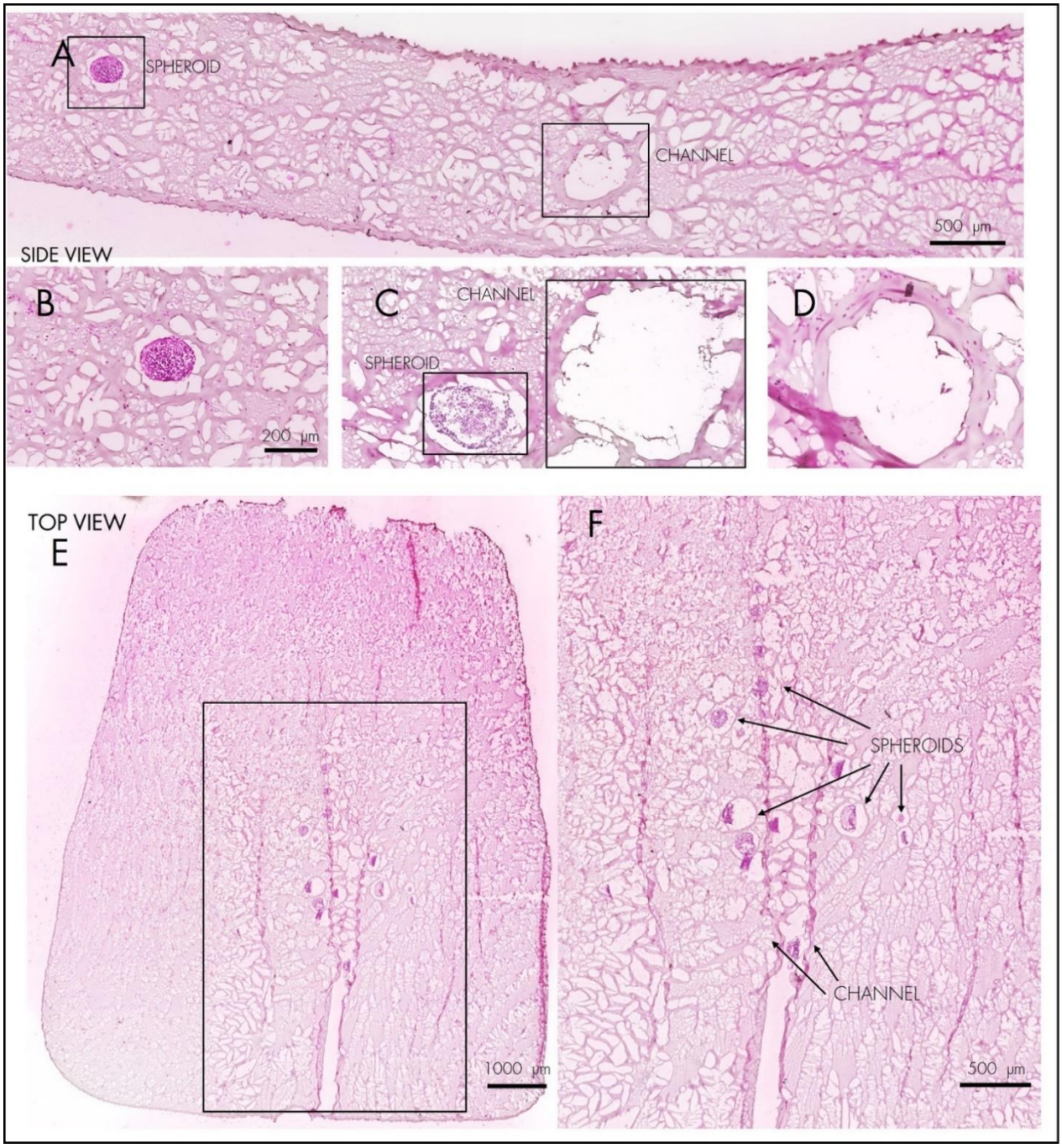

FIG. 23 HAEMATOXYLIN & EOSIN (H&E) OF BC SIDE AND TOP SECTIONS, CELL NUCLEI ARE IN PURPLE WHILE ECM AND CYTOPLASM ARE IN PINK SCALE; A) C) Side sections of the BCM in which the endothelialized channels and the tumor spheroids are indicated; MAGNIFICATION 2.5X; B) Side section of the BCM, detail of 4T1 spheroid; magnification 10x; C) Side section of the BCM, detail of 4T1 spheroid nearby H5V channel; magnification 10x; D) Side section of BCM, detail of H5V endothelialized channel; magnification 10x; E) Top view of the BCM; magnification 1x ; F) Detail of the top view (E) in which the channel, and the tumor spheroids are well visible, magnification 2,5x.

5.4.2.2 PROTEIN EXPRESSION IN BCM

To investigate the protein expression within the microtissues, we sectioned the cryopreserved tissues with a FSE cryotome and stained them with cytokeratin 19, collagen 1α, and vimentin whether on day 7 [Supplementary Material, Fig.8S] and on day 14. This immunohistochemical staining was aimed at a better characterization of the BCM $^{(+)}$ content via the expression of key stromal (collagen 1α and vimentin), and cancerous (CK19) proteins. In the case of tumorigenic features, the spheroids were found to be highly positive for the CK19 staining thus indicating the presence of epithelial 4T1 breast cancer cells embedded in the tissue (Fig. 24 A, B). The surrounding area around the four spheroids showed in these pictures, therefore, resulted in to have solely consisted of NIH/3T3 which showed very little expression of CK19. Vimentin staining revealed that 4T1 breast cancer spheroids on day 14, not only expressed the epithelial marker CK19 but also showed a significant expression of the mesenchymal marker vimentin in the outer shell of the spheroid indicating loss of epithelial features, and acquired migratory phenotype of 4T1 cells in contact with the surrounding ECM matrix (Fig.24 E,F).The area stained positive for Collagen1-1α, a very representative ECM protein, (Fig.24 C, D) surrounds the tumor spheroids and covered the entire tissue section with a higher expression on the tissue border likely in concomitance with high fibroblasts cell-spreading.

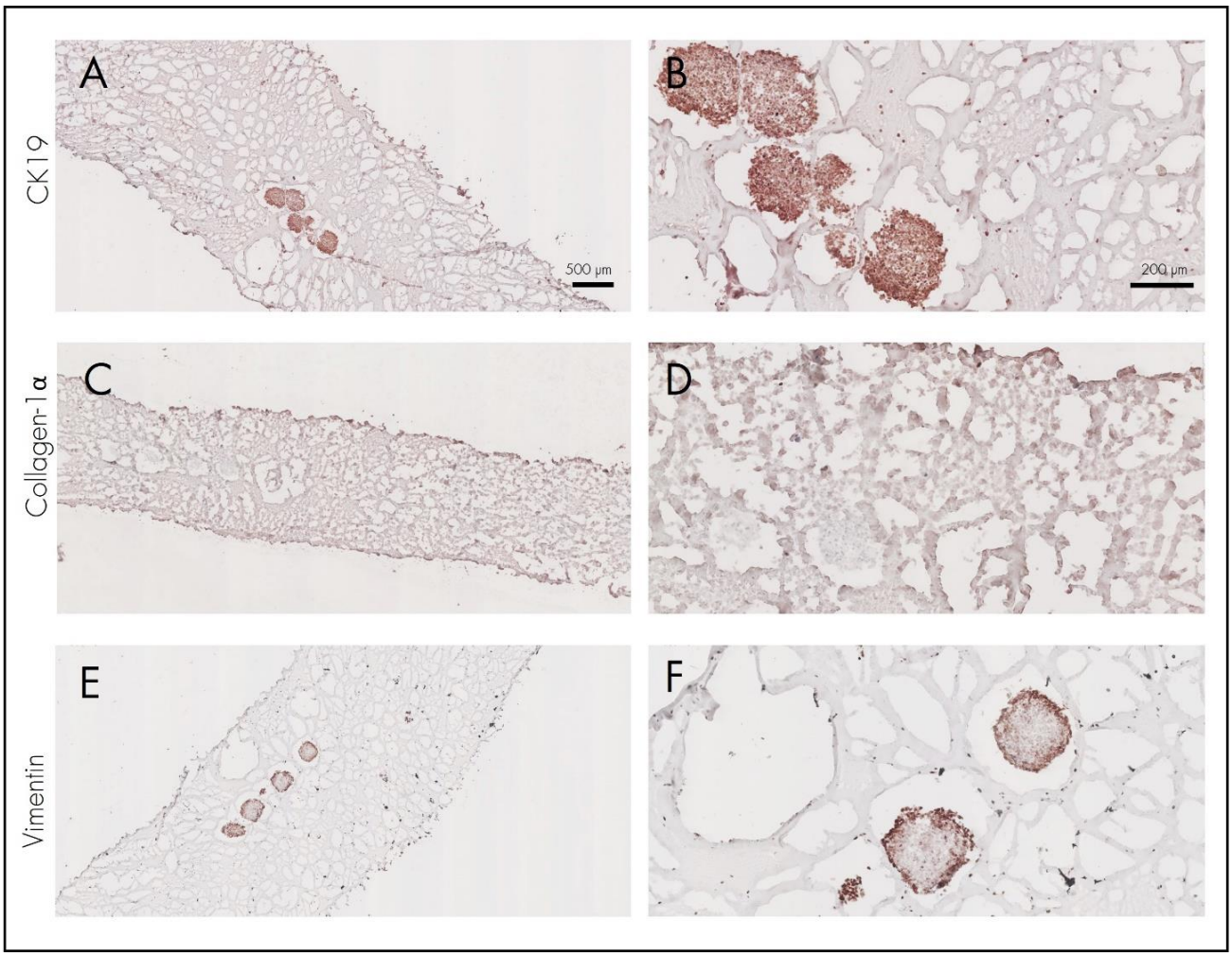

FIG. 24 IMMUNOHISTOCHEMICAL STAINING OF BCM AT DAY 14; A) B) Protein expression of Cytokeratin 19 (CK19) at 2.5x (A) and 10 x (B); C) D) Protein expression of Collagen-1 at 2.5x (C) and 10x (D); E) F) Protein expression of Vimentin at 2.5x (E) and 10x (F);

5.4.2.3 TUMORIGENICITY AND CLINICAL RELEVANCE OF THR BCM

The effects of GelMA hydrogels on cells fate were further examined evaluating gene expression using the quantitative polymerase chain reaction (qPCR) approach. In this analysis, 2D and 3D monocultures of the respective cell lines were compared, and results are reported in Supplementary Material, Fig 7S.

The biological relevance of the BCM model was, instead, furtherly assessed by separately measuring the gene expression of 3D monocultures of NIH/3T3 and of 4T1 spheroids in hydrogel and comparing it with the 3D co-culture in hydrogel to estimate the relative gene expression contribution given by both stromal and cancerous cell lines in the BCM model. To compare the three different datasets the $2^{-\Delta CT}$ method was preferred over the $2^{-\Delta\Delta CT}$ method. The $2^{-\Delta CT}$ equation, in fact, doesn't include a reference gene and it was used to estimate the relative contribution of the two cell lines to the co-culture model gene expression according to the results of the singular monocultures. The expression of different stromal or tumorigenic markers and their relative up- and downregulation in the 3D co-culture environment was evaluated with qPCR analysis performed on monocultures and co-cultures at day 4. Notably, the $H5V^{(-)}$ BCM in which NIH/3T3 and 4T1 spheroids are cultured (5:1), is particularly characterized by a very high expression of vimentin followed by fibronectin. Notably, mesenchymal marker vimentin resulted in to be particularly expressed in all the conditions showing an average expression of 172 in the co-culture model deriving, to a greater extent, from 3T3 fibroblasts, which instead showed an average value of 73 compared to the 4T1 3D monocultures (56,74). Fibronectin (Fn1), on the other hand, showed a drastically difference between 3D monocultures as NIH/3T3 showed an average of 215,3 while 4T1 spheroids showed more moderate values (79,8), resulting however in an increased expression in the co-culture (151,05) and thus higher invasiveness. This result, together with the downregulation of E-cadherin (E-cad) from 4T1 monocultures (1,32) to the co-culture with fibroblasts (0.82) confirms that 4T1 tumor cells underwent EMT in BCM and differentiated toward a mesenchymal phenotype. Levels of the Pdgfr-β, more accentuated in NIH/3T3 3D monocultures (2,73), provide additional indications of the transition towards a mesenchymal and migratory phenotype of the BCM (1,64) if compared to the 4T1 monocultures (0,96). Contrarily, a significant upregulation in Mmp-9 expression, which suggests the extent of cellular differentiation in breast cancer cells, was found in 4T1 tumor spheroids monocultures (6,93) when compared to co-culture tissues (1,94). The close relation between pro-fibrotic Tgf-β and pro-inflammatory tumor necrosis factor (Tnf)-α was shown here as they were found to be similarly expressed in the co-culture models (2,86 and 2,83 respectively) and downregulated in compared to the 3D monocultures of 4T1 (4,51 and 4,64 respectively). Angiogenic Vegf instead, initially more expressed in fibroblasts monoculture (0,99), displayed a slightly lower, but not significant, expression in the co-culture tissue (0,55). Interestingly, hypoxia representative gene hypoxia-inducible factor 1 α (Hif-1α) was slightly upregulated in the co-cultures with an average values of 1,76 when compared to the two singular monocultures, 1,34 for 3T3 and 0,94 for 4T1 spheroids. Unexpectedly, the expression of stromal markers such as α-SMA, integrin subunit alpha 5 (Itga5), and periostin (Postn) as well as tumor-associated drug resistance marker (Abcg2) presented very low expression in both, monocultures and co-culture conditions.

Nevertheless, to confirm the tumorigenic trends of the $H5V^{(-)}$ BCM model and to support its clinical relevance, a transcriptomic analysis of the publicly available data of TNBC patients was conducted.

In the dataset GSE65194, data from 11 TNBC patients and control patients was analysed to know the significance of the altered genes. Interestingly, we observed that all the genes showing upregulation in our microtissues also showed significant overexpression in TNBC patients when compared to the control patients. The genes which are most altered in the co-cultured microtissues and significantly altered in the patients are shown in Fig.25B.

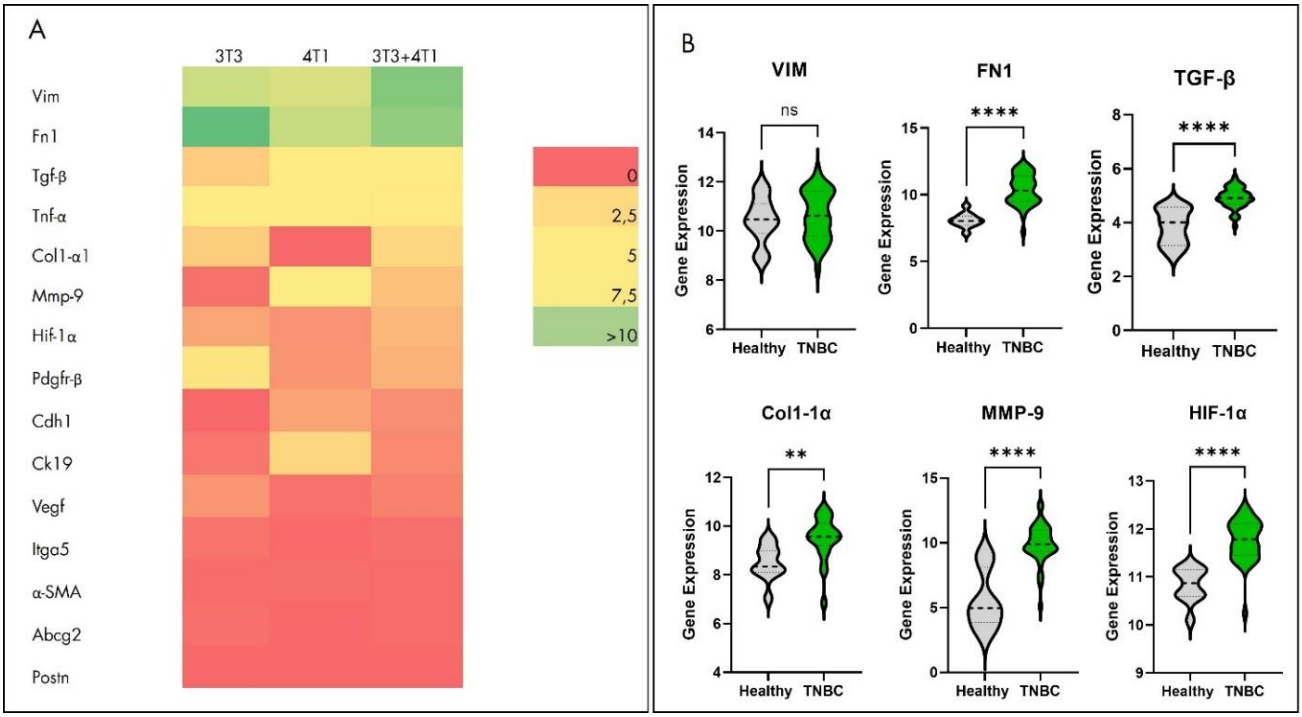

FIG. 25 TUMORIGENICITY AND CLINICAL RELEVANCE OF THE BCM; A) Gene expression of NIH/3T3 and 4T1 3D monocultures in hydrogel and the gene expression of NIH/3T3 and 4T1 3D co-culture in hydrogel were compared to assess the relative contribution of the two cell lines to the tumorigenicity of the BCM; B) Comparative transcriptomic analysis in human TNBC patients from public database GEO () for genes found to be upregulated in the 3D breast cancer microtissue.

5.4.3 MECHANICAL CHARACTERIZATION

Following fixation on days 0,5, and 10, microtissues composed of $4*10^6$ cells/ml NIH/3T3 and 4T1 spheroids in ratio (5:1) were subjected to mechanical characterization via DMA in compression mode performed as in the hydrogel mechanical characterization This analysis was conducted based on the hypothesis of microtissue stiffening due to enhanced ECM deposition by fibroblasts or cellular proliferation as observed in desmoplastic reactions typical of breast carcinomas. In other words, the mechanical characterization of cell-laden hydrogel can be used to observe a hypothetical extent of stiffening and to yield a further description of the tumorigenic stroma recapitulated in this model. Stress-strain curves of cell laden GelMA/Matrigel are reported below in Fig. 26 and show a similar trend among days 5 and 10, while day 0 is significantly characterized by higher stiffness inasmuch, for equal values of deformation, a higher stress should be applied. Unexpectedly, however, the stiffness feature of cell-laden hydrogels over time attenuated, showing lower rigidity on day 10 which, yet remains higher than the cell-free hydrogel.

Given the lack of statistical significance among the three independent replicates, however, these curves can just qualitatively describe the mild changes observed in the microtissue mechanic over 10-days culture. The decrease in compressive modulus over time could be given by a degradation in the hydrogel matrix which make the whole structure weaker from day 0 to day 10.

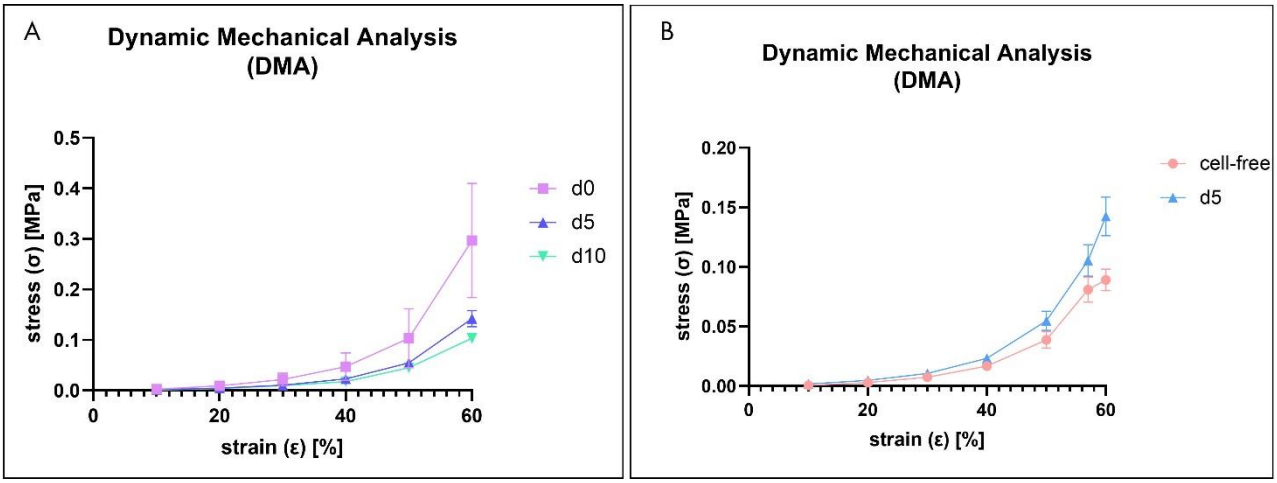

FIG. 26 STRESS-STRAIN CURVE OF CELL-LADEN (3T3+; H5V-; 4T1 SPHEROIDS +) HYDROGEL AND COMPARISON WITH CELL-FREE HYDROGEL; MECHANICAL CHARACTERIZATION THROUGH DMA IN COMPRESSION MODE. **A)** stress-strain curve of cell-laden hydrogels at day 0, 5, and 10 shows a decrease in overall stiffness; **B)** comparison of stress-strian curve of cell-free and cell-laden hydrogel at day 5 shows difference in stiffness, with cell-laden hydrogel stiffer than cell-free. Data represents mean ± SEM for at least 3 independent experiments. *$p < 0.05$, **$p < 0.01$, ***$p < 0.001$

5.5 MOLECULES TRANSPORT WITHIN THE BCM

Following a broad multidisciplinary characterization phase in which we showed both the biological and clinical relevance of the proposed BCM, in the third part of this project, we aimed at its application for molecules transport studies. In particular, we aimed at showing the adequate suitability of the model to this type of application by recapitulating and showing the impediment that biological diffusion barriers constitute within the tumor milieu in the specific case of breast carcinomas. As mentioned in the first part of this report, in such desmoplastic cancers, the greater physical barrier is constituted by a dense and aberrant deposition of ECM molecules responsible for increased solid stress and which, along with high IFP, contributes to therapeutic failure. The resulting impenetrable barrier in fact makes diffusion and penetration of anticancer agents insufficient risking suboptimal therapeutic regimens. By employing the cell-free hydrogel and the two configurations of the microtissues, BCM $^{(-)/(+)}$, it was thus possible the qualitative analysis of the limited diffusion of different molecules upon the presence of both, the endothelial barrier in BCM $^{(-)}$ and the endothelial-stromal barrier in BCM $^{(+)}$ using cell-free hydrogel as control.

5.5.1 Rhodamine B transport within the BCM $^{(-)/(+)}$

Time-lapse fluorescence microscopy of cellular transport of Rhodamine B is Fig.27 D. All the images were obtained by perfusing Rhodamine B in BMF solutions for 10 min at a perfusion rate of 10 µl/min. As shown below, the distribution profile of Rhodamine B is very sharp and neat suggesting a very homogeneous distribution within each BCM. Further confirmation of the homogenous diffusion of Rhodamine B is given by the signal profile plots shown in Fig. 27 C in which the relative plateau of signal intensity is reached in all the measurements regardless of the cellular conditions (Fig. 27 C top) and of the time points (Fig. 27 C bottom). The local fluorescence intensity is indeed proportional to local Rhodamine B concentration. Interestingly, in Fig.27 D. for NIH/3T3^{+} microtissue the distribution profile of Rhodamine B follows the morphology of the tissue and in particular of the spheroids nearby the channel. What changes in the three different conditions, cell-free, BCM (-), and BCM (+) respectively, is the diffusion distance of Rhodamine B from the channel over a 10 min period. As hypothesized, higher diffusion distances of Rhodamine B were observed in the cell-free hydrogels, followed by stroma-free hydrogel (BCM$^{(-)}$), and eventually by stroma-laden hydrogel (BCM$^{(+)}$). The statistical significance in Rhodamine B diffusion was present between BCM $^{(-)}$ and cell-free models at 5 min whereas at 10 min significant difference was observed between BCM$^{(-)}$ and BCM$^{(+)}$ models, as shown in Fig. 27 B. In the signal intensity profile plots, besides the equal plateau, the different curve slopes are all parallel, implying the equal signal intensity but at different distance the curve related to cell-free hydrogel is (delayed) broader since the diffusion distance is higher.

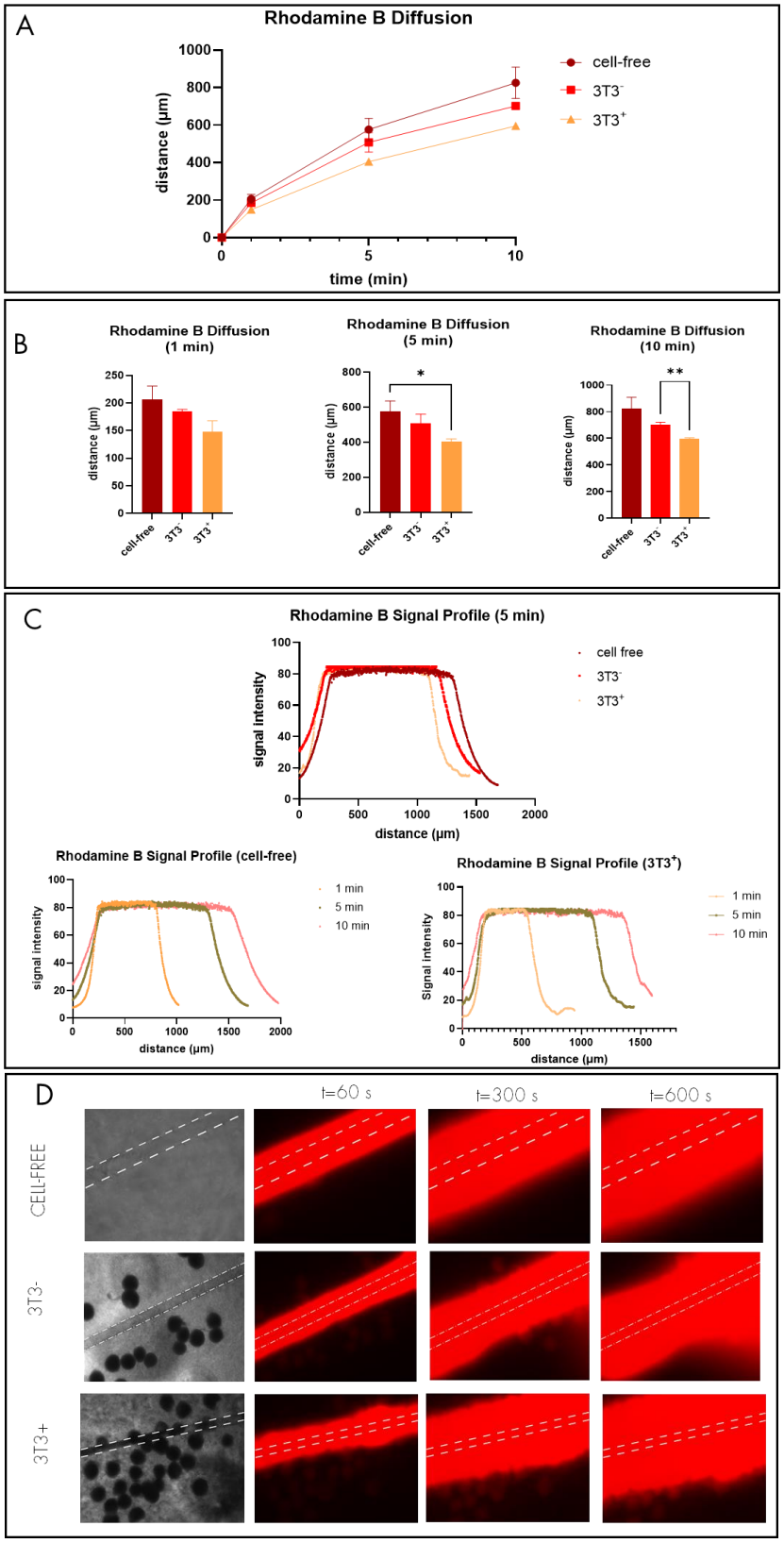

FIG. 27 RHODAMINE B DIFFUSION AND SIGNAL PROFILES INTO THE BCM; A) Diffusion curves of Rhodamine B within cell-free, 3T3-, and 3T3+ BCM for the evaluation of Rhodamine B transport in the presence of endothelial barrier [H5V+; 4T1+; 3T3-] and endothelial and stromal barriers [H5V+; 4T1+; 3T3+]; B) Diffusion of Rhodamine B at time points 1, 5, and 10 min in BCM(+)/(-) models. Data represents mean ± SEM for at least 3 independent experiments. *p < 0.05, **p < 0.01, ***p < 0.001; C) Rhodamine B signal intensity profiles comparison in cell-free, 3T3-, and 3T3+ BCM at 5 min of perfusion (top); Rhodamine B signal profiles comparison in cell-free (bottom left) and 3T3+ (bottom right) at 1,5-, and 10-min D) Perfusion of rhodamine b in the three model conditions, cell-free, stroma-free (3t3-) and with stroma (3T3+).

5.5.2 FITC Dextran 10 kDa transport within the BCM $^{(-)/(+)}$

Similarly, FITC Dextran 10kDa diffusion studies were performed using the same experimental set-up. Having a larger size (Mw and hydrodynamic radius) than Rhodamine B, we had supposed FITC Dextran 10 kDa to diffuse slower within the BCM.

Even in this case of FITC Dextran 10 kDa, the differences in diffusion distance from the channel due to the physical barriers' impedance are measurable (Fig.28A) but less accentuated compared to Rhodamine B diffusion. Notably, the differences in diffusion distance are not appreciable and significant as in the first case of Rhodamine B as shown in Fig. 28A. The diffusion distance curves are indeed very close to each other with a significant difference just between the cell-free model and BCM $^{(+)}$ at 10 min, Fig.11B. Furthermore, in the case of FITC Dextran 10 kDa, the diffusion profile is less neat and more heterogeneous compared to the first case as can be observed in the microscopy frames (Fig.28D bottom). However, the dye solution is more confined by the surrounding cellular or non-cellular matrix as shown in the narrow bell-shaped signal profile plots (Fig. 28 C, D). Therefore, in the case of larger molecules are more appreciable differences in signal intensity, and thus in molecules' local concentration, as shown in Fig. 28 C,D rather than in diffusion distance as used for Rhodamine B. In this case, the presence of the dense stroma made of NIH/3T3+ is what mostly hampered the diffusion of FITC Dextran 10 kDa while no striking difference was observed between cell-free and BCM$^{(-)}$ models.

Importantly, observing the diffusion rates of Rhodamine B and FITC Dextran10 kDa, they behave differently in the three microtissue conditions. Alternatively, we can say biological barriers affect molecules' diffusion differently, depending on the molecule size. After 10 min, in the case of Rhodamine B (ca.1 nm), diffusion attenuation is the same (15%) from cell-free hydrogel to BCM$^{(-)}$ and from BCM$^{(-)}$ to BCM$^{(+)}$: Therefore there is a decrease in diffusion by 30% from cell-free hydrogel to BCM$^{(+)}$. There is no difference between diffusion rates through the endothelial and the stromal barrier may be due to the excessive small size of Rhodamine B molecules which experience the same flow resistance regardless of the biological barrier. FITC Dextran (10 kDa) molecules (ca.4-5 nm), on the other hand, show different extents of transport impediment depending on the biological barrier inasmuch the diffusion rate from cell-free to BCM$^{(-)}$ is attenuated by 15% while from BCM $^{(-)}$ to BCM $^{(+)}$ is decreased by 28,5% indicating a further reduction of 13,5% in the presence of the dense stroma. However, from these data, oppositely of what was expected, it appears that the endothelial barriers yield equal flow impediment regardless of the molecular size of dyes, as we measured ca. 15% in diffusion reduction from cell-free to endothelialized channel for both FITC Dextran (10 kDa) and Rhodamine B. According to this data, we can assume that the endothelial barrier is equally permeable to FITC Dextran (10 kDa, ca. 4-5 nm) and Rhodamine (ca.1 nm) as the endothelium is usually permeable to molecules ranging from 0.1 nm (ions) to 11.5 nm (such as immunoglobulins). In this case, according to what was reported by Sukriti et al. and by Dravid et al., the transport of FITC Dextran 10 kDa (larger than 3 nm) as well as of other macromolecules such as albumin, would occur through the transcellular pathway, also defined as transcytosis or vesicular transport. On the other hand, Rhodamine B (smaller than 3 nm) together with glucose, water, and ions, would pass via endothelial junctions, and thus via the paracellular pathway. Both transcellular and paracellular pathways work simultaneously to maintain the oncotic tissue pressure and ensuring the endothelial barrier [108 109].

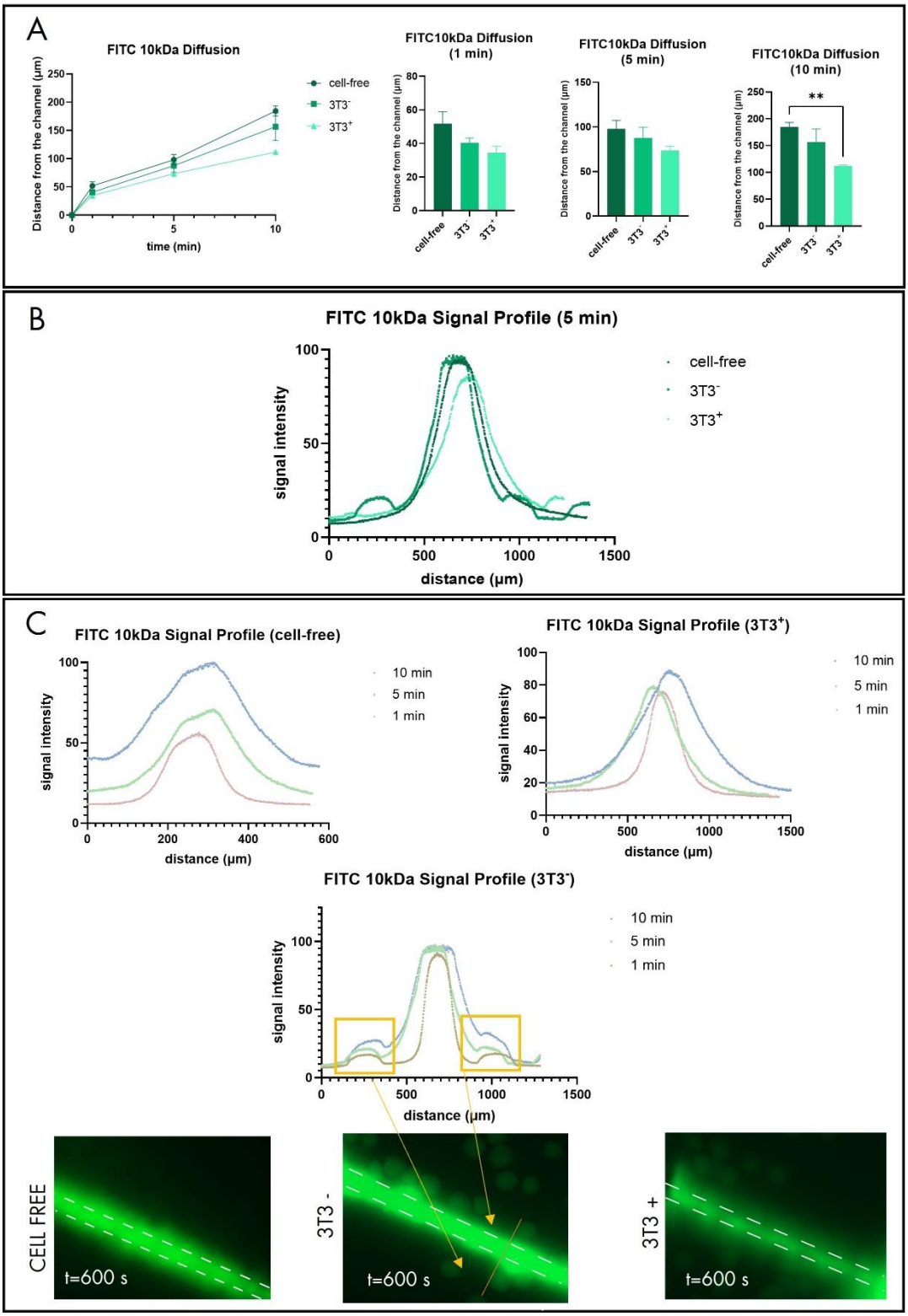

FIG. 28 FITC Dextran 10 kDa DIFFUSION AND SIGNAL PROFILES INTO THE BCM; A) Diffusion curves of FITC Dextran 10 kDa within cell-free, 3T3-, and 3T3+ BCM for the evaluation of FITC Dextran 10 kDa transport in the presence of endothelial barrier and endothelial with stromal barriers; On the right Diffusion of FITC Dextran 10 kDa at time points 1 , 5, and 10 min in cell-free and BCM$^{(+)/(-)}$ models. Data represents mean ± SEM for at least 3 independent experiments. *p < 0.05, **p < 0.01, ***p < 0.001; B) FITC Dextran 10 kDa signal intensity profiles comparison in cell-free, 3T3-, and 3T3+ BCM at 5 min of perfusion (top); C) FITC Dextran 10 kDa signal profiles comparison in cell-free (top left), 3T3- (top middle), and 3T3+ (top right) at 1,5, and 10 min; Frames of FITC Dextran 10 kDa diffusion in within cell-free model at t=10 min (bottom left); frames of FITC Dextran 10 kDa diffusion in 3T3- model at t=10 min (bottom left). The contribution of spheroids to the signal profile is highlighted; frames of FITC Dextran 10 kDa diffusion in 3T3+ model at t=10 min (bottom right). Fluorescence microscope via EVOS 4x.

5.5.3 Molecules transport within the BCM (+)

Finally, to have a more complete dataset, the diffusion rates of molecules of different sizes were assessed within the BCM (+) model. Besides Rhodamine B and FITC Dextran 10 kDa, in fact, also the diffusion profile of FITC Dextran 70 kDa and of Silica NPs in stroma-laden BCM was measured. As shown in Fig.29A-B, there are significant differences among the diffusion curves of the different molecules with FITC Dextran 70 kDa showing a moderate diffusion rate even compared to FITC Dextran 10kDa, and Silica NPs whose extravasation through the vessel wall was already hard to observe as shown in Fig. 29 A. For the latter in fact, the diffusion rate into the BCM was approximated to zero. In Fig. 29 A the sequences of time-lapse frames over time are reported to yield a qualitative analysis of the diffusion distance of different molecules within the BCM (+). Interestingly, the signal intensity profiles of FITC Dextran 10 and 70 kDa were compared (for t=5 min). While FITC Dextran 10kDa diffused heterogeneously, low concentrations area, fluorescent dye, FITC Dextran 70 kDa diffused as slower as more homogeneously due to the larger size of molecules without generating areas with more or less dye concentration.

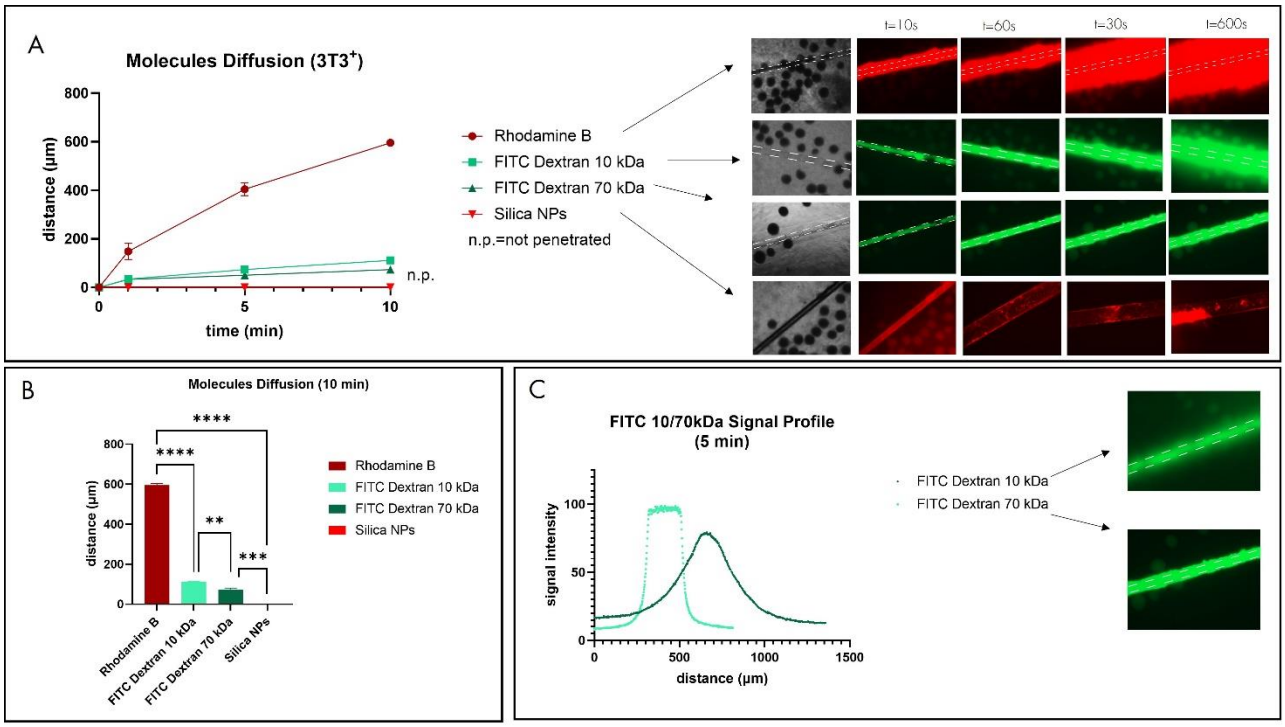

FIG. 29 COMPARISON OF MOLECULES TRANSPORT WITHIN THE BCM [H5V+; 4T1+; 3T3+] OVER TIME; A) Diffusion rates of Rhodamine B (ca.1-2 nm), FITC Dextran 10 kDa (3 - 5 nm), FITC Dextran 70 kDa (6 -14 nm); and Silica NPs (100 nm). Size of FITC-Dextran 10/70 kDa are reported according to the hydrodynamic radius. On the right side, bright field and fluorescence microscopy (magnification 4x) of each condition respectively at t=10, 60, 300, and 600 s. For Silica NPs no extravasation and penetration were observed. B) Molecules diffusion at t=10 min, data represents mean ± SEM for at least 3 independent experiments. *p < 0.05, **p < 0.01, ***p < 0.001, ****p < 0.0001; C) Comparison of signal profiles for FITC Dextran 10 kDa and 70 kDa at 5 min show different trends in diffusion pattern.

5.6 MBs-MEDIATED SONOPORATION

As the final step of this research project, the BCM was employed as a biologically relevant 3D in vitro model for acoustical applications in which both the physical effects on MBs and the mechanobiological responses on biological tissues upon exposure to the US field can be observed. In particular, the employed model constituted by the BCM, and an appropriate holding mould were, from the beginning, designed and optimized in view of their applicability not only in biological but also in acoustical set-ups.

The results related to the accomplishment of the research goal are reported below. In this case, cell-free hydrogel and BCM (-) were employed as investigation platforms in which the effects of MBs-US on the endothelial barrier and on the consequent increase of FITC Dextran 10 kDa were evaluated. The analysis is a proof of concept for the purposes of enhanced extravasation and diffusion of large molecules through the main drug diffusion barriers by means of MBs-mediated sonoporation.

5.6.1 BCM suitability for MBs-US investigations

5.6.1.1 Hydrogel perfusion and MBs cavitation

After guaranteeing the acoustical and optical transparency of the GelMA/Matrigel cell-free hydrogel, it followed the adaptability and optimization of the model design to the optical set-up in terms of model perfusion and alignment of US and camera, as described above in the methods section. Once that MBs were successfully perfused and observed in the channel of cell-free hydrogel, different pressure in the range of 100 kPa-5MPa were applied to assess whether MBs were responding, and thus to check the alignment of the US transducer, and the extent of MBs response upon acoustic field. As shown in Fig. 30, MBs within cell-free hydrogel reacted to the external US field with volumetric oscillations, allowing the observation of both linear, nonlinear, and inertial regimens. In this specific case, for pressure of 100 kPa we could indeed observe spherical oscillations. The spherical oscillations of MBs, however, was gradually lost with the increase of the acoustic pressure, yet observable at 800 kPa -1MPa in which MBs are subjected to nonlinear deformation while oscillating. The linear and nonlinear regimens are defined as stable cavitation in which the MBs echoes contains not only their fundamental driving frequency but, eventually, also harmonics and subharmonics. When acoustic pressure exceeds, in this case 5MPa, MBs behaviour becomes chaotic and oscillation amplitudes can be that large to lead to violent inertial collapse and thus to MBs fragmentation.
Nevertheless, how specified above, acoustic pressure is not the only parameter affecting the extent of MBs volumetric oscillations. The incidence wave in fact, should match the resonance frequency of MBs, defined according to their size, to obtain the maximum excursion of bubble. This is important for therapeutic applications as it has been observed that tissue sonoporation with the opening of endothelial junctions, occurred when the excursion amplitude of MBs exceeds 0.7 μm [89].

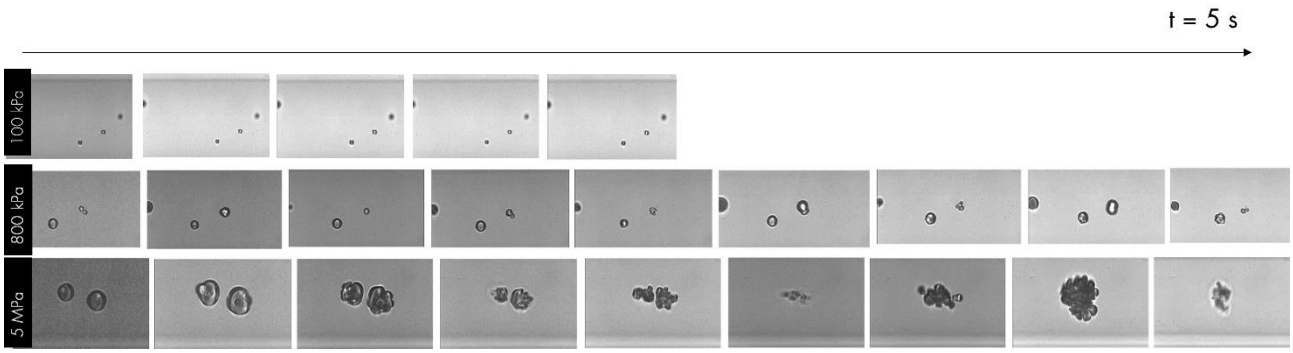

FIG. 30 MBs CAVITATING UPON EXPOSURE OF US WITH DIFFERENT PRESSURE IN CONDITION OF FLOW (10 µl/min); (From the top raw) MBs (whose original diameter is ca. 6 µm) show very low volumetric amplitudes upon exposure of an acoustic pressure of 100 kPa; For higher acoustic pressures the MBs oscillations are subjected to mild deformations towards non-spherical oscillations. In the bottom row, the effect of excessive acoustic pressures (in this case 5 MPa) leads to violent volumetric oscillations which lead to MBs fragmentations. In this inertial range, the attractive effects among nearby MBs due to radiation forces is also clearly visible.

5.6.1.2 MBs cavitation within the endothelialized channel

Successively, the endothelialized channel of the hydrogel was clearly observed under the acoustical set-up as shown below, confirming the optical appropriateness of the hydrogel. Furthermore, a high concentration of MBs was injected and perfused into the channel with a perfusion rate of 10 µl/min, as shown in Fig. 31 B. When the flow was interrupted, MBs were stuck in between endothelial cells present in the confluent channel as shown in Fig. 31 C, D. Frames of the inner endothelialized channel before and after the US (0,3 MHz, 10 mV) are shown below (). The employment of the ultra-high-speed camera allowed the observation of MBs aggregation upon US exposure, likely due to radiation forces that are established when MBs in proximity oscillate in phase and undergo attractive force leading to MBs coalescence. To show the tissue damage due to harmful cavitation, we intentionally applied the US field for repeated cycles. As expected, compared to the starting situation (Fig. 31A), we could observe significant intermediate and complete endothelial walls damage and cell detachment, as shown in Fig. respectively.

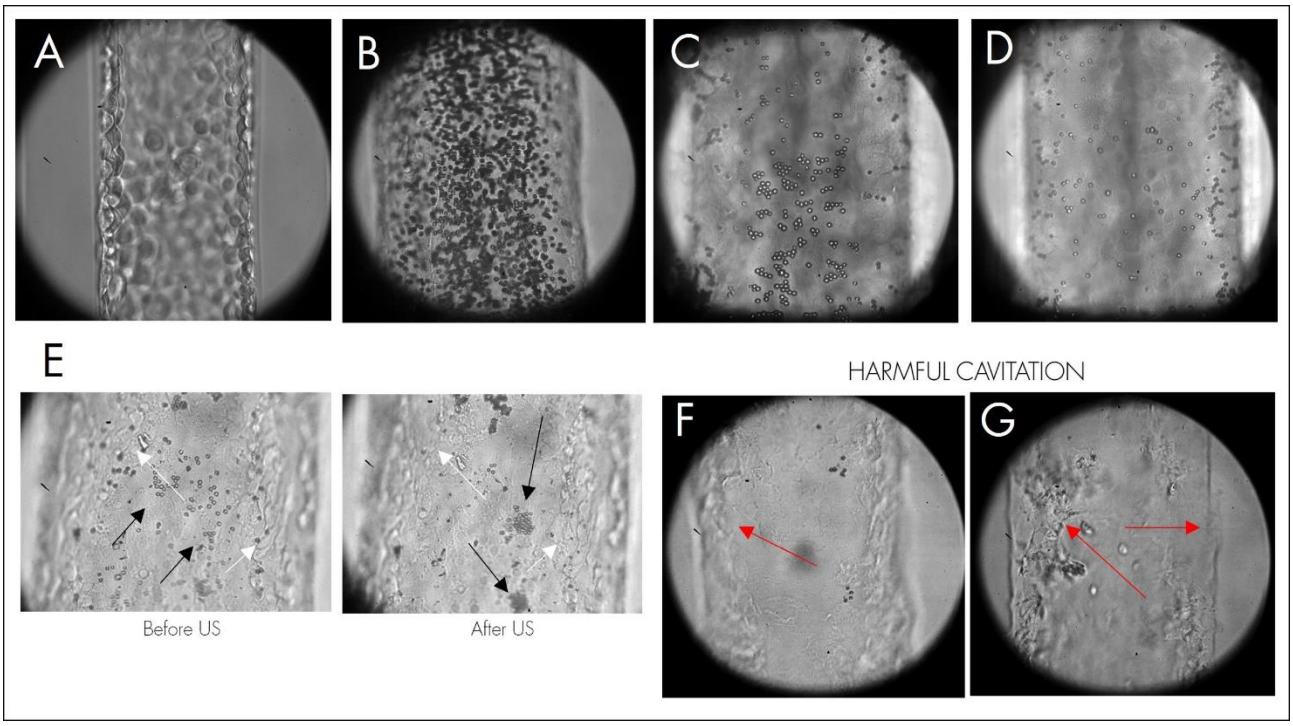

FIG. 31 MBs CAVITATION INTO THE ENDOTHELIAZED CHANNEL; A) The optical transparency of the BCM[1] allows the sharp visualization of the endothelial barrier walls; B) MBs in a very high concentrations were perfused into the endothelialized channel by means of a syringe pump (10 µl/ml); C) - D) By focusing the camera on the bottom layer of the channel, it is possible to observe MBs stuck in between of endothelial cells after perfusion (no flow present). The two pictures show two different focuses of the channel (bottom is on focus in C while in D the focused in on the vessel walls); E) Frames captured prior and post the application of US show the presence of endothelial cells (white arrows) and the coalescence of MBs after US applications (black arrows). The channel results in intact in both cases; F) – G) Show, instead, different extent of cellular damage upon repeated US applications. Starting from an initial situation of perfectly endothelium, it is possible to induce different degrees of endothelium and vessel wall disruption (the second visible on the right wall in Fig. G) via harmful cavitation regimens.

5.6.1 MBS CAVITATION WITHIN THE BCM

The proposed tri-culture BCM model characterized by a relatively dense stroma resulted in suitable for investigations of MBs-US applications. As shown below in Fig. 32A, the visualization of the endothelialized channel was still possible although it was not as well-defined as in BCM[1] models due to the presence of the fibroblastic stroma, indicated in the picture. Following the injection of MBs in higher or lower concentrations (Fig.32), the use of an ultra-high-speed camera allowed the observation of the aggregation of a relatively high concentrated population of MBs when exposed to a US field (2MHz, 20mV) (Fig. 32 I).

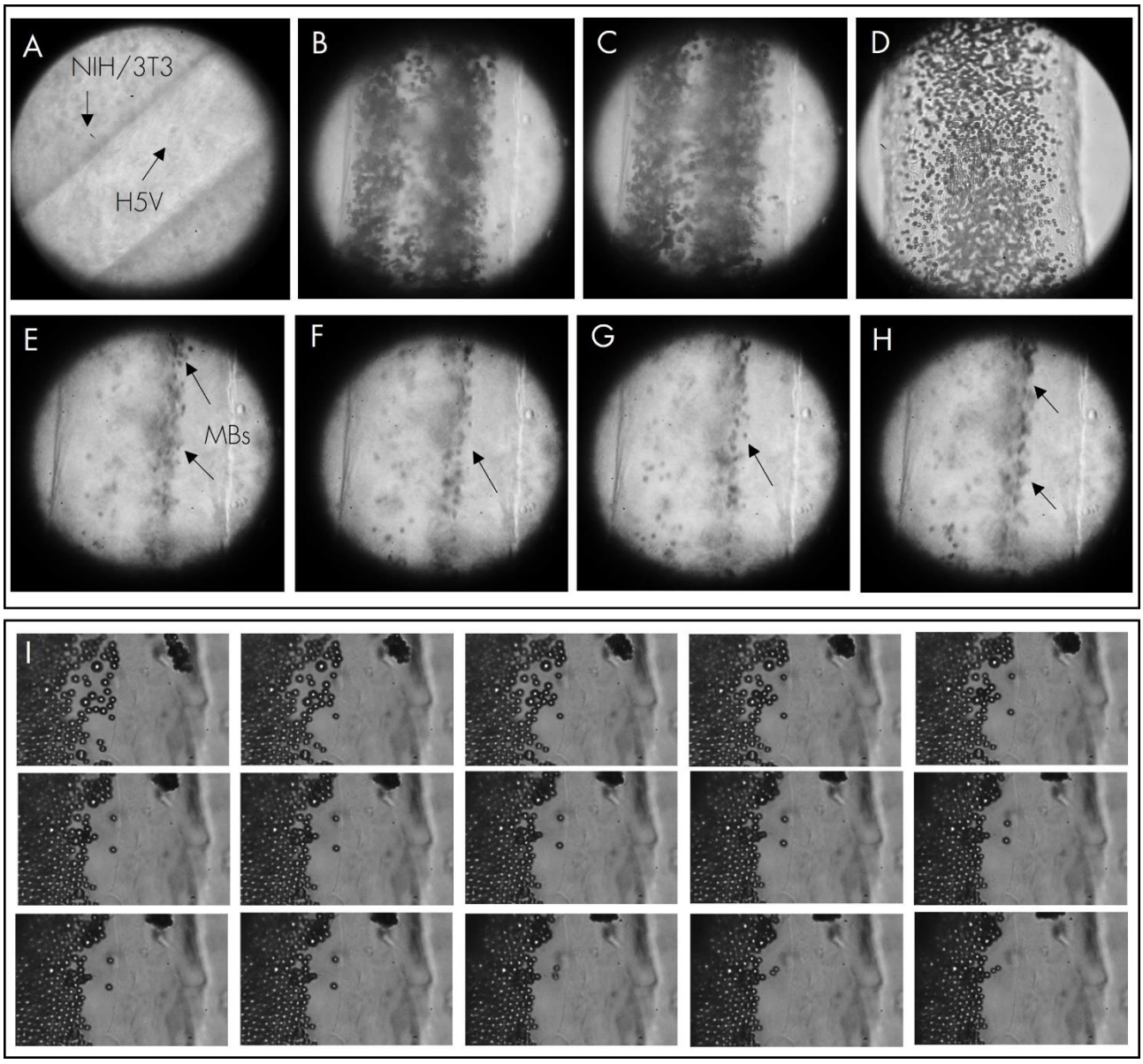

FIG. 32 MBs WERE PERFUSED INTO THE BCM CONTAINING THE FIBROBLASTIC STROMA AND US WAS APPLIED. A) The optical clarity of the hydrogel and the layering-based BCM assembly ensure the observation of the channel even in the presence of $4x10^6$ cells/ml 3T3 fibroblasts albeit vessel walls are less sharp compared to the $BCM^{(-)}$; The sequence B)-H) show the $BCM^{(+)}$ channels perfused with different confenctration of MBs. Even in the presence of fibroblasts, it is still possible to observe MBs within the channel (200 μm). I) By means of ultra-high-speed-camera, it is possible to observe a population of MBs clustering upon US exposure even in condition of surrounding stroma.

5.7 MBS-US -MEDIATED ENHANCED MOLECULES TRANSPORT

5.7.1 Effects of MBs-mediated sonoporation on cell-free hydrogel

Permeability assay with FITC Dextran 10 kDa was performed once again in a cell-free hydrogel under the acoustical set-up. The rationale behind the use of a cell-free hydrogel as the first step is whether to have a control condition in the new setup, similar to the transport assay performed in the biological set-up and, to evaluate the feasibility and objective readouts of experiments priorly to the employment of the BCM in this

set-up. A time window of 10 min was considered for perfusion of FITC Dextran 10 kDa with and without the application of the US field. Time-lapse fluorescence images were collected and both, diffusion distance and signal intensity at 0, 2, 4, 6,8,10, and 12 mins time points were assessed by means of a self-generated Python script (Fig.33 A). Such code yielded a summarized dataset in a 2D heat map for each performed experiment (Fig.33 B). By overlapping the bright field microscopy and the time-lapse fluorescence images it was possible to delineate the diffusion distance from the channel over time (similarly to the previous transport experiments performed in the biological set-up by means of EVOS). Therefore, the 2D graphs reported below in Fig. 33 C, summarize the trends of diffusion rates against distance from the channel at the different time points (up to 12 minutes) reported on the left axis. The colour of the maps indicates the signal intensity for a semi-quantitative evaluation. Although the differences in diffusion rates can be appreciated from these heat maps by looking at the signal intensity profiles, other quantitative readouts are required for the interpretation of the results. In Fig 33. C, the approximate quantitative analysis of FITC Dextran 10 kDa diffusion distance in the cell-free hydrogel is reported. These curves were obtained by measuring on ImageJ the distance from the channel wall to the profile defined by the colour corresponding to the signal intensity value equal to 0.5 (light blue). The mean values of the triplicates relative to the two conditions, with and without MBs-US, are reported in the curves. Of these, the statistical significance at each time points. As hypothesized, the diffusion rate of FITC Dextran 10kDa in cell-free hydrogels is significantly higher in those samples in which MBs were exposed to US compared to those in which no treatment was applied. The statistical significance is verified for the first 6 minutes over the 12 min window.

The lower definition of the signal due to the fluorescent filter microscope in the acoustical set-up led us to generate a Python script able to objectively extract the signal intensity over diffusion distance. Although we cannot directly compare the readouts of this experiment with those of the molecules' transport application because of the different experimental and microscope setups, the results between the two applications were consistent. Even in this case, the presence of the endothelial barrier (without MBs-US) attenuates the diffusion rate of FITC Dextran 10 kDa by37,94% compared to the cell-free hydrogel. In the case of applied MBs-US, an increase of 36,85% and 38,42% in cell-free and BCM$^{(-)}$ models respectively were recorded upon US exposure.

5.7.2 Effect of MBs-mediated US on the endothelial barrier

Analogously to what was done before for cell-free hydrogel, the enhanced permeability mediated by MBs-US was assessed also in BCM$^{(-)}$ models to evaluate the effect of MBs-US on the endothelial barrier (Fig. 34). Even in this case, timeframes of three independent replicates per condition were analyzed by means of the script to generate summary heat maps of the diffusion rate and signal intensity over time. Diffusion distances were measured on ImageJ and mean values were used to draw the two approximate curves. On the basis of the enhanced signal intensity for longer diffusion distances, we can claim that, even in this case, upon activation of the focused US beam, MBs response within the BCM$^{(-)}$ generated an increase in FITC Dextran 10 kDa transport within the tissue. Therefore, limitations diffusion due to the endothelium were attenuated thanks to the MBs-US treatment.

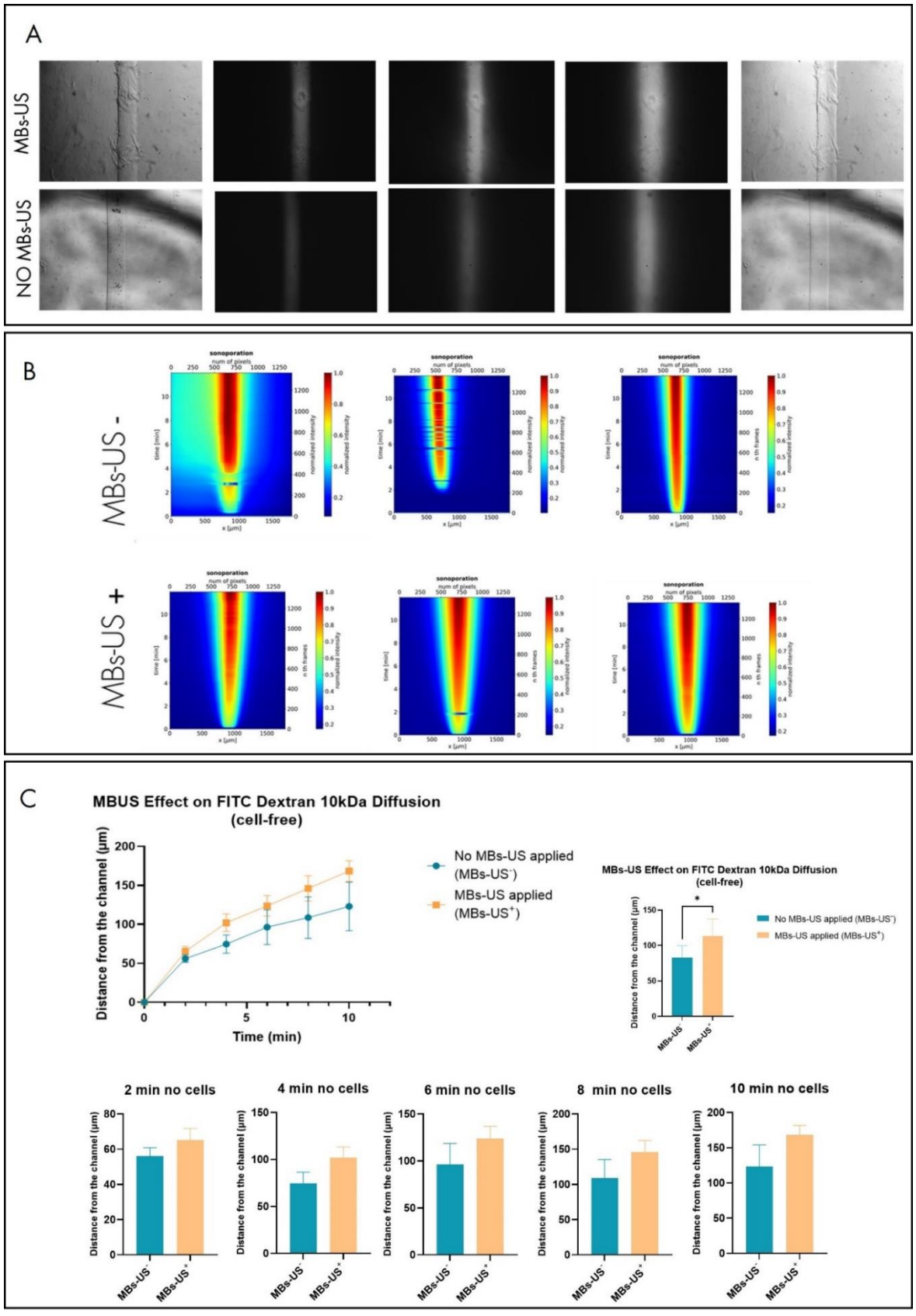

FIG. 33 EFFECT OF MBS-US ON FITC DEXTRAN 10 KDA DIFFUSION IN CELL-FREE HYDROGEL OVER 10 MIN TREATMENT A) Bright field and fluorescence microscopy (5x) frames analysed by the Python script to returned the heat maps of signal intensity over distance (shown in B); Heat maps were then analyzed via ImageJ; Results of the analysis are shown in C) Upon MBs-US there is enhanced, but not significant, extravasation and diffusion rates of FITC Dextran 10 kDa upon the exposure to US over 10 min treatment. Data represents mean ± SEM for at least 3 independent experiments. *$p < 0.05$, **$p < 0.01$, ***$p < 0.001$, ****$p < 0.0001$;

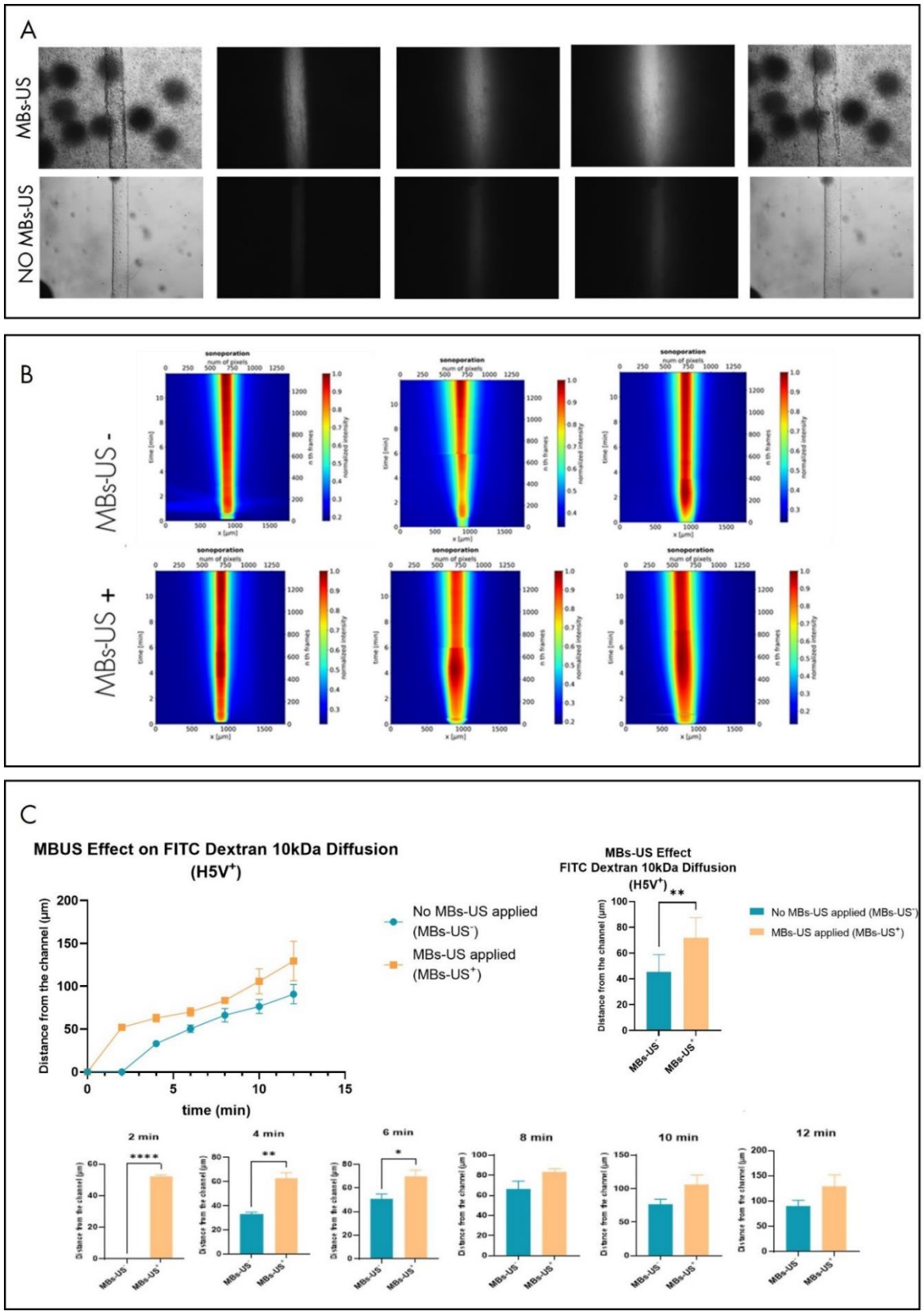

FIG. 34 EFFECT OF MBS-US ON FITC DEXTRAN 10 KDA DIFFUSION IN BCM(-) MODEL OVER 10 MIN TREATMENT A) Bright field and fluorescence microscopy (5x) frames analysed by the Python script to returned the heat maps of signal intensity over distance (shown in B); Heat maps were then analyzed via ImageJ; Results of the analysis are shown in C) Upon MBs-US there is enhanced extravasation and diffusion rates of FITC Dextran 10 kDa upon the exposure to US over 10 min treatment. Statistical significance is shown in the first 6 min of treatments. Data represents mean ± SEM for at least 3 independent experiments. *p < 0.05, **p < 0.01, ***p < 0.001, ****p < 0.0001;

The comparison among the datasets of the four conditions checked in the table below is shown in Fig.35. In particular, the consistency between the results obtained in this last phase of MBs-US-mediated enhanced diffusion and the results obtained when the effect of biological barriers on different molecules transport was assessed, was checked. As shown in Fig. 35A, in conditions of no treatment (MBs-US-), FITC Dextran 10 kDa diffusion rate was higher in the cell-free hydrogel than in the endothelialized tissue. The lack of treatment and the presence of the endothelial barrier conferred the lowest diffusion rate. As expected, the highest diffusion rate was observed in cell-free hydrogel treated with MBs-US where. Interestingly but not completely unexpected, instead, is the lower diffusion rate of treated endothelialized samples compared to the diffusion profile of non-treated cell-free hydrogels.

EFFECT OF SONOPORATION ON PHYSICAL BARRIER

	Cell-free	Endothelial (3T3-)	Stroma (3T3+)
NO MBUS	◆	◆	
WITH MBUS	◆	◆	

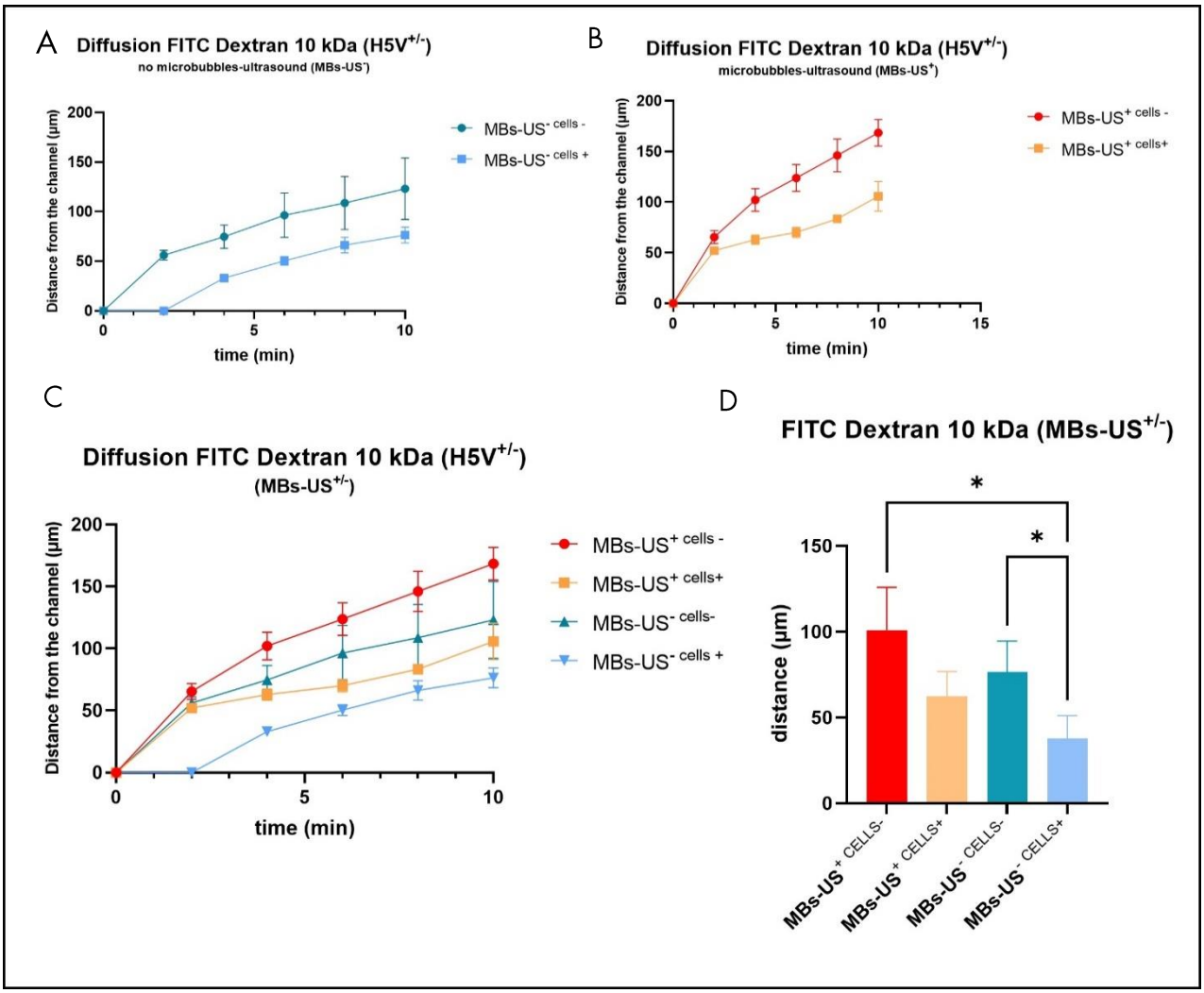

FIG. 35 OVERALL COMPARISON OF MBs-US OR NO TREATMENT EFFECTS ON THE TWO CONDITIONS, CELL-FREE HYDROGEL WALLS AND ENDOTHELIAL WALLS, DERIVING FROM THE TWO PREVIOUS SINGULAR ANALYSIS. **A)** Comparison of no treatment on the two different conditions (cell-free and BCM $^{(-)}$) ; **B)** Comparison of treatment on the two different conditions (cell-free and BCM $^{(-)}$) ; **C)** Comparison of all conditions: with and without treatment on the two different conditions (cell-free and BCM $^{(-)}$) ; **D)** Data show the mean value for each condition and the statistical significance obtained via one-way ANOVA and multiple comparison; * $p < 0.05$

6. DISCUSSION

In the last decade, the employment of therapeutic MBs-US has shown promising results even in more adverse pathological conditions characterized by impenetrable biological barriers such as the blood-brain barrier as well as cancer-associated endothelium and dense stroma. Animal models are currently the most employed investigation platforms as they enable the optimization of acoustical parameters for achieving the optimal dose/efficacy ratio in *in vivo* situations, allowing, in case, an estimation of potential side effects. Their use, however, is limited to microscopy-based techniques/lack of optical clarity, and real-time measurements. *In vitro* microfluidic platforms are valid tools that can obviate some of these issues by simulating simple or complex biological environments in which pathophysiological conditions can be induced and therapeutic techniques can be studied. Nevertheless, the development of a 3D model which includes biological relevance while ensuring acoustical and optical requirements is challenging.

In this multidisciplinary project a relatively complex 3D *in vitro* breast cancer microtissue (BCM) suitable for both, molecules diffusion studies and MBs-US applications, was successfully developed, characterized, and used as an assessment tool.

According to biological, optical, and acoustical design requirements, we successfully developed a stable, optically, and acoustically clear 3D GelMA/Matrigel-based scaffold with significant thickness and perfusable channel(s) able to sustain long-term tricultures. By means of qPCR and, possibly, immunohistochemistry, the BCM model show tendencies towards an invasive and tumorigenic phenotype via downregulation of E-Cadherin over upregulation of Mmp-9, furtherly confirmed by mesenchymal markers such as Fibronectin, and vimentin. The BCM also recapitulated the involvement of 3T3 in matrix stiffening, when compared to the cell-free hydrogel, although the fast degradation of the hydrogel caused a decrease in compressive modulus over time. By perfusing the BCM with Rhodamine B, FITC Dextran (10 and 20 kDa), and silica NPs we were able to mimic the effect of biological barriers upon molecules diffusion. Notably, we showed the limited molecules' diffusion rate and concentration upon the increased molecular size of the tracer. Furthermore, we showed that the extent of the impediment of the stromal barrier versus the endothelial is more accentuated on large molecules (FITC Dextran 10 kDa) rather than Rhodamine B. Finally, we showed the suitability of the BCM model for the study of cavitating MBs upon US exposure and their potential damage on the endothelial layer. Furthermore, the beneficial effects of MBs-US on molecule transport across biological barriers were successfully reproduced and confirmed in the BCM via the enhancement of FITC Dextran 10 kDa transepithelial transport upon treatment.
In conclusion, the BCM model is a versatile investigation platform that lends itself for studies molecules transport mediated by MBs-US and for offering insights on MBs-cell interactions.

6.1 GELMA/MATRIGEL-BASED HYDROGELS AS SUITABLE SCAFFOLDS FOR THE BREAST CANCER-LIKE 3D MICROTISSUE CULTURE

The proposed GelMA/Matrigel hydrogels offer simple, robust, and mechanical tunable systems to develop significantly sized scaffolds able to integrate multiple cell lines and to ensure their viability for relatively long culture times (at least 14 days). GelMA, which constitutes 95% of the hydrogel, owns relevant biological and mechanical properties easily tunable via modification of GelMA and PI concentrations, degree of methacrylation, and polymerization protocol [102]. Besides this, in this project, the choice of GelMA-based hydrogels was also driven by their complete optical transparency especially if compared to collagen hydrogels, widely employed as breast cancer *in vitro* models. Although collagen hydrogels show better biocompatibility and closer resemblance with the *in vivo* breast tumor ECM, they lack appropriate mechanical stability for recapitulating samples with relevant hierarchical cellular architecture, and, in this case, adequate size and thickness to fit acoustical set up requirements (Supplementary material, 1S) [97]. GelMA, however, is anyway made of gelatin which is an irreversibly hydrolysed form of collagen type I, thus they have similar properties [110]. Furthermore, cell-compatibility of GelMA with a several cell types, among which NIH/3T3 fibroblasts, was shown for in vitro configurations [111]. To properly recapitulate a more complex ECM and to confer higher biocompatibility to the proposed hydrogel, Matrigel was added in a very small percentage (5% v/v). Matrigel is broadly used in models aimed at mimicking breast cancer drug resistance since, as reconstituted basement membrane, it contains most of the breast ECM molecules such as collagen IV, laminin, and proteoglycans [112 99 113].

By means of SEM images and of hydrogel size measurements we could describe GelMA/Matrigel hydrogel physical properties. Being the hydrogel mostly composed by GelMA and just to a minor extent by Matrigel, the overall morphology resembles more that one of pure GelMA hydrogels than Matrigel's [114 115]. Notably, GelMA-based hydrogels own a physical porous structure highly dependent and tunable on photopolymerization conditions, GelMA and PI concentrations, and degree of methacrylation.

GelMA/Matrigel hydrogel samples for SEM were lyophilized after being stored at 37°C for one day and thus SEM pictures show the morphology of hydrogel after their syneresis following incubation (37°C) and lyophilization process. The microporous network of the hydrogel, thus, is the result of the phase separation induced by hydrogel photopolymerization. In other terms, when hydrogel polymerization occurs with a higher amount of water than that there would be at equilibrium swelling, syneresis occurs, namely the expulsion of water from the gel. In this regard, it should be pointed out that GelMA and Matrigel cure at opposite temperatures, 4°C and 37°C degrees respectively. Therefore, the high-water expulsion observed in the hydrogel upon incubation time can be due to the local excess of water which is squeezed out of the curing polymer to reach its equilibrium swelling concentration (thermodynamically favoured state).

From a visual observation of the SEM pictures, we can notice a very dense and relatively homogeneous network which ensures the structural stability of the construct. On the other hand, still from SEM pictures, we have reason to believe that pores are not interconnected and are cavity-shaped, consistently with pore formation deriving from syneresis-mediated phase separation induced by photopolymerization [116]. The range of optimal pore size for fibroblasts found in literature (5-15 μm) is confirmed in our hydrogel (9,544 ± 0.0876 μm) indicates that cell viability of stromal NIH/3T3 fibroblasts is ensured [117]. It is, however, well consolidated the importance of having, ideally, hydrogels with interconnected pores in bioengineering applications to enable the cellular spreading, migration, and proliferation of encapsulated cells as, in such conditions, cells would receive an adequate supply of nutrients and oxygen while ensuring a proper

metabolic waste diffusion [118] [119] [120]. Although in this project GelMA and PI concentrations were minimized to ensure both mechanical stability of the thick construct and cell viability, the addition of Matrigel (5% v/v) was supposed to increase the formation of larger, or at least interconnected pores, without constraining the cellular spreading while ensuring the mechanical stability of the scaffold.

These considerations were consistent with cell viability assay results. Although the GelMA/Matrigel hydrogel showed to sustain cellular viability of 3T3 and 4T1 monocultures over 10 days, Calcein-AM staining showed differences in cellular spreading according to tissue areas. In other words, given the three dimensionality and the large size of samples analysed (7x7x5 mm), the extent of cellular spreading within the tissue varied according to vicinity with hydrogel surface. The part of tissue more exposed to the outer environment (cell culture medium) showed an increasing cellular spreading over time and was completely covered by a robust matrix of aligned fibroblasts on day 10 of culture. Underlying layers also showed good cell morphology as they were still in proximity of the surface. For very inner tissue areas, however, cells looked alive, but their spreading was not always ensured probably due to the non-interconnectivity of pores which ensured nutrients supply but constrain cells from properly spreading. It is, however, interesting to point out that, in 4T1 3D monoculture, cluster of cancer cells were growing within the hydrogel and, on day 7, significant cellular aggregates were observed. This suggests an environment potentially favourable to cancer cells migrations although the no interconnectivity of the porous network. It is possible that this migratory trend of cancer cells is enhanced by the augmented degradation of the hydrogel matrix over time even if minor trends in clustering were observed already on early stage of cell culture. In supplementary material, Fig.7S , the gene expression of the 3T3 and 4T1 monocultures in 2D and 3D (on day4) are reported. In both cell monocultures, upregulations in gene associated with ECM degradation and with a mesenchymal and metastatic, and thus migratory, phenotype are upregulated (MMP-9, TNF-α, PDGF-β). This can suggest that, although not always visible (at least in fibroblasts), cells show migratory trends confirming the suitability of the hydrogel as scaffold.

To generate a high cellular density milieu, as the one found in breast cancer, fibroblasts cellular density was increased up to 4 x10^6 cells/ml and cell viability and metabolic activity was compared with the lower cellular density (2x10^6 cells/ml) (Supplementary material, Fig. 2S). Differences between the two cellular densities were esteemed with the metabolic activity assay. The considerably lower metabolic activity rate of the high dense tissue was unexpected but later interpreted as a sort of energetic saturation given by the elevated cellular density. Prior studies reveal a reduction of oxygen consumption, net lactate production, F-actin content, and ATP and NAD-content upon increased culture density [121]. For this model, we anyway decided to incorporate the higher cellular density of fibroblast as they can still constitute a biological barrier for molecules transport. Cancer cell monoculture (2x10^6 cells/ml), on the other hand showed a more homogeneous cell viability with a cell spreading characterized by clusters of cells and an overall metabolic activity growth.

When analysing the mechanical properties of hydrogels, usually performed by means of compression testing, it should be kept in mind that soft tissues behave as nonlinear, anisotropic, and nonuniform viscoelastic materials [122]. Despite compression tests are not suitable for yielding information on fracture toughness, we are not interested in hydrogel resistance to tensile strain and tensile strength[123]. Similarly, GelMA and Matrigel themselves are characterized by a high batch-to-batch production process variability which already affects the repeatability and reproducibility and thus the consistency of data. For the aims of this project, these variances however, are not crucial as long as structural stability along with biological and clinical relevance are maintained [124] [125].

To conclude this first hydrogel characterization part, the cell-free GelMA/Matrigel hydrogels were shown to be suitable platforms for 3D (multi-)cellular culture, for the realization of thick and large constructs while maintaining structural stability, channel integrity, and optical clarity. Acoustical clarity, fundamental for following US applications, was verified lately but anyway supposed similar to water, given the nature of hydrogels.

6.2 THE GELMA/MATRIGEL HYDROGEL-BASED BREAST CANCER MICROTISSUE (BCM) SHOWS BIOLOGICAL AND CLINICAL RELEVANCE.

The structural stability of the GelMA/Matrigel hydrogel enabled the realization of several vascular patterns, from the single-channel, to double or triple channels disposed of in parallel or crossed, either aligned on the same plane or on different planes. Furthermore, the embedding of cancer spheroids within a high cellular density matrix following the proposed BCM assembly protocol not only allows the controllability and customization over cellular components disposition within the hydrogel matrix but also the recapitulation of a multitude of multicellular pathophysiological conditions. Bright-field microscopy of the tissue with and without the stromal fibroblastic components yields an idea of the relatively spatiotemporal complexity of the tissue and of the tumor disposition around the channel. It is, however, the immunohistochemical staining done on tissue sections that confirm the relevant architecture, showing the alignment of cancer spheroids to the channel in a tissue thick 4-5 mm. The mechanical characterization of the BCM was conducted on samples composed of fibroblasts and breast cancer homospheroids (in the pathophysiological ratio 5:1) since biomechanical tumorigenic cues that trigger ECM remodeling and desmoplastic phenotype are mostly established between cancer cells and stromal cells (CAFs). Compared to the cell-free hydrogel we could observe some differences in the viscoelastic behaviour although the hypothesis of microtissue stiffening over time typical of desmoplastic reactions was not verified. In particular, cell-laden hydrogels on day 0 showed the highest compressive modulus while samples on day 10 showed the lowest of the cell-laden hydrogel.

Although unforeseen, the results of decreased compressive modulus over cell culture time are consistent with what was reported by Krishnamoorthy et al. In this study, the mechanical effects of 3T3 fibroblasts embedded in GelMA hydrogel in terms of tensile strength and modulus are investigated and, albeit it is the opposite of compression, can provide interpretation insights. The rationale behind the decrease in compressive modulus over ten days of cell culture might be due to crosslinks cleaving mediated by the release of ECM degradation enzymes by fibroblasts. Specifically, they could observe that the extent of NIH/3T3 fibroblasts-induced GelMA degradation was proportional to the incubation time and, most importantly, to increased cellular density which, in turn, implies faster matrix degradation and bigger pores [126]. However, to support this supposition and to better characterize the BCM stroma it could have been interesting the assessment of the enzymatic release which we did not perform. The high compressive modulus of cells fixed on day 0, instead, could be the result of a not complete release of retained water, given the shorter incubation time, along with a compact hydrogel network. Regardless of cell culture day, cell-laden hydrogels showed a higher, but not significant (apart from day 0), compressive modulus compared to the cell-free hydrogels suggesting the changes at the microstructural levels following breast cancer spheroids and fibroblasts seeding. Notwithstanding, the confirmation of GelMA/Matrigel hydrogel susceptibility to enzymatic degradation was obtained through incubation with collagenase prior to qPCR assay as shown also in the study of Benton et al [116].

Gene expression was assessed on 3D samples of both fibroblasts and breast cancer spheroids monocultures in GelMA/Matrigel, and on 3D samples of co-culture, all on their fourth day. The results of the above discussed mechanical characterization of the cell-laden hydrogels can be confirmed by the results of qPCR, given the presence of matrix metalloproteinase (MMP) enzymes, in particular MMP-9, in the 3D co-culture model stemming from 4T1 cells. MMP-9 enzymes are the main tools used by fibroblasts to shape an invasive tumor milieu through ECM remodelling [127]. As reported in the first section of this report, the loss of ECM integrity mediated by MMPs dysregulates the differentiated state upon loss of junctional integrity and shapes a protumorigenic milieu. Furthermore, a broad body of research claims the tight relation between stable expression of MMP-9 and the consequent loss of E-cadherin, both involved in the EMT toward a more invasive phenotype [128 129]. Strongly associated with MMP-9 upregulation and E-cadherin downregulation there is the upregulation of the angiogenic VEGF which, all together, coordinate breast cancer migration and metastasis [130 131]. In vitro models made of natural polymers, such as GelMA, are often functionalized with VEGF-mimicking peptides since they do not spontaneously display sufficient bioactivity to accelerate angiogenesis and re-epithelialization[132 133]. Interestingly, our 3D co-culture in GelMA/Matrigel show a very moderate expression of VEGF, consistently with the literature, but it is downregulated compared to the NIH/3T3 3D monoculture. It should be kept in mind, however, that CAFs are the principal secretors of MMPs as well as of VEGF so it might be that VEGF is expressed in fibroblast-laden hydrogels[133]. For what concerns E-Cadherin, instead, the final co-culture shows a downregulation compared to the 4T1 spheroids monocultures confirming the occurrence of EMT toward a more aggressive phenotype when 4T1 are in grown with fibroblasts [81]. Moreover, both, 3D monocultures and the 3D co-culture presented sustained values of TNF-α and TGF-β, a profibrotic and a proinflammatory intimately related cytokines which, although their antagonist role in inflammatory and collagen deposition activities, they resulted in co-expressed in breast cancer niche driving exposed tumor cells towards a mesenchymal phenotype as reported by previous studies [134]. In particular, the sustained stimulation of TNF-α with TGF-β, that is the most involved cytokine responsible for the induction of EMT of breast cancer cells, leads to increased tumorigenicity and drug resistance upon activation of NF-κB as well as of p38δ MAPK signaling, inducing tumor growth and metastasis [135 136]. Another evidence of cancer cells undergoing EMT in the co-culture hydrogel is given by the excessive deposition of vimentin and fibronectin (FN) mesenchymal markers, highly present in all the conditions[137]. Mouse metastatic breast tumors are primarily composed of fibronectin in the mammary mesenchymal compartment and it is positively associated with an invasive and metastatic breast cancer phenotype [138]. In line with what was reported by Sugimoto et al., vimentin expression is not specific for fibroblasts in the 4T1 breast cancer model as it is significantly expressed on both 3D 3T3 and 4T1 [139] monocultures. However, in the 3D co-culture vimentin is remarkably upregulated which, as reported by Elisha et al., suggests the detachment from the underlying epithelial layer and the loss of junctional connections among cells implying enhanced invasiveness of the model [140]. Importantly, it has been validated the role of hypoxia, here referred to as expression of HIF-1α, in the increased expression of collagen- and fibronectin-binding integrins. In particular, hypoxia-inducible factor HIF-1α is required for ITGA5 transcriptional activation under hypoxic conditions, which leads to enhanced migration and invasion of single cells within a multicellular 3D tumor spheroid. The upregulated expression of ITGA5, in fact, has been positively associated with increased risk of mortality in metastatic breast cancer patients. Here, the presence of HIF-1α is verified in all the conditions with higher expression in 3D fibroblasts monocultures which indeed yielded the higher contribution to the co-culture. Analogously, albeit to a very minor and almost insignificant extent, ITGA5 expression showed the same trend as HIF-1α consistently with what was observed by Ju et al. [141] . The tumor-associated fibroblasts marker α-SMA was unexpectedly and particularly low expressed in all the conditions but successive transcriptomic analyses of TNBC patients showed congruent results. On the other hand, Pdgfr-β was found relatively highly expressed in the co-culture model,

mainly arising from 3T3 fibroblasts. In breast cancer, PDGF/PDGFR signaling, crucial for EMT and cancer cells migrations, is triggered by TGF-β and promotes the generation of a desmoplastic reaction [142]. Cytokeratin-19 (CK19), also, was very expressed in 4T1 spheroids monoculture, which reflected on the co-culture, and slightly present in fibroblasts, maybe meaning that these fibroblasts were more likely to arise from epithelial cells more than activated fibroblasts.

In regards to ECM remodelling gene expression, it is well confirmed in this 3D co-culture tissue the contribution of fibroblasts as primary aberrant secretion source in ECM Collagen, type 1, α in line with the broad literature [143]. The tumorigenic character of the whole BCM [(+)] was furtherly confirmed by the immunohistochemical staining in which the expression of collagen type 1, vimentin, and ck19 was positively expressed, especially after 14 days of culture, more than what was observed on day 7, suggesting an increase in expression over time culture.

Following this characterization phase, we can thus claim that the GelMA/Matrigel-based hydrogel scaffold constitutes a valid investigation platform inasmuch it allows the recapitulation of organ-specific architecture and displays tumorigenic profiles consistent with the transcriptomic data of TNBC, therefore confirming not only its biological relevance but also the clinical one. Simultaneously to the biological and mechanical characterizations, the cell-free and cell-laden hydrogel showed also suitable optical and acoustical properties in view of successive applications.

6.3 THE VERSATILE BCM MODEL IS SUITABLE FOR IN VITRO STUDIES OF MOLECULES TRANSPORT CONDITIONED BY THE PRESENCE OF DIFFUSION BARRIER AND, POTENTIALLY, ENHANCED BY THE APPLICATION OF MBS-MEDIATED US.

Following characterization of the hydrogel-based microtissue, the BCM model was employed as an investigation in vitro platform for multidisciplinary and interdisciplinary studies related to biological diffusion barriers' implications on molecules transport and their potential overcoming. Results are below discussed.

6.3.1 BCM recapitulates the effect of biological physical barriers, namely endothelium and stroma, on molecules diffusion within the breast cancer microtissue

Scaffolds for 3D cell culture made of biopolymeric hydrogels have been broadly employed in literature to study the effects of molecular gradients-dependent cellular responses as they introduce elements of fluid resistance that prevent convection-based transport mechanisms as observed in tumor milieus due to lack of drainage [144] [145]. As reported above in the first section of this report, molecular gradients in the tumorigenic interstitial space, as well as in this BCM model and in hydrogels in general, are driven by diffusion-based transport due to the EPR effect and thus to the lack of drainage flux [146]. Diffusion is the random movement of molecules that passively tend to move from areas of higher concentration to lower concentration. Therefore, upon gradient establishment, the concentration of the soluble molecules is reduced as an inverse function of the distance from the source.

This statement is consistent with our results. What we could observe is in fact that, for equal tissue conditions (cell-free, with or without fibroblast), Rhodamine B and, to a minor extent, FITC Dextran 10 kDa, quickly established a diffusion gradient upon BCM model perfusion. In particular, Rhodamine B, owing to a smaller size diffused significantly more rapidly due to the steeper concentration gradient between the channel and the farthest tissue areas. FITC Dextran 10 kDa, on the other side, generated less steep concentration gradients and showed a slower diffusion rate given the larger molecular size. Consequently, in BCM(+) models, larger molecules as FITC Dextran 70 kDa (ca.8-15nm) showed a very moderate diffusion rate through the fibroblastic stroma while no penetration into the surrounding stroma was observed for silica NPs (100 nm) which barely showed extravasation. These results are similar to those stated by Cabral et al. after comparing the accumulation and effectiveness of different sizes of drug-loaded polymeric micelles (with diameters ranging between 30 and 100 nm) in poorly permeable human pancreatic cancer models in which just micelles smaller than 50 nm showed penetration [147]. In another study instead, Tang et al. instead, demonstrated that the optimal size of nanocarriers through the various transport compartments varies according to the tissue properties. In other terms, they affirm that nanocarriers in the size range 100-160 nm are optimal for blood circulation but that this size range did not yield any therapeutic benefits for the inability to penetrate the intratumoral tissue for which, instead, nanocarriers of 25 nm might ensure longer penetration distances [148]. The results obtained in our molecule transport study are consistent with the results of Tang et al. in two ways. First, we could observe effective tissue penetration distance for FITC Dextran 10 kDa (ca- 4-5 nm) while FITC Dextran 70 kDa (ca. 15 nm) showed a very attenuated diffusion rate. Second, compared to the smallest Rhodamine B (ca. 1 nm), FITC Dextran 10 kDa experienced different degrees of the impediment in the transendothelial and stromal barriers respectively. Tracers' concentration profiles over space, measured as signal intensities, showed substantial differences in curve trends as Rhodamine B presents a significant plateau due to homogeneously distributed signal while FITC Dextran's signal presents a sharper peak in concomitance of the perfused channel. These observations are in line with previous molecules transport studies found in literature in which diffusion rate, which is determined by the diffusion coefficient has been positively associated with molecules size and the structural properties of the hydrogel-based barrier [149]. The differences in tracer concentrations can be related with molecules retention and optimization of therapeutic dose over time within the tissue on which molecular size has an impact.

These considerations thus suggest that the BCM(+) model is able to recapitulate hinderance of molecule diffusion due to the dense stromal barrier found in the tumor interstitial matrix given by the increased deposition of fibrillar collagen which was shown to hamper penetration of molecules larger than 60 nm into the tumor parenchyma as reported by Ramanujan et al.[150].

When studying molecules transport into biological-like matrices, besides the diffusion rates, it is important to consider also other factors related to internal morphology of such scaffolds. The available value fraction of pores, for example, defined as the accessible space where molecules can pass through, and the tortuosity of the pathway into the hydrogel set the conditions for flow resistance. In the case of cell-free BCM model, average pores size (ca-5-10 um) should have allowed a net diffusion even of FITC Dextran 10 kDa (ca.4-5 nm) but the non-interconnected dense porous network and its tortuosity has given a considerable attenuation in tracer diffusion distance and concentration. In case of cell laden BCM, instead, a certain extent of hydrogel degradation (in this case on day 7), and the affinity of ECM proteins as well as the cellular uptake of the diffused molecules should be considered [151].

Normal endothelial layers easily allow the passage of small lipophilic solutes and nonpolar molecules through endothelial cells due to their high solubility in the cell membrane as in the case of oxygen or, in this case, of Rhodamine B. FITC Dextran, instead, has a hydrophilic nature and thus can cross the endothelial barrier through gaps in the endothelium. Tumor-associated vessels, however, distinguish from normal

vasculature as they have an increased permeability due to endothelial dysregulation towards tumorigenic events. Therefore, endothelial cells of tumor vasculature proliferate faster but form looser gap junctions. Across tumor endothelium, in fact, the large solutes can pass through undisturbed although their penetration into the stroma is subjected to consistent flow resistance due to solid stress and IFP of the tumor milieu [152]. The BCM model, on the other hand, presents a highly confluent endothelial layer whose permeability has been only characterized via molecule transport showing consistent results to literature as mentioned before. Despite it is possible to observe the effect of molecules size and biological barriers on transport, a major characterization of endothelial protein expression such as claudins, occluding, or VE-cadherin, however, is required for being able to compare the BCM endothelium tightness with those found in tumors and the following transport type [153].

These perfusion assays can provide us just a semi-quantitative evaluation of the effects of biological barriers on different-sized molecules diffusion but show that the model could lend itself to more quantitative analysis via permeability assays and/or transepithelial electrical measurement. This would allow a better prediction of drug active or passive absorption or provide more objective information on endothelial barrier integrity respectively [154]. Permeability assays, which is independent from the size- and charge-based selectivity of endothelial tight junctions, could provide quantification of tracer diffusion specifically to cell culture as:

$$Apparent\ Permeability \quad [\mathrm{cm/s}] \qquad Papp = \frac{dQ}{dt}\frac{1}{AC_0}$$

Where dQ/dt is the steady state flux [μmol/s] (which takes place at constant rates);

A is the cell culture area [cm^{-1}]

C_0 initial concentration of tracer

Having said that, although more characterization of stromal and endothelial barriers are necessary, the $BCM^{(+)/(-)}$ model has the foundations to offer a solid and valid investigation platform with organ-like architecture through which could be assessed many quantitative or qualitative aspects of molecular transport across diffusion barriers.

6.3.2 BCM enables the observation of US effects, as the dynamic of MBs cavitation in a confined viscoelastic and tumor-like environment, and the enhanced permeability to molecules diffusion upon exposure to US when MBs are in the channel.

When designing biological in vitro models for ultrasonic applications, several requirements should be considered. So far both the biological aspect of the $BCM^{(+)/(-)}$ in terms of adequacy to display elevated enduring (multi-)cellular density culture and its biological and clinical relevance have been broadly discussed and confirmed. Since the initial phase of model development, however, the choice of the hydrogel matrix was dictated also by the requirements arising from acoustical setups.

The proposed configuration of the BCM model boasts a series of biological complexities and acoustical transparency which, to the best of our knowledge, were never combined before in microfluidic models for ultrasonic applications. As far as we know, current in vitro models employed in therapeutic MBs-US investigations, recapitulate a very simplistic biological environment aimed at single-MB single-cell

interactions observations. Nevertheless, to gain a broader understanding of the underlying biophysical mechanisms and to optimize acoustical therapeutic parameters, a more tumor milieu-like environment should be implemented.

The BCM model presented, being made of hydrogel, owns viscoelastic properties and is softer compared to rigid phantoms often used in acoustical setups. This affects the dynamic of MBs and thus the efficacy of in vitro stimulations for drug delivery studies given that, for equal US driving conditions, the presence of a relatively rigid nearby vascular confinement produces damping effects lowering the maximum MBs oscillations compared to those in free space[155].

The complete optical clarity of the cell-free hydrogel and, even if to a minor extent, of the endothelialized BCM(-) model, allowed the observation of MBs inertial and cavitation regimens within the 200 µm channel upon acoustic pressure in the range of 100 kPa-5MPa. Furthermore, by means of an ultra-high-speed camera, we could observe MBs clustering due to acoustic radiation forces, or Bjerkness forces, which can occur at any acoustic pressures, although their result is more appreciable upon higher intensities (as shown in 5MPa frames sequence) and longer acoustic pulses [105].

Besides allowing the monitoring of MBs dynamic in a viscoelastic confined environment, the BCM model was mostly designed as an experimental platform for evaluating the potential enhancement of molecules' transendothelial and intrastromal diffusion upon application of MBs-US.

We were able to assess the benefits on FITC Dextran10 kDa transport mediated by MBs-US into cell-free and endothelialized (BCM(-)) models. In both cases, the application of treatment at the therapeutic pressure of 700 kPa allowed the enhanced extravasation of tracer from the channel compared to the non-treated models. The fact that also cell-free hydrogel showed enhanced FITC Dextran (10 kDa) extravasation and diffusion implies that MBs cavitation upon US has structural aftermath also on the nearby structures. In line with this, Bezer et al. showed how the effect of a single MBs in conditions of acoustic radiation force can reversibly deform soft tissue mimicking materials [156]. In our case, this might imply that under therapeutic acoustical parameters, the whole and repeated radiation force resulting from a population of MBs upon US exposure has an impact on the surrounding ECM-like GelMA/Matrigel hydrogel through local tissue stresses and micron-scale displacements. Such structural effects in the ECM following cavitation-enhanced US propagation into the tissues induce, to a certain extent, variations in cellular mechanotransduction which might results in a temporarily increase of endothelial junctions or cell membrane porosity and thus of the cellular uptake.

According to these results, we can claim that our model is a valid platform to study the enhanced transendothelial transport of FITC Dextran 10 kDa upon MBs-US application. In particular, to objectively assess cavitation-induced interendothelial gap opening and the potential damage of the endothelial barrier it would be appropriate to adopt electrical sensing techniques such as measurements in the increase in the transmembrane current (TMC) or by measuring transendothelial electrical resistance (TEER) [157 158].

For elaborating more objective conclusions about the efficacy of MBs-US enhanced endothelial permeability, the optimal ratio between the MBs concentration (here $1*10^6$ MBs/cells) and the size of the channel (200 µum should be studied to maximize the potential therapeutic effect of cavitation [159 160]. Also, from bright field microscopy, we had reason to suppose that a flow rate of 10 µl /min was ensuring the refuelling of MBs in the channel between one US application and the other (15 s), although this could not be observed during FITC Dextran diffusion due to fluorescence microscopy. Also, the homogeneity of MBs within the channel is arguable as sometimes we could observe MBs flowing along one wall of the channel rather than the other, or a perfectly centred MBs flow. This inequality of MBs distribution into the channel

could be even given by the presence of non-smooth linear vessel walls (due to more confluent endothelial cell layer) or of channel walls damages (due to fishing line friction upon removal) [161].

To conclude, the BCM model offers a 3D in vitro platform that can be used for observing the behaviour of a population of MBs in a viscous fluid surrounded by a viscoelastic matrix, providing more information about inertial and cavitation regimes. Alternatively, the BCM model able to recapitulate the dense environment of breast carcinoma, is suitable for US-based therapeutic investigation. In this view, the BCM model can yield precious insights on improvements of drug kinetics within tumorigenic tissues upon MBs-US-mediated sonoporation. Furthermore, the complexity of the model can be tuned according to investigation requirements. In the case of investigations about MBs-US effects on the permeability of the endothelial barrier, for example, we used stroma-free models.

6.4 LIMITATIONS OF THE MODELS AND OF THE STUDY

In view of alternative applications, some features of the proposed biologically relevant 3D in vitro breast cancer microtissue with relevant thickness and organ-like architecture for US applications can be improved according to the following hints. To the aims of our study, however, the model was best optimized and functionalized, fulfilling all the research goals.

BCM contained in the plastic disposable molds are grown in well-plates completely submerged in a cell-culture medium. By doing so, cells are equally and ideally exposed to nutrients and oxygen, while in dense tumor stroma the supply is highly heterogeneous leading to the establishment of acidic and hypoxic areas which, in turn, trigger protumorigenic signalings and compromise the efficacy of therapeutic compounds.
The remarkable size (15x15x5mm) and the structural stability of the hydrogel can, however, be exploited to embed multiple channels into the tissue reducing the amount of external medium. Then, through an appropriate peristaltic pumps-based perfusion system, we could attempt to recapitulate more accurate culture conditions in which both diffusion nutrients and oxygen gradients are closer to the in vivo situations. Given the pivotal role of the breast cancer desmoplastic stroma in establishing an impenetrable tumor barrier, its reproducibility into the BCM is important for the purposes of molecules transport studies. The degradation rate of the hydrogel matrix, greater than the cellular release of ECM proteins, however, hampers the stiffening of the microtissue yielding inadequate results relative to the stroma-related diffusion impediment. To enhance the deposition rate of ECM proteins in the scaffold, 3T3 can be transfected with a GLI-responsive firefly luciferase reporter (NIH-3T3/GLI-luc). By doing so, the exposure of treated fibroblasts to sonic hedgehog ligand (SHH) induced by HIF-1α deriving from cancer cells stimulates the upregulated deposition of ECM proteins [162 163].

A further limitation in the study is the short observation time of molecules diffusion which did not allow to measure any penetration of NPs into the stroma, usually conducted over at least 48 h time windows.
Albeit the deposition of spheroids above the channel does not necessarily imply vascular damage if a sufficient amount of hydrogel is interposed, this should be avoided. Rarely, it happened that spheroids accidentally deposited on top of the channel when the second layer of solution was poured, compromising the visualization and the integrity of the vessel.

For the rest, the handmade insertion of needles into the plastic mould roughly on at the same high resulted in enabling the correct formation of the channel. Just in a few cases, the channel is shown to be partially unfocused on the same plane meaning that it was not perfectly aligned without any crucial implications for our applications.

Due to the thin walls of disposable plastic mould, the BCM model showed susceptibility to handling during insertion into the acrylic holder of the acoustic set-up as needles were not completely firm, risking the damage of the channel or fluid leakages at the interfaces needle-plastic moles (which yielded signal issues especially in the water tank of the acoustical set-up in which the samples were submerged). Thus, the assembly of these models required extra care. By meticulously creating the holes with a smaller sharp needle (27G) and then precisely inserting the 25G blunt needles this could be obviated. Particular attention should be pointed even to the removal of the fishing line from the hydrogel after photocrosslinking to avoid damage to vessels walls. In general, however, the model shows to be a solid versatile high throughput platform that can be customized according to investigation goals and adapted to different experimental setups.

CONCLUSIONS

In summary, in this research project, a novel 3D in vitro engineered breast cancer microtissue with biological significance and suitability for MBs-US applications was realized, characterized, and used as an investigation platform. Compared to the state of the art of in vitro platforms for MBs-mediated US studies, the BCM model offers a higher level of biological complexity in terms of cellular components involved and of tumorigenic features, which become more accentuated overtime culture. The BCM also owns clinical relevance upon comparison with TNBC patients' transcriptomic. The ability to mimic organ-specific architecture is given by the mechanical stability of the GelMA/Matrigel hydrogel-based scaffold and allows the recapitulation of both the endothelial and dense stromal barriers for molecules transport studies within the breast TME. The BCM model, developed according to optical and acoustical requirements, ensures its application also as an investigation platform for studying MBs cavitation confined in a viscoelastic environment which better mimics the in vivo situation compared to current rigid phantoms employed. The BCM model is thus a versatile tool that can more accurately predict the biophysical and biochemical effects of MBs-US on the surrounding tissues with an estimation of cellular damage.

FOLLOW-UP STUDIES

The novelty of the BCM model offers many hints for future studies. Follow-up studies are certainly addressed to the evaluation of MBs-US effects on molecules diffusion and concentration through the surrounding dense tumor stroma as anticipated in Fig.36. Once that the parameters of an effective MBs-mediated sonoporation

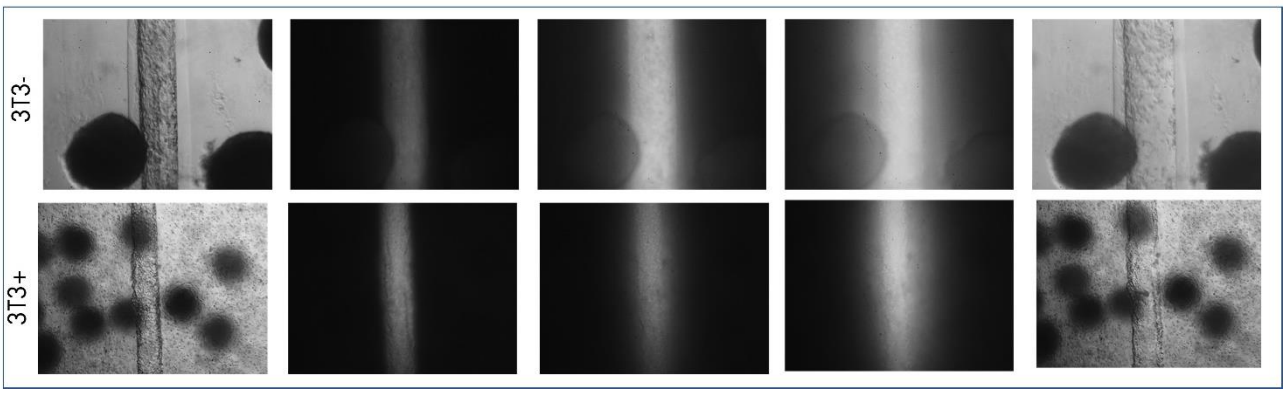

FIG. 36 FOLLOW-UP STUDY: THE EFFECT OF MBS-US ON THE BARRIER CONSTITUTED BY ENDOTHELIUM AND STROMA is shown in the second raw and should be better investigated in order to assess the effective benefits of MBs-US for enhanced drug penetration even through dense barriers such as the desmoplastic breast cancer TME

through the dense stroma are assessed, adequate characterization of treatment benefits should be yielded. The BCM model can be employed to assess the extent of disruption of the plasma membrane and the integrity of ion channels via oscillating MBs. As shown in many MBs-US studies, the influx and outflux of impermeable agents can be evaluated upon propidium iodide uptake and Calcein-AM release respectively. The effect on the cellular membrane alterations could, in the BCM model, be measured even in terms of distance from the vessel to evaluate the extent of the propagation of US waves across the surrounding tissue even when the stimuli are not applied anymore.

Furthermore, for quantitative estimations of the cellular damage either due to US alone or MBs-US cell viability assays should be performed following treatment either through sample sections (possibly a thinner layer containing the channel) and observation of LIVE/DEAD readouts via confocal microscopy or via Annexin V/ PI apoptosis protocol.

As mentioned above, the intratumoral penetration of silica NPs with or without MBs-US treatment would provide striking evidence of the MBs-US efficacy but should be assessed for longer periods in a constrained (closed) vessel to force the side extravasation, potentially recapitulating the obstructed vessel in the TME. Penetration of Silica NPs (100 nm) could be then investigated by sectioning the sample and checking the penetration into the stroma with a fluorescence microscope as shown in **(supplementary material, Fig. 9S)** for shorter perfusion times.

Interestingly, the BCM model characterized by a dense stroma set the bases for being employed for investigations of co-administration of MBs with anti-ECM therapies, such as anti-LOXs, for evaluating the potential further increase in molecules diffusion upon reduction of stromal content following the combinatorial treatment.

After 14 days of culture, the BCM model showed clear signs of angiogenesis via endothelial protrusions as shown in Fig.37. In this view, another interesting application of the BCM model would be that of studying mechanisms of sonoprinting, namely direct deposition of NPs onto endothelial cells walls following cavitation of NPs-loaded MBs. As it was demonstrated that these NPs "patches" remain attached to the cellular membrane for some hours before being internalized, it would be interesting to couple antiangiogenic agents, very debated in breast cancer treatment, on NPs surfaces and evaluate the efficacy via qPCR assays before and after the treatment.

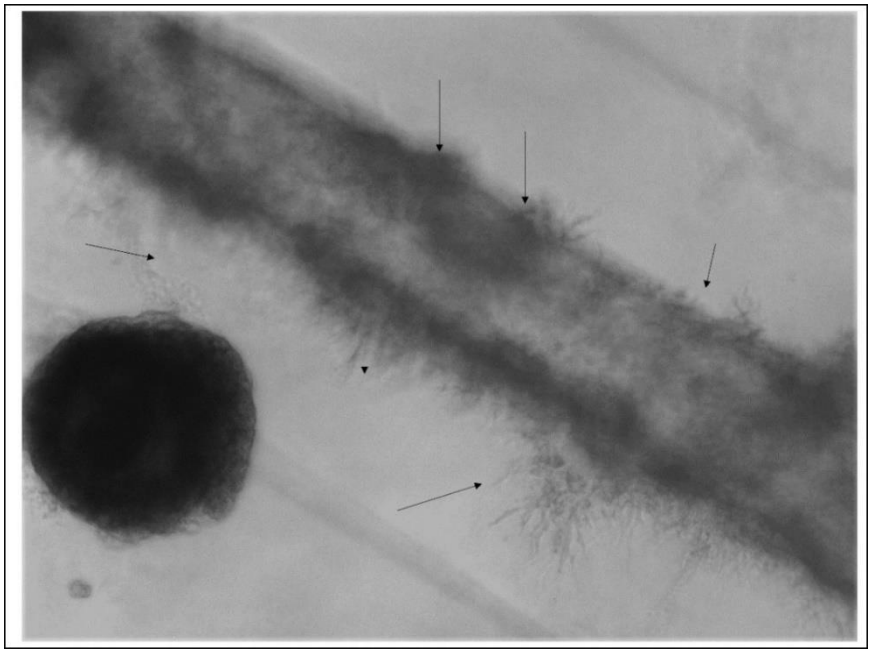

FIG. 37 ANGIOGENIC SPROUTS – H5V ENDOTHELIAL CELLS OBSERVED ON DAY 14 OF BCM(H) CULTURE

Another possible follow-up project could be addressed on investigating the potentially enhanced invasiveness of tumor cells in spheroids located in the proximity of the endothelialized channel. This can offer interesting insights especially if evaluated in function of the endothelial damage due to the MBs-US treatment.

As claimed several times in this report, the BCM shows a high level of versatility which allows the formation of several vascular, and to a minor extent, tumor distribution patterns. This is possible whether thanks to the structural stability of the hydrogel and to the GelMA/Matrigel hydrogel layering-based assembly process. As shown before in the report, parallel or crossed channels could be embedded in the channel. This would yield interesting insights for investigating whether MBs oscillating in nearby or overlapped channels behave differently, of whether they still experience attraction due to radiation forces, and, eventually, if their effects are enhanced.

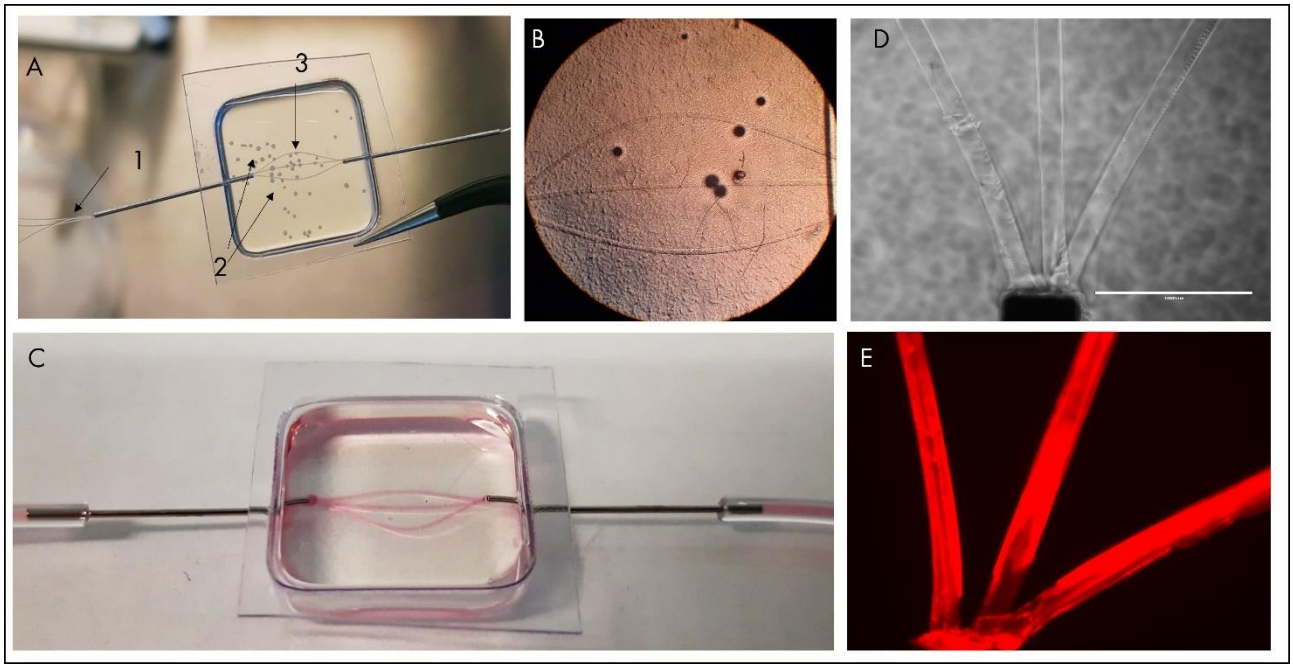

FIG. 38 SHOWS THE POTENTIAL ALTERNATIVE PATTERN OF A TRI-CHANNEL PERFUSED (c) vascular network that can be integrated into the bcm with the same protocol developed before. The difference is given by just using multiple fishing lines; A) shows the hydrogel right after photocrosslinking the bcm with spheroids (indicated by the arrow number 2) and the three fishing (arrow 3 and 1); Of course, this is more a proof of concept of the versatility of the model; b) is a picture that shows the overall integrity of the channels even after removal of the fishing line with minimum dragging. Finally, the new vascialr network was perfuse with food U and silica NPs, Fig. C) and E) respectively. Of course, this design requires optimization.

The complexity of the BCM model can be increased either by integrating a more complex vascular network, as reported in Fig., or by incorporating multiple cells type such as macrophages for which interesting cellular crosstalks could be observed with stromal or tumor cells. Finally, given the suitability of the model to sustain high cellular density mimicking desmoplastic tumors, the BCM could be converted to pancreatic ductal adenocarcinoma (PDAC) model, possibly by using human cells which would increasing the clinical relevance.

In conclusion, our results proved the suitability of the model to molecules transport studies, with the possibility of extrapolating (semi-)quantitative data on the diffusion rate and concentration useful for the investigation of effective therapeutic doses able to trigger a beneficial effect over time. The presence of biological barriers can then be exploited to estimate their overcoming through the application of MBs-US treatments. By closely

observing the direct effects of a population of MBs in the proximity of the endothelium via the employment of ultra-high-speed cameras, as well as the indirect penetrating effect of molecules into the stroma surrounding the channel by means of fluorescent microscopy a multitude of data can be obtained. The use of biological assays, such as qPCR, ELISA, western blot, flow cytometry, permeability, and TEER assays prior and post-treatment, provide further quantitative validations of the MBs-US effectiveness and cellular damage. The BCM model also owns tunable biological features that make it versatile for further applications not only on drug biodistribution but also on the response of different cell types to treatment exposure with the possibility of enhancing the biological complexity and the clinical relevance.

Supplementary material

1. Hydrogel composition study and optimization: GelMA/Collagen hydrogel

In order to investigate the most suitable hydrogel-based scaffold for biological and acoustical applications, a broad hydrogel composition study was conducted. Initial efforts were addressed on the development of a GelMA/collagen hydrogel inasmuch most of the breast cancer in vitro models showed pathobiological relevance when developed in a collagen matrix. GelMA and collagen concentrations and thus ratios of the two components were manipulated in order to obtain reproducible and mechanically stable constructs. In particular, in this research, concentration ranges of 3-5% (w/v) of GelMA and 0.2-0.4% PI (w/v) were tested in combination with 2-3% collagen. Mechanical stability was assessed by visual observation and bright field microscopy (EVOS Cell Imaging System)

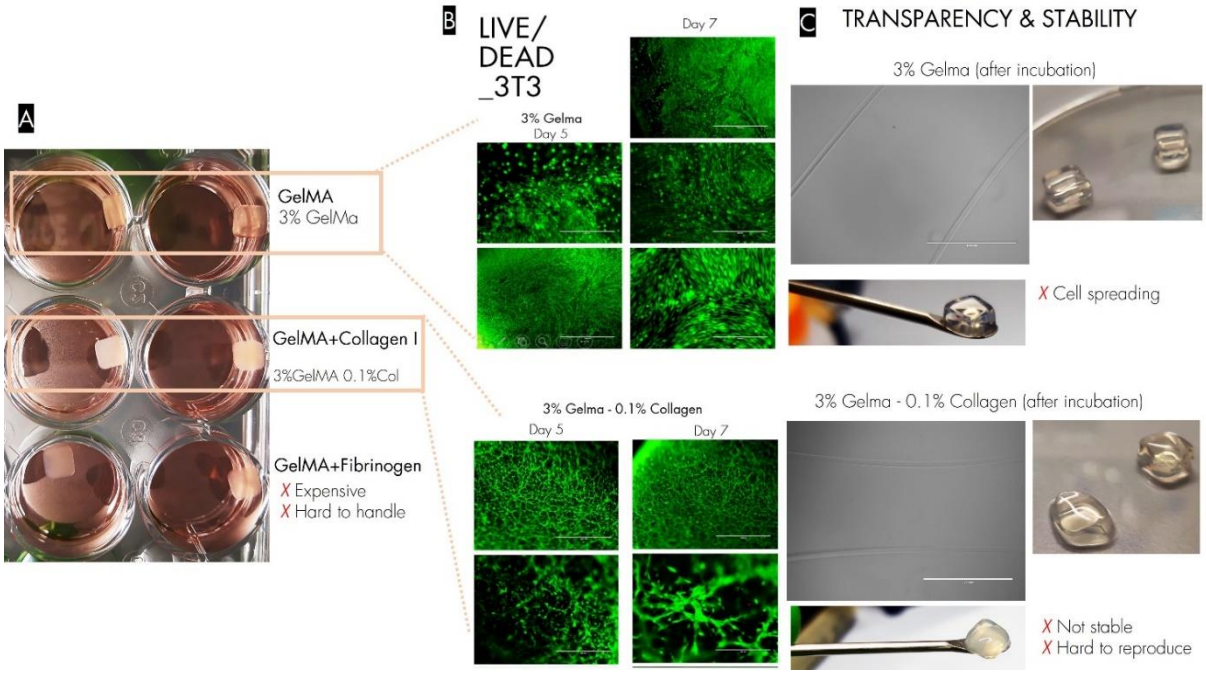

FIG. 1S ATTEMPTS TO DEVELOP HYDROGEL MADE OF COLLAGEN AND GELM; ALTHOUGHT HE GOOD BIOCOMPATIBILITY OF THE HYDROGEL, THE COLLAGEN DID NOT YIELD APPROPRIATE MECHANICAL FRATURES. ALSO, GELMA COLLAGENE CROSSLINK AT OPPPOSITE TEMPERATURE AND THIS HAMPER THE REPROFUCIVILITY OF THE MODEL.

2. Cell Viability of 2*10⁶ cells/ml and 4*10⁶ cells/ml fibroblasts

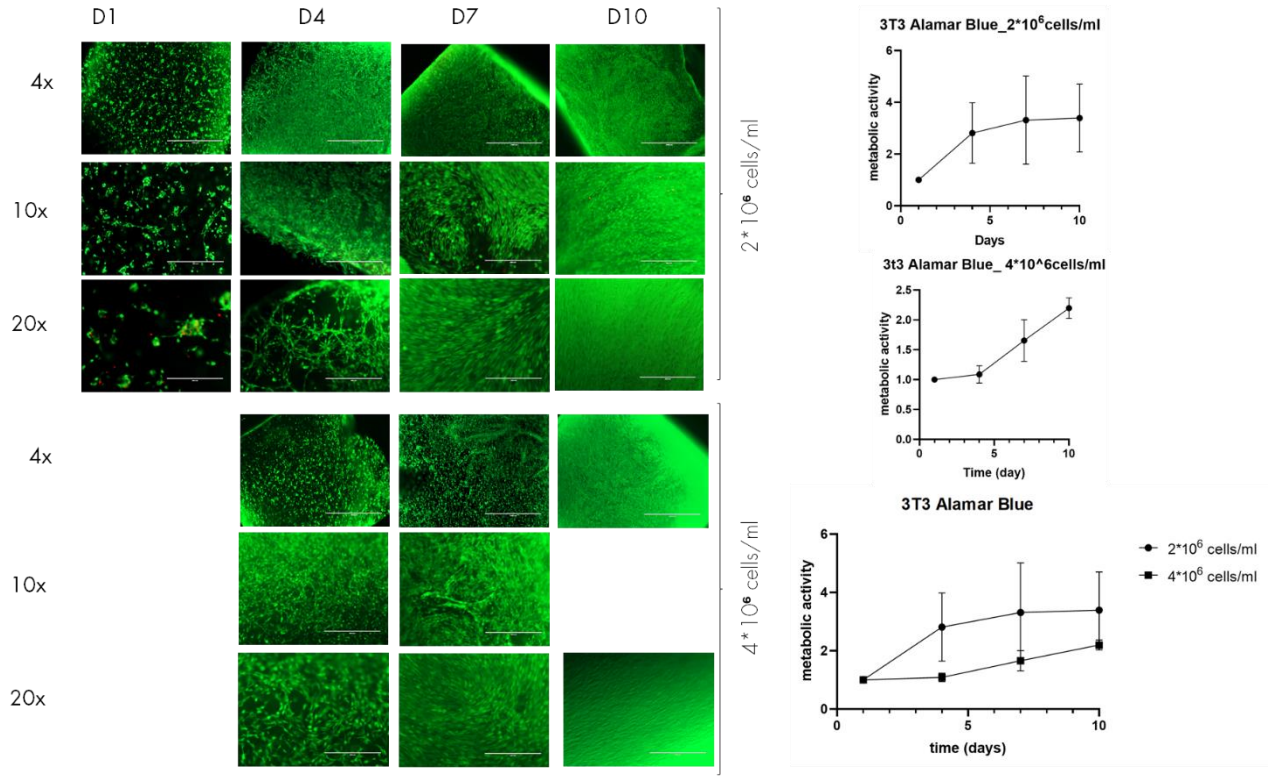

FIG. 2S LIVE/DEAD ASSAYS TO ASSESS THE AFFINITY OG THE HYDROGEL ON BOTH 2 – AND 4-X 10⁶ CELLS/ML FIBROBLASTS. SAME FOR ALAMAR BLU WAS ALSO PERFORMED AND STANDARDIZED ON DAY 0. STILL, NO IMPROVEMENTS IN CELL VIABILITY.

3. Scanning Electron Microscopy: hydrogel morphology

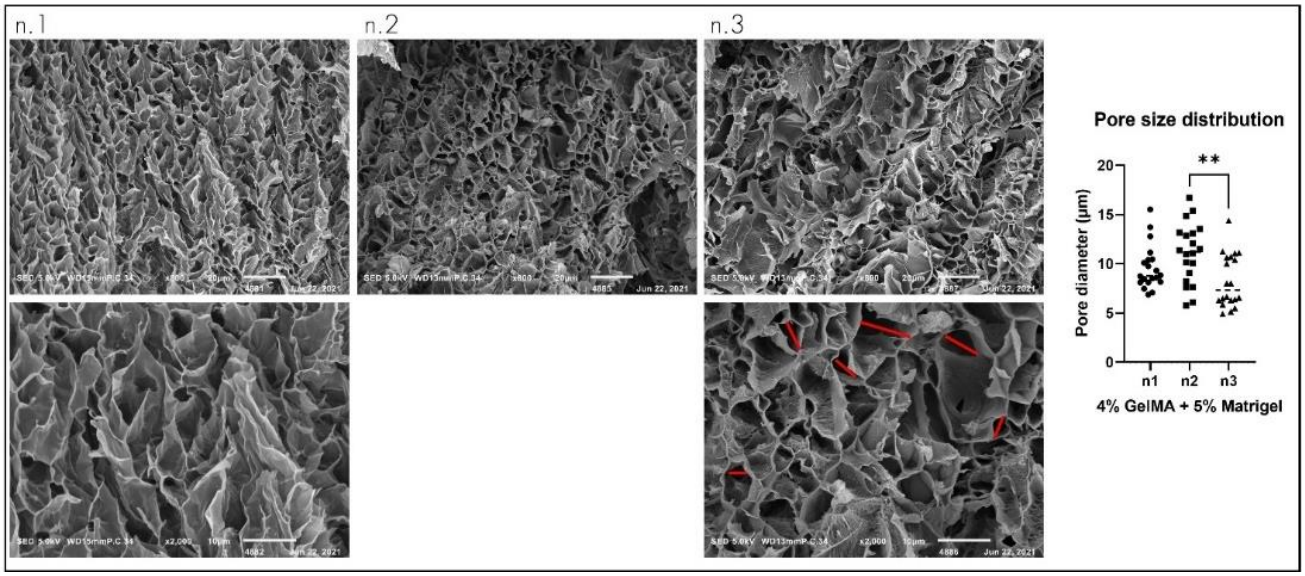

FIG. 3S HYDROGEL INTERNAL MORPHOLOGY AND PORE SIZE DISTRIBUTION; Scanning Electron Microscope (SEM) 800x (above) and 2000x (below) magnification was used to observe the inner morphology of cell-free hydrogels. All the samples present an irregular laminar organization. Sample n.3 (bottom picture) shows how measurements of pore size were taken on ImageJ. The graph shows the corresponding mean values of the pores for the corresponding sample of two dependent replications. Approximately, pores size is around 10 µm. $**p < 0.01$

4. Dynamic Mechanical Characterization (DMA)

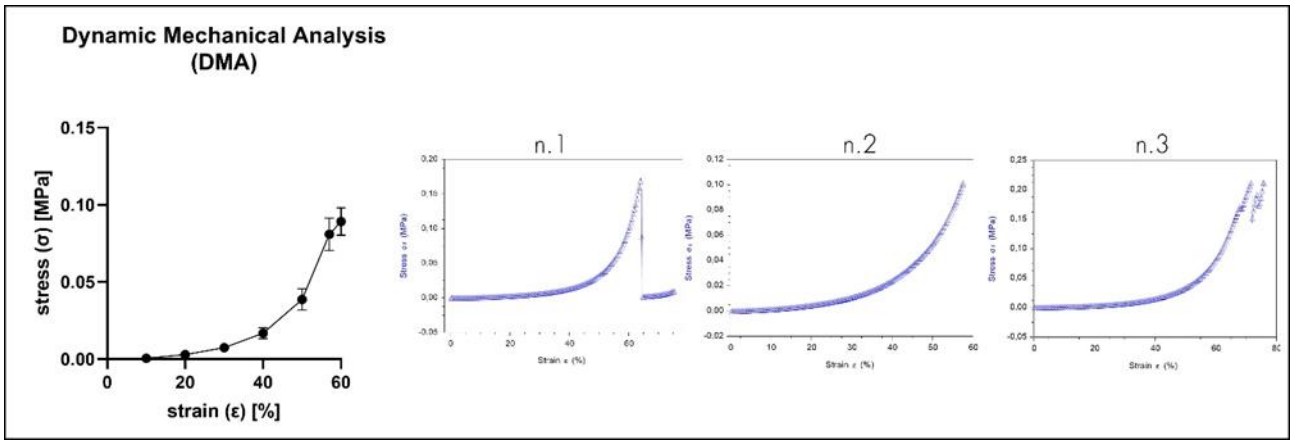

FIG. 4S STRAIN-STRESS CURVE OBTAINED FROM THE DYNAMIC MECHANICAL ANALYSIS (DMA) IN COMPRESSION. The graph shows the mean trend of the viscoelastic behaviour of three independent replicates (n.1, n.2, n.3) under compression. Considered strain range 10 - 60%. Data represents mean ± SEM for at least 3 independent experiments. *p < 0.05, **p < 0.01, ***p < 0.001.

5. BCM Mould Design

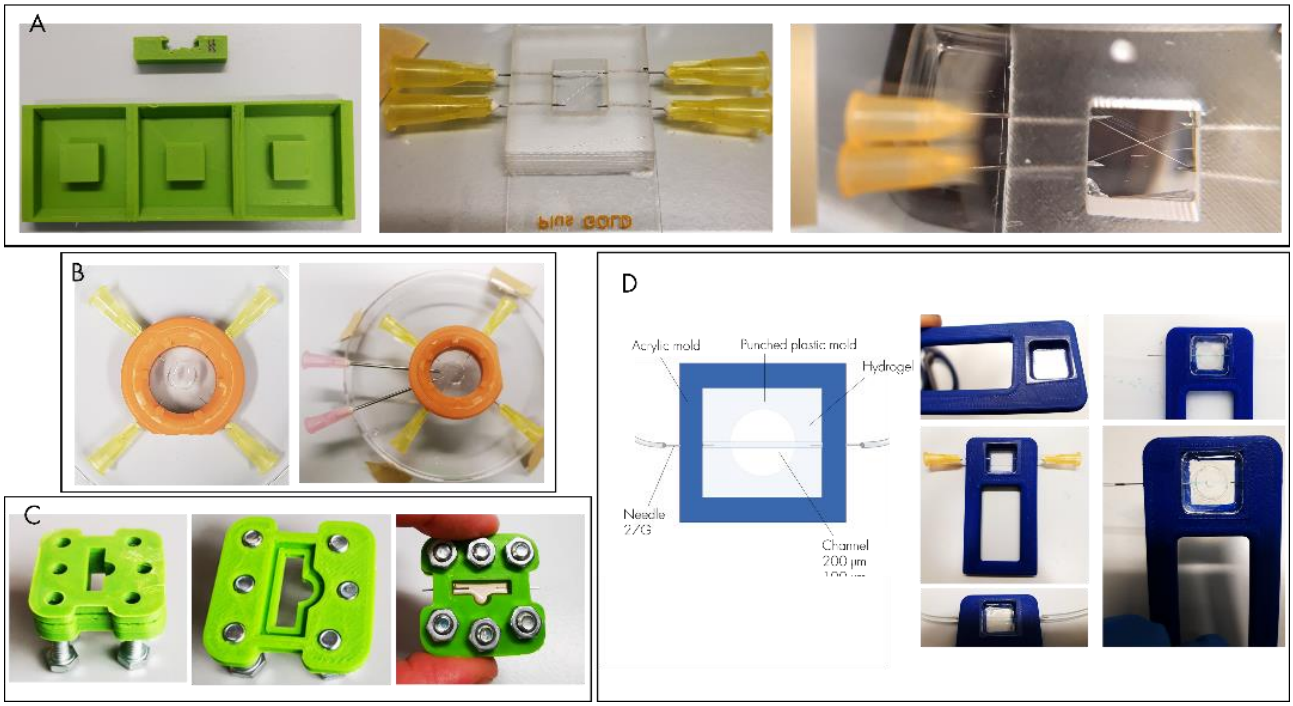

FIG. 5S DIFFERENT DESIGN OF THE ACRYLIC HOLDER FOR GELMA/MATRIGEL HYDROGEL. Each of these showed vulnerabilities and inappropriateness for the application of ultrasound due to potential wave distortions or attenuation caused by materials. Another limiting factor was given by the inability to crosslink the hydrogel due to the acrylic mould

6. BCM Protocol

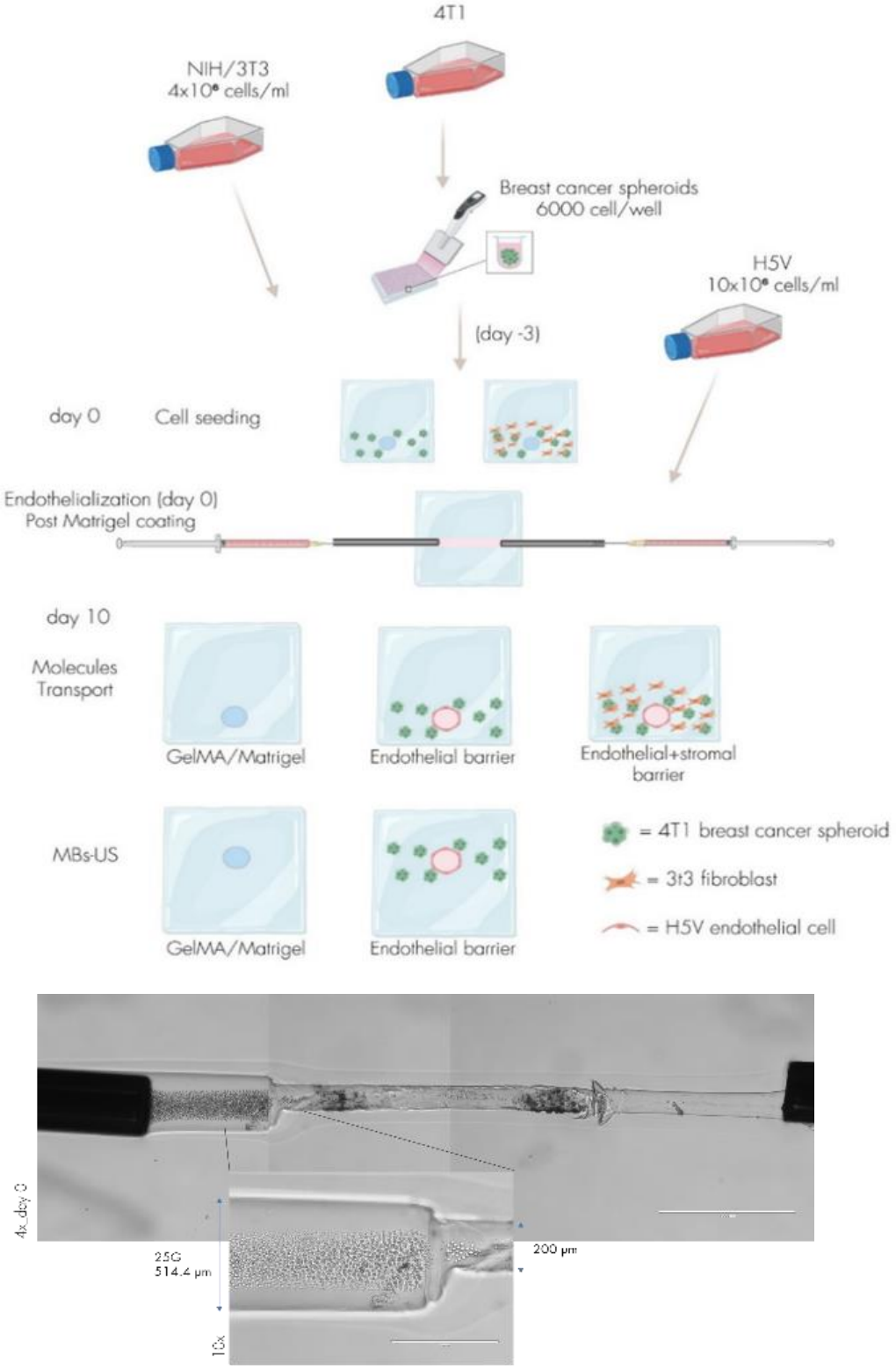

FIG. 6S SUM UP OF THE BCM MODEL ASSEMBLY PROCESS ORGANIZATION AND THE PREPARATION OF SAMPLES ACCPRDING TO THE APPLICATION AND (BELOW) A DETAIL OF THE ENDOTHELIAL SEEDING

7.BCM Biological Characterization

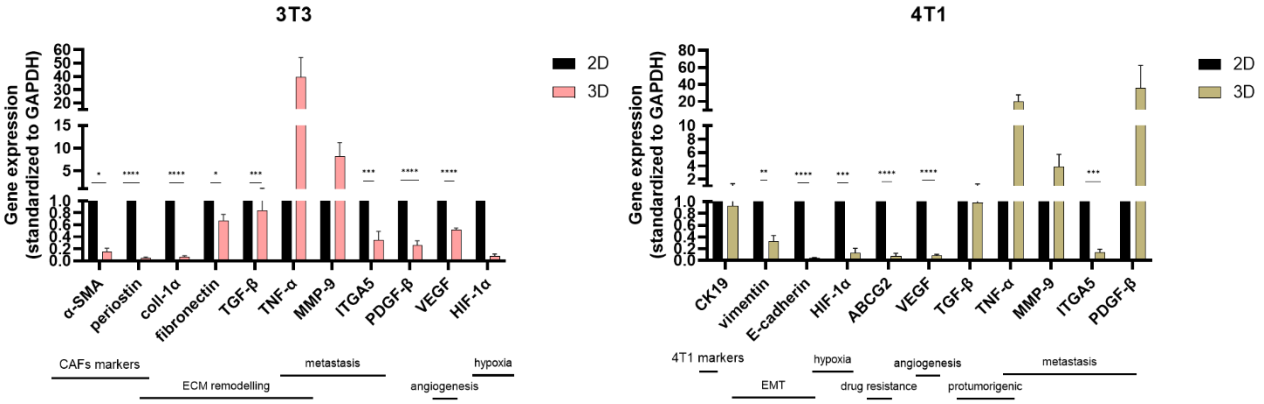

FIG. 7S GENE EXPRESSION OF 3T3 AND 4T1 MONOCULTURES IN 2D AND 3D (DAY 4) REVEAL THAT CELLS EXPERIENCE DIFFERENT STIMULI WHEN EMBEDDED IN 3D. IN PARTICULAR, IN BOTH CELL MONOCULTURE GENES ASSOCIATED WITH METASTASIS AND THUS MIGRATION ARE SIGNIFICANTLY UPREGULATED.

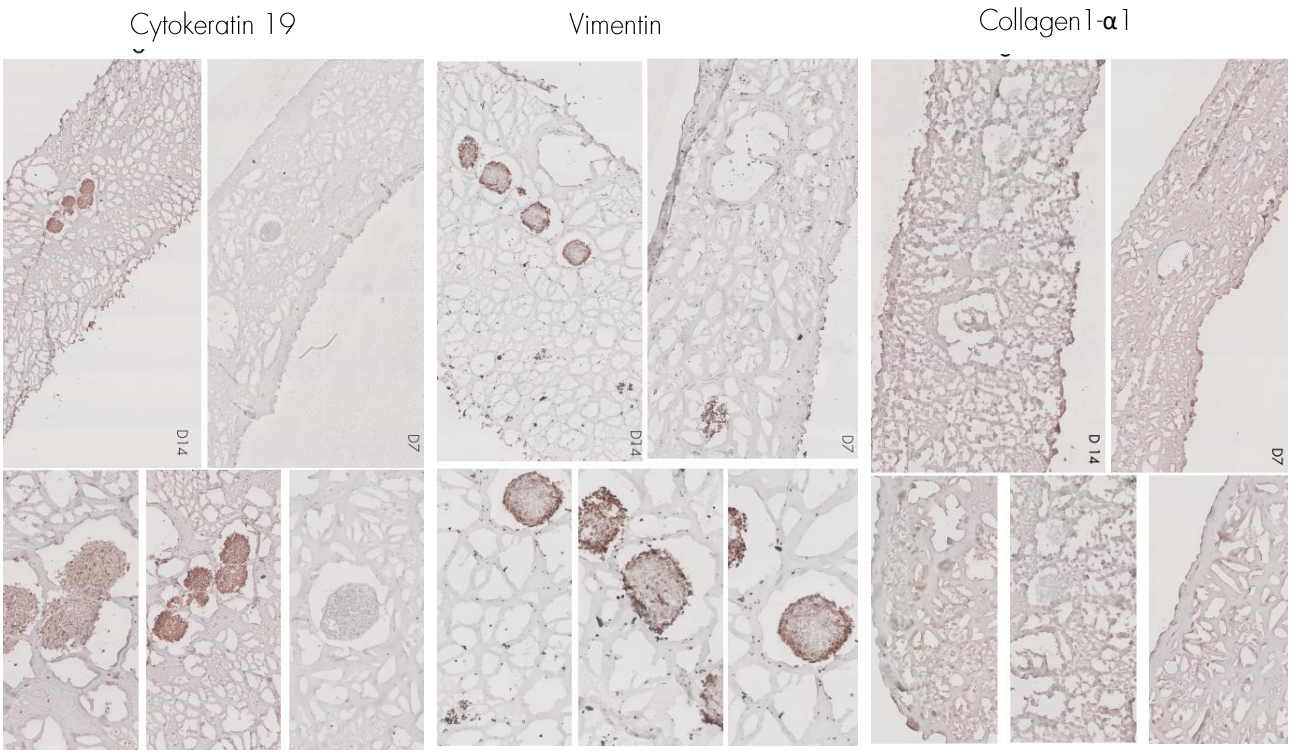

FIG. 8S IMMUNOHISTOCHEMISTRY FOR PROTEIN EXPRESSION ON DAY 7 AND DAY 14. Vimentin, cytokeratin 19, and collagen type i resulted in expressed, especially on day 14 confirming the dynamic and tumorigenic hydrogel-based microtissue.

9. Silica NPs Diffusion

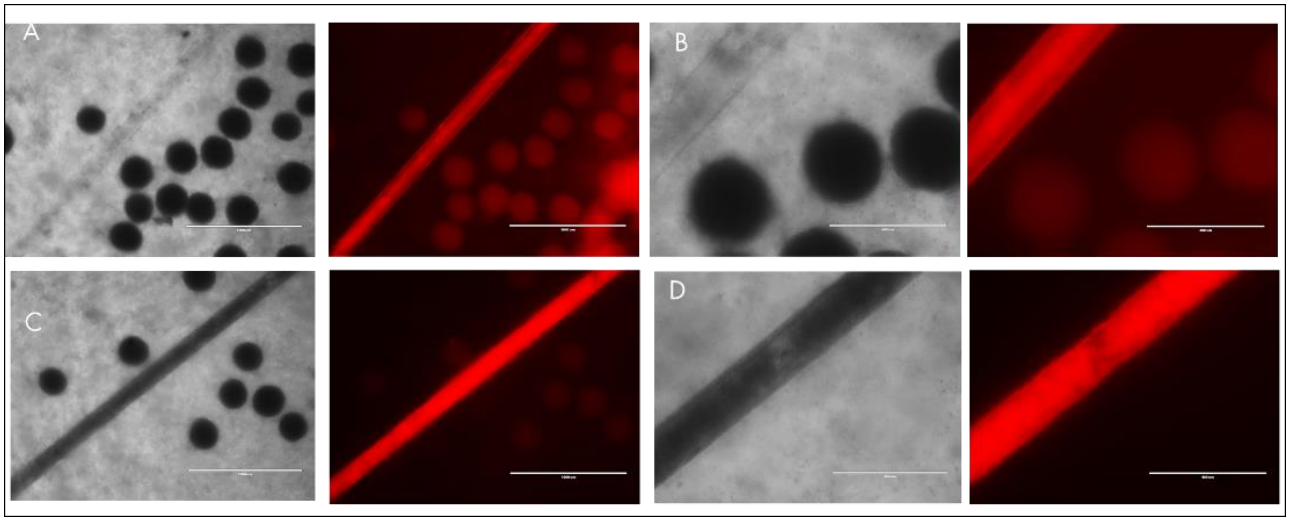

FIG.9S PERFUSION OF BCM(+) WITH SILICA NPs (100 nm) OVER 10 MIN IN THE PRESENCE OF AN EXTERNAL STROMA. Picture are taken with EVOS microscopy (4x and 10 x magnifications). In none of these cases, effective penetration of NPs into the surrounding stroma was observed.

10. MBs-US Research Approach

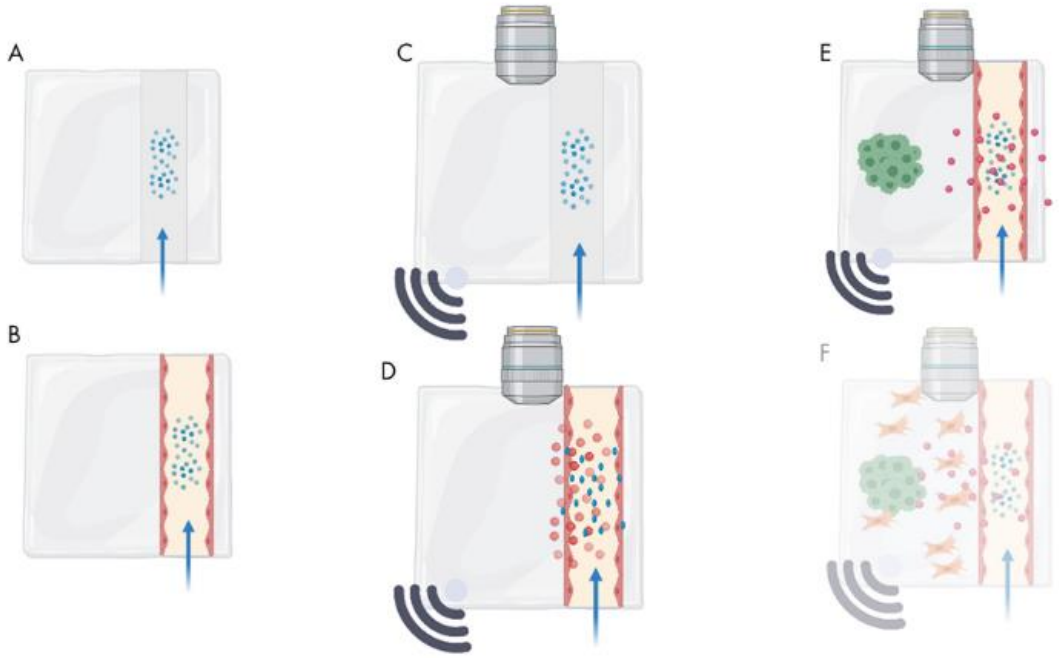

FIG. 10 S MBs-US RESEARCH APPROACH. BRIEFLY, A) MBs are perfuse into the cell-free hydrogel to check optical transparency of the hydrogel, and perfusion of the construct with the acoustical set up B) MBs are injected into the endothelialized channel. Even in this case of dense stroma we should be able to visualize MBs; C) MBs response to an external US beam are verified in a cell-free hydrogel (first) and later into an endothelialized channel; C) D) Show cavitation of MBs can be observed and studied. Especially in the second case, cavitation of MBs in proximity to the vessels walls can yield mechanobiological insights; F) follow-up studies the effect of MBs-US will be assessed on the dense tumorigenic stroma barrier.

11.Diffusion data analys

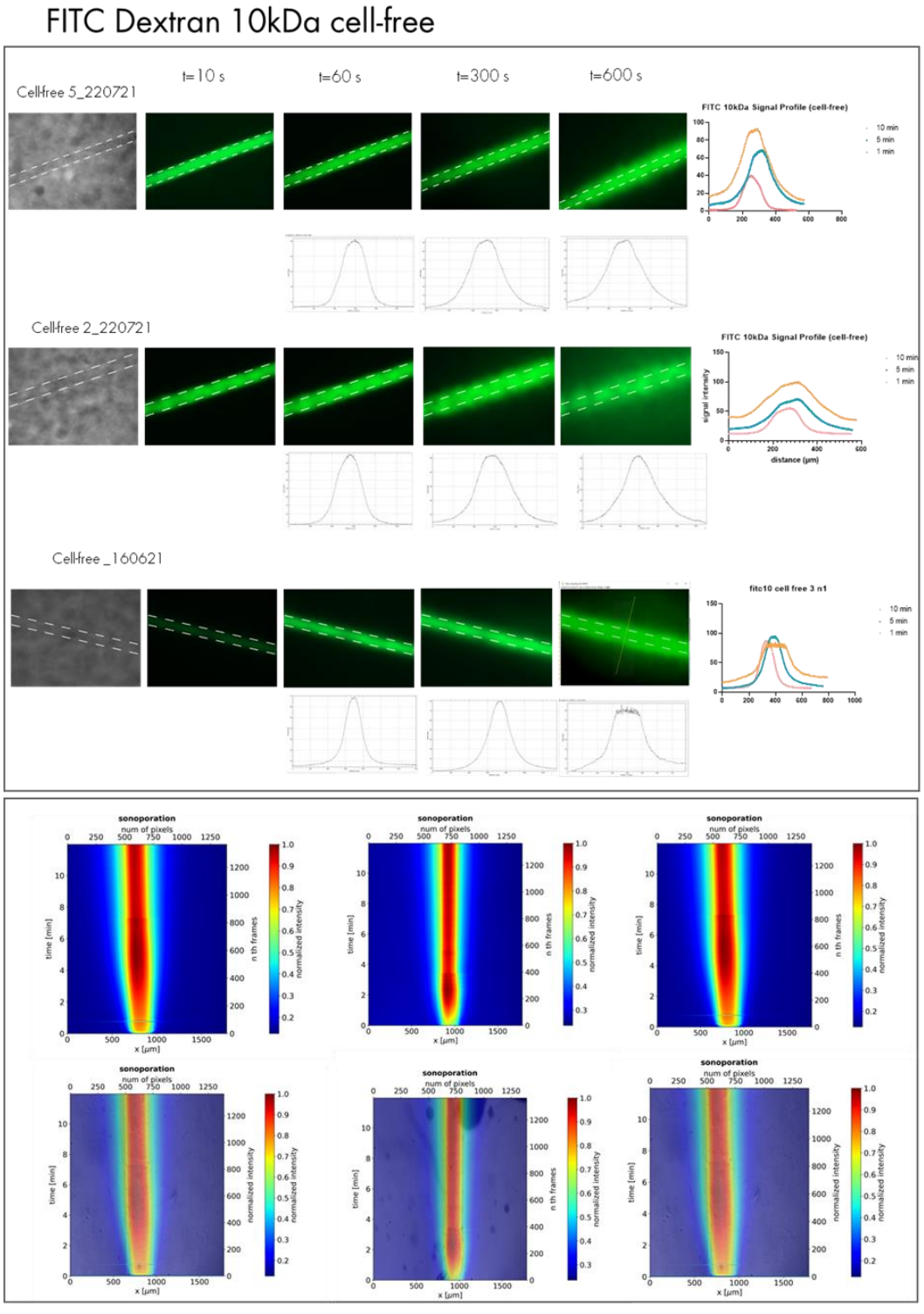

FIG. 10S SCHEME OF THE PROCEDURE EMPLOYED TO EVALUATE ENHANCED OR REDUCED MOLECULE DIFFUSION WITH OR WITHOUT ULTRASOUND IN THE PRESENCE OF A BIOLOGICAL BARRIER. In the first case, bright field microscopy images (4x) are used to delineate the wall of the vessel to draw perpendicular lines to the signal profile in every frame to measure the distance over time and thus diffusion rate. In the case of MBs-US, a self-generated Python code allowed the relatively fast and objective analysis of the diffusion data over signal intensity and time. The code is able to extract the signal intensity over distance and time and to summarize them in a heat map which, in turn, is measured on image j to elaborate data as in the molecules transport study.

References

1. WHO, W. H. O. Breast cancer now most common form of cancer: WHO taking action. https://www.who.int/news/item/03-02-2021-breast-cancer-now-most-common-form-of-cancer-who-taking-action (2021).
2. Organization, W. W. H. Breast cancer. https://www.who.int/news-room/fact-sheets/detail/breast-cancer.
3. ECIS - European Cancer Information System. *Breast cancer burden in EU-27: New cases of breast cancer per 100,000 women* deaths caused by breast cancer per 100,000 women* 2020 new cases (incidence) and deaths (mortality) estimates*. https://cancer-code-europe.iarc.fr.
4. Nazari, S. S. & Mukherjee, P. An overview of mammographic density and its association with breast cancer. *Breast Cancer* **25**, 259–267 (2018).
5. Dafni, U., Tsourti, Z. & Alatsathianos, I. Breast cancer statistics in the european union: Incidence and survival across european countries. *Breast Care* vol. 14 344–353 (2019).
6. Harbeck, N. *et al.* Breast cancer. *Nat. Rev. Dis. Prim.* **5**, 66 (2019).
7. American Cancer Society. cancer-treatment-and-survivorship-facts-and-figures-2019-2021.
8. Turashvili, G. & Brogi, E. Tumor Heterogeneity in Breast Cancer. *Front. Med.* **4**, 227 (2017).
9. Rebecca A. Shatsky, C. R. I. Immunotherapy for Breast Cancer.
10. Gordon, B. & Gadi, V. K. The Role of the Tumor Microenvironment in Developing Successful Therapeutic and Secondary Prophylactic Breast Cancer Vaccines. *Vaccines* **8**, (2020).
11. Martelotto, L. G., Ng, C. K. Y., Piscuoglio, S., Weigelt, B. & Reis-Filho, J. S. Breast cancer intra-tumor heterogeneity. *Breast Cancer Res.* **16**, 210 (2014).
12. Kalluri, R. & Zeisberg, M. Fibroblasts in cancer. *Nat. Rev. Cancer* **6**, 392–401 (2006).
13. Monteran, L. & Erez, N. The dark side of fibroblasts: Cancer-associated fibroblasts as mediators of immunosuppression in the tumor microenvironment. *Frontiers in Immunology* vol. 10 (2019).
14. Monteran, L. & Erez, N. The dark side of fibroblasts: Cancer-associated fibroblasts as mediators of immunosuppression in the tumor microenvironment. *Frontiers in Immunology* vol. 10 (2019).
15. Friedman, G. *et al.* Cancer-associated fibroblast compositions change with breast-cancer progression linking S100A4 and PDPN ratios with clinical outcome. *bioRxiv* 2020.01.12.903039 (2020) doi:10.1101/2020.01.12.903039.
16. Joshi, R. S. *et al.* The Role of Cancer-Associated Fibroblasts in Tumor Progression. *Cancers (Basel).* **13**, 1399 (2021).
17. Paulsson, J. & Micke, P. Prognostic relevance of cancer-associated fibroblasts in human cancer. *Semin. Cancer Biol.* **25**, 61–68 (2014).
18. Han, C., Liu, T. & Yin, R. Biomarkers for cancer-associated fibroblasts. *Biomark. Res.* **8**, 64 (2020).
19. Linares, J., Marín-Jiménez, J. A., Badia-Ramentol, J. & Calon, A. Determinants and Functions of CAFs Secretome During Cancer Progression and Therapy . *Frontiers in Cell and Developmental Biology* vol. 8 1706 (2021).
20. Sophia K. Apple, and L. W. B. Normal Breast Anatomy and Histology. in *Breast Imaging* (2018). doi:10.1093/med/9780190270261.003.0003.
21. Conklin, M. W. & Keely, P. J. Why the stroma matters in breast cancer: insights into breast cancer patient outcomes through the examination of stromal biomarkers. *Cell Adh. Migr.* **6**, 249–260 (2012).
22. Khamis, Z. I., Sahab, Z. J. & Sang, Q.-X. A. Active Roles of Tumor Stroma in Breast Cancer Metastasis. *Int. J. Breast Cancer* **2012**, 574025 (2012).
23. Ramião, N. G. *et al.* Biomechanical properties of breast tissue, a state-of-the-art review. *Biomech. Model. Mechanobiol.* **15**, 1307–1323 (2016).

24. Fernández-Nogueira, P. *et al.* Breast Mammographic Density: Stromal Implications on Breast Cancer Detection and Therapy. *Journal of Clinical Medicine* vol. 9 (2020).

25. Huo, C. W. *et al.* High mammographic density is associated with an increase in stromal collagen and immune cells within the mammary epithelium. *Breast Cancer Res.* **17**, 79 (2015).

26. Provenzano, P. P. *et al.* Collagen density promotes mammary tumor initiation and progression. *BMC Med.* **6**, 11 (2008).

27. Schober, M. *et al.* Desmoplasia and chemoresistance in pancreatic cancer. *Cancers (Basel).* **6**, 2137–2154 (2014).

28. Winkler, J., Abisoye-Ogunniyan, A., Metcalf, K. J. & Werb, Z. Concepts of extracellular matrix remodelling in tumour progression and metastasis. *Nat. Commun.* **11**, 5120 (2020).

29. Henke, E., Nandigama, R. & Ergün, S. Extracellular Matrix in the Tumor Microenvironment and Its Impact on Cancer Therapy. *Frontiers in Molecular Biosciences* vol. 6 (2020).

30. Paszek, M. J. *et al.* Tensional homeostasis and the malignant phenotype. *Cancer Cell* **8**, 241–254 (2005).

31. Levental, K. R. *et al.* Matrix crosslinking forces tumor progression by enhancing integrin signaling. *Cell* **139**, 891–906 (2009).

32. Mohammadi, H. & Sahai, E. Mechanisms and impact of altered tumour mechanics. *Nat. Cell Biol.* **20**, 766–774 (2018).

33. Ping, Q. *et al.* Cancer-associated fibroblasts: overview, progress, challenges, and directions. *Cancer Gene Ther.* (2021) doi:10.1038/s41417-021-00318-4.

34. Madu, C. O., Wang, S., Madu, C. O. & Lu, Y. Angiogenesis in Breast Cancer Progression, Diagnosis, and Treatment. *J. Cancer* **11**, 4474–4494 (2020).

35. Farnsworth, R. H., Lackmann, M., Achen, M. G. & Stacker, S. A. Vascular remodeling in cancer. *Oncogene* **33**, 3496–3505 (2014).

36. Ribatti, D., Nico, B., Crivellato, E. & Vacca, A. The structure of the vascular network of tumors. *Cancer Lett.* **248**, 18–23 (2007).

37. Siemann, D. W. The unique characteristics of tumor vasculature and preclinical evidence for its selective disruption by Tumor-Vascular Disrupting Agents. *Cancer Treat. Rev.* **37**, 63–74 (2011).

38. Dewhirst, M. W., Cao, Y. & Moeller, B. Cycling hypoxia and free radicals regulate angiogenesis and radiotherapy response. *Nat. Rev. Cancer* **8**, 425–437 (2008).

39. Vaupel, P. & Hockel, M. Blood supply, oxygenation status and metabolic micromilieu of breast cancers: characterization and therapeutic relevance. *Int. J. Oncol.* **17**, 869–879 (2000).

40. Valkenburg, K. C., de Groot, A. E. & Pienta, K. J. Targeting the tumour stroma to improve cancer therapy. *Nat. Rev. Clin. Oncol.* **15**, 366–381 (2018).

41. Plava, J. *et al.* Recent advances in understanding tumor stroma-mediated chemoresistance in breast cancer. *Mol. Cancer* **18**, 67 (2019).

42. Tanaka, H. Y. & Kano, M. R. Stromal barriers to nanomedicine penetration in the pancreatic tumor microenvironment. *Cancer Sci.* **109**, 2085–2092 (2018).

43. Miao, L., Lin, C. M. & Huang, L. Stromal barriers and strategies for the delivery of nanomedicine to desmoplastic tumors. *J. Control. Release* **219**, 192–204 (2015).

44. Oskarsson, T. Extracellular matrix components in breast cancer progression and metastasis. *The Breast* **22**, S66–S72 (2013).

45. Henke, E., Nandigama, R. & Ergün, S. Extracellular Matrix in the Tumor Microenvironment and Its Impact on Cancer Therapy. *Front. Mol. Biosci.* **6**, 160 (2020).

46. Logsdon, D. K., Beeghly, G. F. & Munson, J. M. Chemoprotection Across the Tumor Border: Cancer Cell Response to Doxorubicin Depends on Stromal Fibroblast Ratios and Interstitial Therapeutic Transport. *Cell. Mol. Bioeng.* **10**, 463–481 (2017).

47. Fisusi, F. A. & Akala, E. O. Drug Combinations in Breast Cancer Therapy. *Pharm. Nanotechnol.* **7**, 3–23 (2019).

48. Anselmo, A. C. & Mitragotri, S. Nanoparticles in the clinic: An update. *Bioeng. \& Transl. Med.* **4**, e10143 (2019).

49. Salvioni, L. *et al.* Thirty Years of Cancer Nanomedicine: Success, Frustration, and Hope. *Cancers (Basel).* **11**, (2019).

50. van der Meel, R. *et al.* Smart cancer nanomedicine. *Nat. Nanotechnol.* **14**, 1007–1017 (2019).

51. Zhang, Y.-R. *et al.* Strategies to improve tumor penetration of nanomedicines through nanoparticle design. *Wiley Interdiscip. Rev. Nanomedicine Nanobiotechnology* **11**, e1519 (2018).

52. Roma-Rodrigues, C., Mendes, R., Baptista, P. V & Fernandes, A. R. Targeting Tumor Microenvironment for Cancer Therapy. *Int. J. Mol. Sci.* **20**, 840 (2019).

53. Diop-Frimpong, B., Chauhan, V. P., Krane, S., Boucher, Y. & Jain, R. K. Losartan inhibits collagen I synthesis and improves the distribution and efficacy of nanotherapeutics in tumors. *Proc. Natl. Acad. Sci.* **108**, 2909 LP – 2914 (2011).

54. Baghban, R. *et al.* Tumor microenvironment complexity and therapeutic implications at a glance. *Cell Commun. Signal.* **18**, 59 (2020).

55. DuRoss, A. N., Neufeld, M. J., Rana, S., Thomas Jr, C. R. & Sun, C. Integrating nanomedicine into clinical radiotherapy regimens. *Adv. Drug Deliv. Rev.* **144**, 35–56 (2019).

56. Min, Y. *et al.* Antigen-capturing nanoparticles improve the abscopal effect and cancer immunotherapy. *Nat. Nanotechnol.* **12**, 877–882 (2017).

57. Kouloulias, V. *et al.* Hyperthermia Is Now Included in the NCCN Clinical Practice Guidelines for Breast Cancer Recurrences: An Analysis of Existing Data. *Breast Care (Basel).* **10**, 109–116 (2015).

58. Triantopoulou, S. *et al.* Radiotherapy in conjunction with superficial and intracavitary hyperthermia for the treatment of solid tumors: survival and thermal parameters. *Clin. Transl. Oncol. Off. Publ. Fed. Spanish Oncol. Soc. Natl. Cancer Inst. Mex.* **15**, 95–105 (2013).

59. Cheng, Y. *et al.* The Role of Hyperthermia in the Multidisciplinary Treatment of Malignant Tumors. *Integr. Cancer Ther.* **18**, 1534735419876345–1534735419876345 (2019).

60. Fiorentini, G. *et al.* A Narrative Review of Regional Hyperthermia: Updates From 2010 to 2019. *Integr. Cancer Ther.* **19**, (2020).

61. Amrahli, M. *et al.* MR-labelled liposomes and focused ultrasound for spatiotemporally controlled drug release in triple negative breast cancers in mice. *Nanotheranostics* **5**, 125–142 (2021).

62. Farr, N. *et al.* Hyperthermia-enhanced targeted drug delivery using magnetic resonance-guided focussed ultrasound: a pre-clinical study in a genetic model of pancreatic cancer. *Int. J. Hyperth. Off. J. Eur. Soc. Hyperthermic Oncol. North Am. Hyperth. Gr.* **34**, 284–291 (2018).

63. Frazier, N. & Ghandehari, H. Hyperthermia approaches for enhanced delivery of nanomedicines to solid tumors. (2015) doi:10.1002/bit.25653.

64. Mallidi, S. *et al.* Beyond the Barriers of Light Penetration: Strategies, Perspectives and Possibilities for Photodynamic Therapy. *Theranostics* **6**, 2458–2487 (2016).

65. Min, D., Jeong, D., Choi, M. G. & Na, K. Photochemical tissue penetration via photosensitizer for effective drug penetration in a non-vascular tumor. *Biomaterials* **52**, 484–493 (2015).

66. Lai, C., Fite, B. & Ferrara, K. Ultrasonic Enhancement of Drug Penetration in Solid Tumors . *Frontiers in Oncology* vol. 3 204 (2013).

67. Liang, H.-D., Tang, J. & Halliwell, M. Sonoporation, drug delivery, and gene therapy. *Proc. Inst. Mech. Eng. Part H, J. Eng. Med.* **224**, 343–361 (2010).

68. Sharma, D. *et al.* Optimization of microbubble enhancement of hyperthermia for cancer therapy in an in vivo breast tumour model. *PLoS One* **15**, e0237372 (2020).

69. Lee, H. *et al.* Combination of chemotherapy and photodynamic therapy for cancer treatment with sonoporation effects. *J. Control. Release* **283**, (2018).

70. Dimcevski, G. *et al.* A human clinical trial using ultrasound and microbubbles to enhance gemcitabine treatment of inoperable pancreatic cancer. *J. Control. Release* **243**, 172–181 (2016).

71. Tharkar, P., Varanasi, R., Wong, W. S. F., Jin, C. T. & Chrzanowski, W. Nano-Enhanced Drug Delivery and Therapeutic Ultrasound for Cancer Treatment and Beyond. *Front. Bioeng. Biotechnol.* **7**, 324 (2019).

72. Stride, E. & Coussios, C. Nucleation, mapping and control of cavitation for drug delivery. *Nat. Rev. Phys.* **1**, 495–509 (2019).

73. van den Berg, A., Mummery, C. L., Passier, R. & van der Meer, A. D. Personalised organs-on-chips: functional testing for precision medicine. *Lab Chip* **19**, 198–205 (2019).

74. Yu, F., Hunziker, W. & Choudhury, D. Engineering Microfluidic Organoid-on-a-Chip Platforms. *Micromachines* **10**, 165 (2019).

75. Prasad, V. & Mailankody, S. Research and Development Spending to Bring a Single Cancer Drug to Market and Revenues After Approval. *JAMA Intern. Med.* **177**, 1569–1575 (2017).

76. Fogel, D. B. Factors associated with clinical trials that fail and opportunities for improving the likelihood of success: A review. *Contemp. Clin. trials Commun.* **11**, 156–164 (2018).

77. Santo, V. E. *et al.* Drug screening in 3D in vitro tumor models: overcoming current pitfalls of efficacy read-outs. *Biotechnol. J.* **12**, (2017).

78. Hutchinson, L. & Kirk, R. High drug attrition rates–where are we going wrong? *Nature reviews. Clinical oncology* vol. 8 189–190 (2011).

79. Rodenhizer, D., Dean, T., D'Arcangelo, E. & McGuigan, A. P. The Current Landscape of 3D In Vitro Tumor Models: What Cancer Hallmarks Are Accessible for Drug Discovery? *Adv. Healthc. Mater.* **7**, 1701174 (2018).

80. Boussommier-Calleja, A. In vitro models of cancer. in *Bioengineering Innovative Solutions for Cancer* (ed. Sylvain Ladame Jason Chang) 273–325 (2020).

81. Priwitaningrum, D. L. *et al.* Tumor stroma-containing 3D spheroid arrays: A tool to study nanoparticle penetration. *J. Control. Release* **244**, 257–268 (2016).

82. Brancato, V. *et al.* 3D breast cancer microtissue reveals the role of tumor microenvironment on the transport and efficacy of free-doxorubicin in vitro. *Acta Biomater.* **75**, 200–212 (2018).

83. Rodrigues, J., Heinrich, M. A., Teixeira, L. M. & Prakash, J. 3D In Vitro Model (R)evolution: Unveiling Tumor–Stroma Interactions. *Trends in Cancer* **7**, 249–264 (2021).

84. Lajoinie, G. *et al.* In vitro methods to study bubble-cell interactions: Fundamentals and therapeutic applications. *Biomicrofluidics* **10**, 11501 (2016).

85. Beekers, I. *et al.* Acoustic Characterization of a Vessel-on-a-Chip Microfluidic System for Ultrasound-Mediated Drug Delivery. *IEEE Trans. Ultrason. Ferroelectr. Freq. Control* **65**, 570–581 (2018).

86. Park, Y. C. *et al.* Microvessels-on-a-Chip to Assess Targeted Ultrasound-Assisted Drug Delivery. *ACS Appl. Mater. Interfaces* **8**, 31541–31549 (2016).

87. Juang, E. K. *et al.* Engineered 3D Microvascular Networks for the Study of Ultrasound-Microbubble-Mediated Drug Delivery. *Langmuir* **35**, 10128–10138 (2019).

88. Bui, L. *et al.* Development of a custom biological scaffold for investigating ultrasound-mediated intracellular delivery. *Mater. Sci. Eng. C* **70**, 461–470 (2017).

89. Beekers, I. *et al.* Opening of endothelial cell–cell contacts due to sonoporation. *J. Control. Release* **322**, 426–438 (2020).

90. Pereno, V. *et al.* Layered acoustofluidic resonators for the simultaneous optical and acoustic characterisation of cavitation dynamics, microstreaming, and biological effects. *Biomicrofluidics* **12**, 34109 (2018).

91. Bourn, M. D. *et al.* High-throughput microfluidics for evaluating microbubble enhanced delivery of cancer therapeutics in spheroid cultures. *J. Control. Release* **326**, 13–24 (2020).

92. Moncion, A. *et al.* Design and Characterization of Fibrin-Based Acoustically Responsive Scaffolds for Tissue Engineering Applications. *Ultrasound Med. Biol.* **42**, 257–271 (2016).

93. Grisanti, G. *et al.* A Microfluidic Platform for Cavitation-Enhanced Drug Delivery. *Micromachines* vol. 12 (2021).

94. Pepelanova, I., Kruppa, K., Scheper, T. & Lavrentieva, A. Gelatin-Methacryloyl (GelMA) Hydrogels with Defined Degree of Functionalization as a Versatile Toolkit for 3D Cell Culture and Extrusion Bioprinting. *Bioeng. (Basel, Switzerland)* **5**, (2018).

95. Harris, A. R., Perez, M. J. & Munson, J. M. Docetaxel facilitates lymphatic-tumor crosstalk to promote lymphangiogenesis and cancer progression. *BMC Cancer* **18**, 718 (2018).

96. Drost, J. & Clevers, H. Organoids in cancer research. *Nat. Rev. Cancer* **18**, 407–418 (2018).

97. Joyce, M. H. *et al.* Phenotypic Basis for Matrix Stiffness-Dependent Chemoresistance of Breast Cancer Cells to Doxorubicin. *Front. Oncol.* **8**, 337 (2018).

98. Marusyk, A. *et al.* Spatial Proximity to Fibroblasts Impacts Molecular Features and Therapeutic Sensitivity of Breast Cancer Cells Influencing Clinical Outcomes. *Cancer Res.* **76**, 6495–6506 (2016).

99. Landry, B. D. *et al.* Tumor-stroma interactions differentially alter drug sensitivity based on the origin of stromal cells. *Mol. Syst. Biol.* **14**, e8322–e8322 (2018).

100. Cafarelli, A. *et al.* Tuning acoustic and mechanical properties of materials for ultrasound phantoms and smart substrates for cell cultures. *Acta Biomater.* **49**, (2016).

101. Wilhelm, S. *et al.* Analysis of nanoparticle delivery to tumours. *Nat. Rev. Mater.* **1**, 16014 (2016).

102. Nichol, J. W. *et al.* Cell-laden microengineered gelatin methacrylate hydrogels. *Biomaterials* **31**, 5536–5544 (2010).

103. Dubois, T. Expression profiling of breast cancer samples from Institut Curie (Maire cohort) –Affy CDF. *Public on Jan 23, 2015* https://www.ncbi.nlm.nih.gov/geo/query/acc.cgi?acc=GSE65194.

104. Volk, A. & Kähler, C. J. Density model for aqueous glycerol solutions. *Exp. Fluids* **59**, 75 (2018).

105. Roovers, S. *et al.* The Role of Ultrasound-Driven Microbubble Dynamics in Drug Delivery: From Microbubble Fundamentals to Clinical Translation. *Langmuir* **35**, 10173–10191 (2019).

106. Fan, Z., Chen, D. & Deng, C. X. Improving ultrasound gene transfection efficiency by controlling ultrasound excitation of microbubbles. *J. Control. Release* **170**, 401–413 (2013).

107. Obregón, R. *et al.* Chapter 13 - Gradient Biomaterials as Tissue Scaffolds. in (eds. Vishwakarma, A., Sharpe, P., Shi, S. & Ramalingam, M. B. T.-S. C. B. and T. E. in D. S.) 175–186 (Academic Press, 2015). doi:https://doi.org/10.1016/B978-0-12-397157-9.00015-1.

108. Sukriti, S., Tauseef, M., Yazbeck, P. & Mehta, D. Mechanisms regulating endothelial permeability. *Pulm. Circ.* **4**, 535–551 (2014).

109. Dravid, A. *et al.* A Macroscopic Diffusion-Based Gradient Generator to Establish Concentration Gradients of Soluble Molecules Within Hydrogel Scaffolds for Cell Culture. *Front. Chem.* **7**, 638 (2019).

110. Gorgieva, S. & Kokol, V. Collagen- vs. Gelatine-Based Biomaterials and Their Biocompatibility: Review and Perspectives. in (2011). doi:10.5772/24118.

111. Aubin, H. *et al.* Directed 3D cell alignment and elongation in microengineered hydrogels. *Biomaterials* **31**, 6941–6951 (2010).

112. Gomes, L. R., Vessoni, A. T. & Menck, C. F. M. Three-dimensional microenvironment confers enhanced sensitivity to doxorubicin by reducing p53-dependent induction of autophagy. *Oncogene* **34**, 5329–5340 (2015).

113. Rong, G., Kang, H., Wang, Y., Hai, T. & Sun, H. Candidate markers that associate with chemotherapy resistance in breast cancer through the study on Taxotere-induced damage to tumor microenvironment and gene expression profiling of carcinoma-associated fibroblasts (CAFs). *PLoS One* **8**, e70960–e70960 (2013).

114. Lee, Y. *et al.* Photo-crosslinkable hydrogel-based 3D microfluidic culture device. *Electrophoresis* **36**, (2015).

115. Anguiano, M. *et al.* Characterization of three-dimensional cancer cell migration in mixed collagen-Matrigel scaffolds using microfluidics and image analysis. *PLoS One* **12**, e0171417–e0171417 (2017).

116. Benton, J. A., DeForest, C. A., Vivekanandan, V. & Anseth, K. S. Photocrosslinking of gelatin macromers to synthesize porous hydrogels that promote valvular interstitial cell function. *Tissue Eng. Part A* **15**, 3221–3230 (2009).

117. Gorth, D. & J Webster, T. 10 - Matrices for tissue engineering and regenerative medicine. in *Woodhead Publishing Series in Biomaterials* (eds. Lysaght, M. & Webster, T. J. B. T.-B. for A. O.) 270–286 (Woodhead Publishing, 2011). doi:https://doi.org/10.1533/9780857090843.2.270.

118. Loh, Q. L. & Choong, C. Three-dimensional scaffolds for tissue engineering applications: role of porosity and pore size. *Tissue Eng. Part B. Rev.* **19**, 485–502 (2013).

119. Ying, G.-L. *et al.* Aqueous Two-Phase Emulsion Bioink-Enabled 3D Bioprinting of Porous Hydrogels. *Adv. Mater.* **30**, e1805460–e1805460 (2018).

120. He, Y. *et al.* Research on the printability of hydrogels in 3D bioprinting. *Sci. Rep.* **6**, 29977 (2016).

121. Bereiter-Hahn, J., Münnich, A. & Woiteneck, P. Dependence of energy metabolism on the density of cells in culture. *Cell Struct. Funct.* **23**, 85–93 (1998).

122. Fung, Y. C. *Biomechanics- Mechanical Properties of Living Tissues.* (Springer-Verlag New York, 1981). doi:10.1007/978-1-4757-1752-5.

123. Xiao, Y., Friis, E. A., Gehrke, S. H. & Detamore, M. S. Mechanical Testing of Hydrogels in Cartilage Tissue Engineering: Beyond the Compressive Modulus. *Tissue Eng. Part B Rev.* **19**, 403–412 (2013).

124. Zhu, M. *et al.* Gelatin methacryloyl and its hydrogels with an exceptional degree of controllability and batch-to-batch consistency. *Sci. Rep.* **9**, 6863 (2019).

125. Aisenbrey, E. A. & Murphy, W. L. Synthetic alternatives to Matrigel. *Nat. Rev. Mater.* **5**, 539–551 (2020).

126. Krishnamoorthy, S., Noorani, B. & Xu, C. Effects of Encapsulated Cells on the Physical–Mechanical Properties and Microstructure of Gelatin Methacrylate Hydrogels. *International Journal of Molecular Sciences* vol. 20 (2019).

127. Kessenbrock, K., Plaks, V. & Werb, Z. Matrix metalloproteinases: regulators of the tumor microenvironment. *Cell* **141**, 52–67 (2010).

128. Gao, Z. *et al.* Association of E-cadherin, matrix metalloproteinases, and tissue inhibitors of metalloproteinases with the progression and metastasis of hepatocellular carcinoma. *Mod. Pathol. an Off. J. United States Can. Acad. Pathol. Inc* **19**, 533–540 (2006).

129. Wang, X. *et al.* KLF8 promotes human breast cancer cell invasion and metastasis by transcriptional activation of MMP9. *Oncogene* **30**, 1901–1911 (2011).

130. Deryugina, E. I. & Quigley, J. P. Tumor angiogenesis: MMP-mediated induction of intravasation- and metastasis-sustaining neovasculature. *Matrix Biol.* **44–46**, 94–112 (2015).

131. Quaranta, M. *et al.* MMP-2, MMP-9, VEGF and CA 15.3 in breast cancer. *Anticancer Res.* **27**, 3593–3600 (2007).

132. Jang, M. J. *et al.* Enhanced wound healing using a 3D printed VEGF-mimicking peptide incorporated hydrogel patch in a pig model. *Biomed. Mater.* **16**, (2021).

133. Li, M.-N. *et al.* Gelatin methacryloyl hydrogels functionalized with endothelin-1 for angiogenesis and full-thickness wound healing. *J. Mater. Chem. B* **9**, 4700–4709 (2021).

134. Lerrer, S. *et al.* Co-Inflammatory Roles of TGFβ1 in the Presence of TNFα Drive a Pro-inflammatory Fate in Mesenchymal Stem Cells . *Frontiers in Immunology* vol. 8 479 (2017).

135. Xie, L. *et al.* Transforming growth factor beta-regulated gene expression in a mouse mammary gland epithelial cell line. *Breast Cancer Res.* **5**, R187 (2003).

136. Liao, S.-J. *et al.* TGF-β1 and TNF-α synergistically induce epithelial to mesenchymal transition of breast cancer cells by enhancing TAK1 activation. *J. Cell Commun. Signal.* **13**, 369–380 (2019).

137. Sudo, T. *et al.* Expression of mesenchymal markers vimentin and fibronectin: the clinical significance in esophageal squamous cell carcinoma. *Ann. Surg. Oncol.* **20 Suppl 3**, S324-35 (2013).

138. Li, C.-L. *et al.* Fibronectin induces epithelial-mesenchymal transition in human breast cancer MCF-7 cells via activation of calpain. *Oncol. Lett.* **13**, 3889–3895 (2017).

139. Sugimoto, H., Mundel, T. M., Kieran, M. W. & Kalluri, R. Identification of fibroblast heterogeneity in the tumor microenvironment. *Cancer Biol. Ther.* **5**, 1640–1646 (2006).

140. Elisha, Y., Kalchenko, V., Kuznetsov, Y. & Geiger, B. Dual role of E-cadherin in the regulation of invasive collective migration of mammary carcinoma cells. *Sci. Rep.* **8**, 4986 (2018).

141. Ju, J. A. *et al.* Hypoxia Selectively Enhances Integrin α(5)β(1) Receptor Expression in Breast Cancer to Promote Metastasis. *Mol. Cancer Res.* **15**, 723–734 (2017).

142. Pinto, M. P., Dye, W. W., Jacobsen, B. M. & Horwitz, K. B. Malignant stroma increases luminal breast cancer cell proliferation and angiogenesis through platelet-derived growth factor signaling. *BMC Cancer* **14**, 735 (2014).

143. Nissen, N. I., Karsdal, M. & Willumsen, N. Collagens and Cancer associated fibroblasts in the reactive stroma and its relation to Cancer biology. *Journal of Experimental and Clinical Cancer Research* vol. 38 (2019).

144. Campbell, P. G., Miller, E. D., Fisher, G. W., Walker, L. M. & Weiss, L. E. Engineered spatial patterns of FGF-2 immobilized on fibrin direct cell organization. *Biomaterials* **26**, 6762–6770 (2005).

145. Vasaturo, A. *et al.* A novel chemotaxis assay in 3-D collagen gels by time-lapse microscopy. *PLoS One* **7**, e52251 (2012).

146. Lühmann, T. & Hall, H. Cell Guidance by 3D-Gradients in Hydrogel Matrices: Importance for Biomedical Applications. *Materials* vol. 2 (2009).

147. Cabral, H. *et al.* Accumulation of sub-100 nm polymeric micelles in poorly permeable tumours depends on size. *Nat. Nanotechnol.* **6**, 815–823 (2011).

148. Wang, J. *et al.* The Role of Micelle Size in Tumor Accumulation, Penetration, and Treatment. *ACS Nano* **9**, 7195–7206 (2015).

149. Albro, M. B., Rajan, V., Li, R., Hung, C. T. & Ateshian, G. A. Characterization of the Concentration-Dependence of Solute Diffusivity and Partitioning in a Model Dextran–Agarose Transport System. *Cell. Mol. Bioeng.* **2**, 295–305 (2009).

150. Ramanujan, S. *et al.* Diffusion and Convection in Collagen Gels: Implications for Transport in the Tumor Interstitium. *Biophys. J.* **83**, 1650–1660 (2002).

151. Seo, B. R., DelNero, P. & Fischbach, C. In vitro models of tumor vessels and matrix: engineering approaches to investigate transport limitations and drug delivery in cancer. *Adv. Drug Deliv. Rev.* **69–70**, 205–216 (2014).

152. Ernsting, M. J., Murakami, M., Roy, A. & Li, S.-D. Factors controlling the pharmacokinetics, biodistribution and intratumoral penetration of nanoparticles. *J. Control. Release* **172**, 782–794 (2013).

153. Komarova, Y. A., Kruse, K., Mehta, D. & Malik, A. B. Protein Interactions at Endothelial Junctions and Signaling Mechanisms Regulating Endothelial Permeability. *Circ. Res.* **120**, 179–206 (2017).

154. Yeste, J., Illa, X., Alvarez, M. & Villa, R. Engineering and monitoring cellular barrier models. *J. Biol. Eng.* **12**, 18 (2018).

155. Shams, M. M., Dong, M. & Mahinpey, N. Viscosity and rheological behavior of microbubbles in capillary tubes. *AIChE J.* **60**, 2660–2669 (2014).

156. Bezer, J. H., Koruk, H., Rowlands, C. J. & Choi, J. J. Elastic Deformation of Soft Tissue-Mimicking Materials Using a Single Microbubble and Acoustic Radiation Force. *Ultrasound Med. Biol.* **46**, 3327–3338 (2020).

157. Zhou, Y., Yang, K., Cui, J., Ye, J. Y. & Deng, C. X. Controlled permeation of cell membrane by single bubble acoustic cavitation. *J. Control. Release* **157**, 103–111 (2012).

158. Kooiman, K., Emmer, M., Foppen-Harteveld, M., van Wamel, A. & de Jong, N. Increasing the endothelial layer permeability through ultrasound-activated microbubbles. *IEEE Trans. Biomed. Eng.* **57**, 29–32 (2010).

159. Telichko, A. V *et al.* Therapeutic Ultrasound Parameter Optimization for Drug Delivery Applied to a Murine Model of Hepatocellular Carcinoma. *Ultrasound Med. Biol.* **47**, 309–322 (2021).

160. Chen, X., Wang, J., Pacella, J. J. & Villanueva, F. S. Dynamic Behavior of Microbubbles during Long Ultrasound Tone-Burst Excitation: Mechanistic Insights into Ultrasound-Microbubble Mediated Therapeutics Using High-Speed Imaging and Cavitation Detection. *Ultrasound Med. Biol.* **42**, 528–538 (2016).

161. Pozrikidis, C. & Davis, J. M. Chapter 6 - Blood Flow Through Capillary Networks. in (eds. Becker, S. M. & Kuznetsov, A. V. B. T.-T. in B. M.) 213–252 (Elsevier, 2013). doi:https://doi.org/10.1016/B978-0-12-415824-5.00006-0.

162. Suklabaidya, S. *et al.* Experimental models of pancreatic cancer desmoplasia. *Lab. Investig.* **98**, 27–40 (2018).

163. Riobo-Del Galdo, N. A., Lara Montero, Á. & Wertheimer, E. V. Role of Hedgehog Signaling in Breast Cancer: Pathogenesis and Therapeutics. *Cells* **8**, 375 (2019).